Evaluation of the Effect of Buoyancy on the flow, heat transfer and performance of a Printed Circuit Heat Exchanger
A Numerical Study

Neofytos Dimitriou

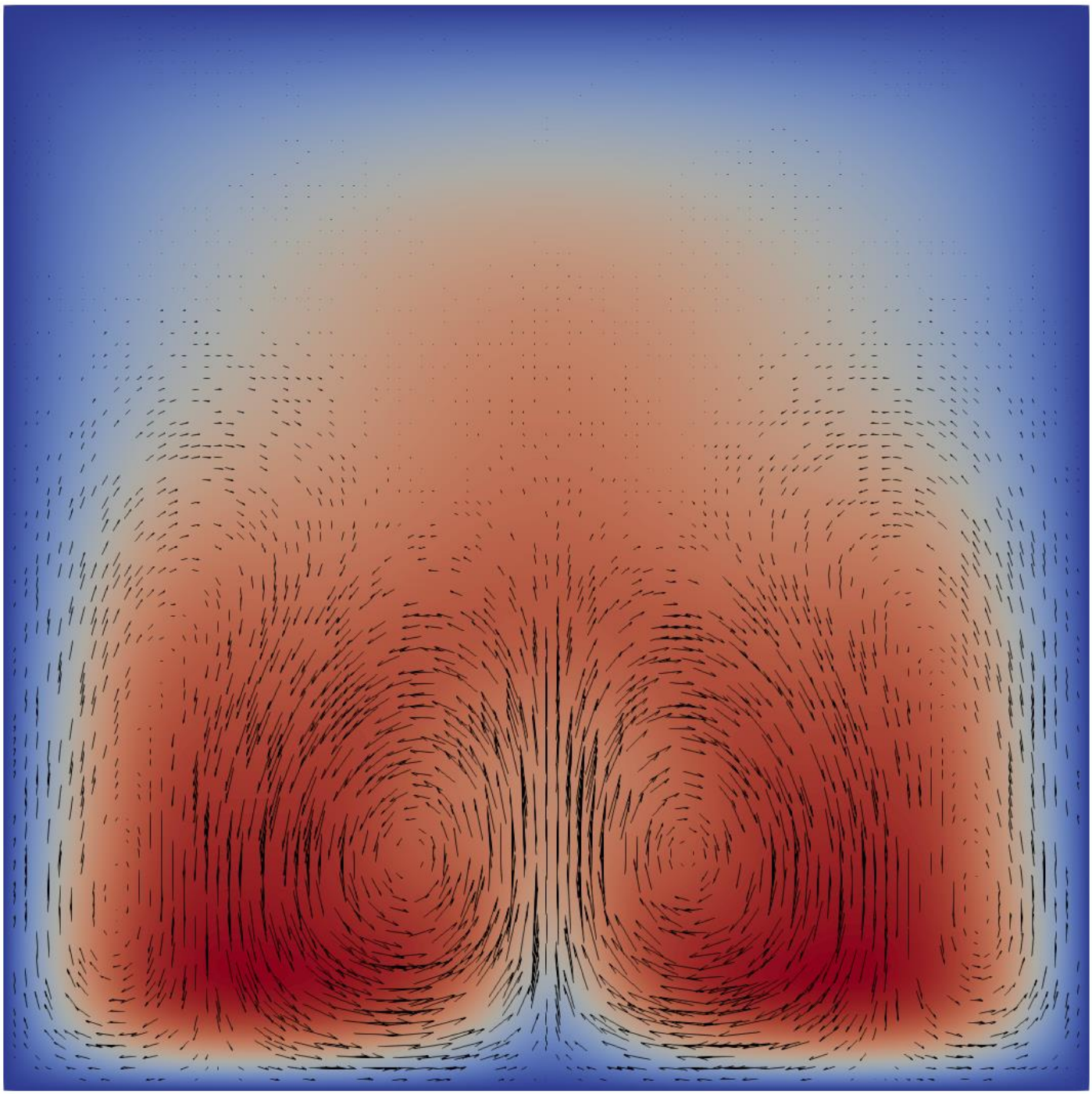

TU Delft

Evaluation on the Effect of Buoyancy on the flow, heat transfer and performance of a Printed Circuit Heat Exchanger
A Numerical Study

By

Neofytos Dimitriou

to obtain the degree of Mater of Science in

Mechanical Engineering

at the Delft University of Technology
to be defended publicly on Thursday December 9, 2021 at 14:00 AM.

Student number: 5120799
Thesis committee: Dr.ir. J.W.R. Peeters, TU Delft, supervisor
Dr.ir. R. Pecnik, TU Delft
Dr. R. Delfos, TU Delft

This thesis is confidential and cannot be made public until December 31, 2021.

An electronic version of this thesis is available at http://repository.tudelft.nl/.

TU Delft

Abstract

One of the biggest threats that humanity is currently facing is the climate change. The amount of greenhouse gases emissions and specifically the amount of CO_2 in the atmosphere has increased and is projected to increase even more in the next years. One possible solution is the use of supercritical CO_2 as an alternative working fluid in power cycles (e.g., Rankine and Brayton cycle). Supercritical fluids operate at pressures and temperature higher than their corresponding critical pressure and temperature value. They behave as a single-phase substances with variable thermophysical properties. CO_2 at supercritical conditions is denser than supercritical water and steam which can affect the efficiency and the design of multiple mechanical components. printed circuit heat exchangers due to their unique design are suitable for supercritical application. They are compact heat exchangers which can operate at high pressures and temperatures and they can achieve high effectiveness. Because of the rapid variation of the thermophysical properties, heat transfer and flow characteristics in supercritical conditions are affected. Three typical heat transfer modes can occur: 1) Normal Heat Transfer, 2) Deteriorated Heat Transfer and 3) Enhanced Heat Transfer. Furthermore, induced forces due to the density difference also known as buoyancy effects are observed in these conditions and can affect both the flow, the heat transfer of the fluid and thus the performance of the heat exchanger.

The main focus of this study is the induced buoyancy effects inside a printed circuit heat exchanger at laminar flow. Initially, a printed circuit heat exchanger is designed based on the literature. Using this heat exchanger geometry two sets of simulations are conducted in OpenFOAM. In the first set of simulations the Reynolds number and the flow thermal capacity are kept constant while the Grashof number is kept nearly constant in order to determine the dependence of Grashof number on the buoyancy effects. In the second set of simulations the Reynolds number, the flow thermal capacity and temperature difference are kept constant to evaluate the performance of the heat exchanger under real working conditions. Three geometries are under investigation (0.015/ 0.03/ 0.06 m) in three different orientations. 1) Vertical Upwards (Assisted Buoyancy), 2) Vertical Downwards (Opposed Buoyancy) and 3) Horizontal.

In the assisted buoyancy cases the induced buoyancy effects produce an M-shape velocity profile due to the acceleration of the flow near the walls and the deceleration of the flow in the centre of the channel. In this orientation the heat transfer coefficient and the Nusselt number increase and enhanced heat transfer is observed. On the other hand, in the opposed buoyancy cases the velocity near the walls decelerates and accelerates in the centre of the channel resulting to the formation of a Bell-shape velocity profile. Both the heat transfer coefficient and the Nusselt number in this orientation decreases and therefore deteriorated heat transfer is observed. It is also shown that in the opposed buoyancy cases the intense buoyancy effects can produce instabilities of the flow and recirculation zones inside the heat exchanger. Instead of the expected deteriorated heat transfer, the produced instabilities result in enhancement of heat transfer. In the horizontal cases, depending on the conditions, heating or cooling, the maximum streamwise velocity is shifted at the bottom surface (Heating conditions) and at the top surface (Cooling conditions). The formation of the secondary flow inside the horizontal heat exchangers produces an average increase of the heat transfer coefficient and the Nusselt number, thus enhancement of heat transfer.

The performance of the printed circuit heat exchanger in the three orientations is also evaluated. It is shown that buoyancy effects can directly affect the effectiveness and the performance of the heat exchanger. In the cases where enhancement of heat transfer is observed (Assisted Buoyancy and Horizontal) the heat exchanger's effectiveness increases. For the Opposed Buoyancy cases decrease of the effectiveness is observed due to the deterioration of heat transfer inside the heat exchanger. Important parameters when investigating buoyancy effects inside the heat exchanger are the diameter of the geometry (Directly proportional to the magnitude of the buoyancy effects) and the Grashof number (Differentiates between all the cases and can be used as an indication of the importance of the buoyancy effects). In all the aforementioned cases the overall heat transfer coefficient is affected which has a direct impact on the design (Length) and the cost of the heat exchanger.

Acknowledgements

First and foremost, I would like to thank my supervisor, Dr. ir. Jurriaan W. R. Peeters for giving me the opportunity to work on such an interesting project. His guidance through this project and the feedback he gave me was absolutely invaluable, allowing me to improve my work and my results. In addition, even in these tough times with the pandemic his supportive attitude kept me motivated and I am really grateful for that. I would, also, like to thank Dr. ir Rene Pecnik and Dr Rene Delfos for taking the time to read and attend my thesis defense.

Finally, I would like to give my highest gratitude to my family for their unconditional love and support throughout my life. I would also like to thank all my friends for making my Master's time unique and full of experiences.

Neofytos Dimitriou
Delft, December 2021

Table of Contents

List of Figures

List of Tables

1 Introduction

One of the biggest threats that humanity is currently facing is the climate change. Human activity is influencing the climate and the earth's temperature. At the same time adds huge amounts of greenhouse gases which increases the greenhouse effect and global warming (Causes of Climate Chnage). The main contributor to global warming is the CO_2 produced when burning coal, oil and gas for producing energy. In recent years the global energy usage and demand has increased massively and according to (U.S. Energy Information Administration (EIA), 2019) the world energy usage is projected to increase nearly 50% by 2050. Consequently, the amount of CO_2 in the atmosphere has increased more than 20% in the last four decades and is projected to rise even more. Figure 1.1 shows the global monthly average concentration of CO_2 in the last 40 years according to (U.S. Global Change Research Programm). Finding new solutions and technologies is an urgent need.

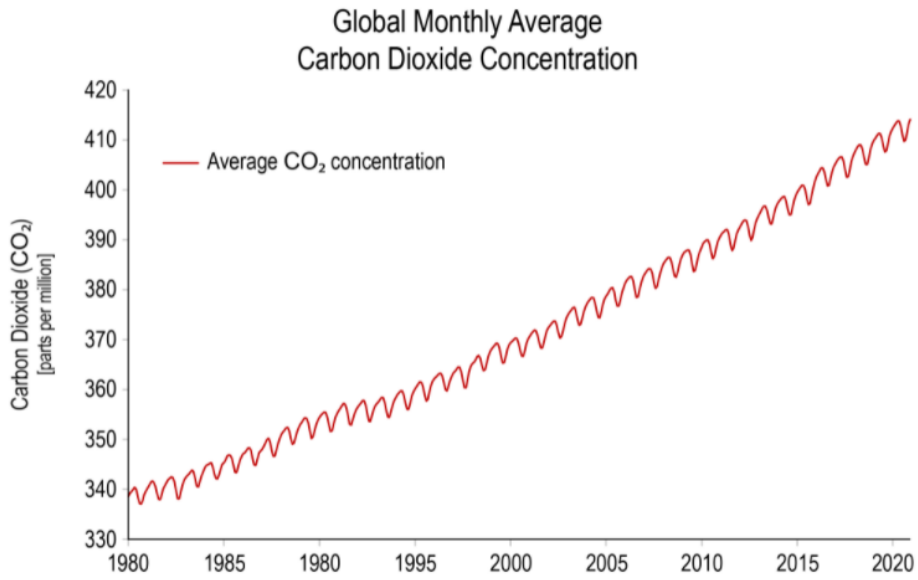

Figure 1.1: Global monthly average concentration of CO_2 in the last 40 years (U.S. Global Change Research Programm).

Supercritical fluids and specifically supercritical CO_2 emerge as an alternative working fluid in power cycles (e.g., Rankine and Brayton cycle). The usage of supercritical CO_2 can affect both the reduction of the average CO_2 concentration on the atmosphere and at the same time increase the efficiency of certain applications. Supercritical fluids operate at pressures and temperatures higher than their corresponding critical pressure and temperature value. One of their most unique behavior is the fact they can act as a single-phase substances with variable thermophysical properties. Immediately a huge amount of energy which is consumed to transform water to steam and vice versa can be saved. Furthermore, CO_2 can easily reach its critical conditions (P_{cr} = 7.38 MPa and T_{cr} = 31.0 °C) where it's very dense compared to other working fluids. As a result, by using supercritical CO_2 bigger amount of power can be extracted out of it in a smaller area (Higher efficiency). This special characteristic has a huge impact on the size reduction of mechanical components such as turbine and pump, leading to smaller power plant footprint and possibly lower manufacturing costs. A comparison between a conventional steam turbine and a supercritical CO_2 turbine is shown in Figure 1.2 (Energy Matters, 2018). Apart from that CO_2 can be found abundant in nature and it has low cost, it is non-toxic and chemically stable. Therefore, the use of supercritical CO_2 has many advantages and can be a breakthrough. One of the most important mechanical components in the aforementioned applications is the heat exchanger. Heat exchangers performance is very crucial because they will ensure that supercritical CO_2 is being correctly heated or cooled between the different stages of the power cycle.

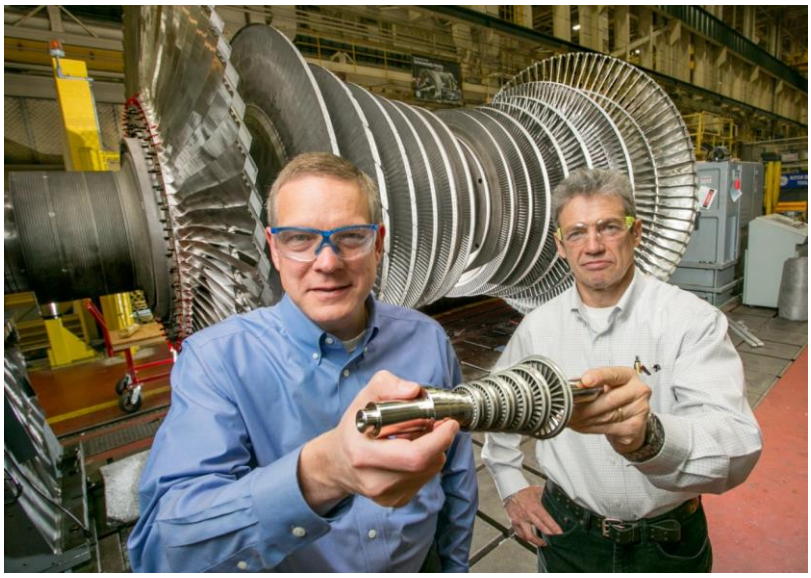

Figure 1.2: Comparison between a conventional steam turbine and a supercritical CO_2 turbine (Energy Matters, 2018).

Because of this rapid variation of the thermophysical properties, heat transfer and flow characteristics in supercritical conditions are different. According to (Pioro I. , 2020) three typical modes of heat transfer can occur: **1)** Normal Heat Transfer, **2)** Deteriorated Heat Transfer (It is characterized by lower values of the wall Heat Transfer Coefficient) and **3)** Enhanced Heat Transfer (It is characterized by higher values of the wall Heat Transfer Coefficient). In addition, other effects such as buoyancy and acceleration are induced by the density variation at supercritical pressures. Specifically, buoyancy effects are forces induced due to the density difference in the radial direction. They are very unpredictable and can affect the flow and the heat transfer inside a heat exchanger leading to enhanced or deteriorated heat transfer depending on the orientation of the heat exchanger.

Heat Exchanger is a device which is used for transferring thermal energy (enthalpy) between two or more process fluids. Heat exchangers have widespread industrial and domestic applications. They have been developed for use in steam power plants, chemical processing plants, building heat and air conditioning systems, transportation power systems and refrigeration units (Schltinder, 1983). Heat exchangers have been classified according to (1) Construction, (2) Transfer process, (3) Degrees of surface compactness, (4) Flow arrangements, (5) Pass arrangements, (6) Phase of the process fluids and (7) Heat transfer mechanisms (Kuppan, 2000).

Printed circuit heat exchangers because of their unique design are suitable for supercritical applications. They are classified as plate heat exchangers with direct heat transfer from the hot fluid to the cold fluid through a separating wall. Printed circuit heat exchangers are compact heat exchangers with large specific heat transfer area. They can operate in all three flow arrangements (Parallel flow, counterflow and crossflow) and both pass arrangement (Single pass or multipass). Furthermore, they are classified as Liquid-Liquid heat exchangers where the basic heat-transfer mechanism employed for heat transfer from one fluid to the other is single-phase convection, forced or free. Due to their small size the fluid pressure drop can be a constraint. However, the main advantages of printed circuit heat exchangers are the high operating pressure and temperatures and high effectiveness (Kuppan, 2000).

1.1 Motivation of the study

The main focus of the present study is the induced buoyancy effects inside a printed circuit heat exchanger at laminar flow. Multiple simulations with different Reynolds and Grashof number will be conducted in OpenFOAM in three different orientations (Vertical Upwards, vertical downwards, Horizontal). The effect of buoyancy on the flow and heat transfer in each orientation will be identified. Insights of this study will clarify the effect of buoyancy on the performance and the effectiveness of heat exchangers, with a final goal of improving the design of printed circuit heat exchangers.

1.2 Research Questions and Objectives

The main questions of this thesis are the following:
How is the effectiveness of a Heat Exchanger affected by:

1. **The varying density and the buoyancy effects**
2. **Heat transfer enhancement and heat transfer deterioration**
3. **The different geometry orientation**

To answer these questions, the following objectives are formulated:
Objective I: Design a Printed Circuit Heat Exchanger model
Objective II: Identify the different flow and heat transfer characteristics in each orientation
Objective III: Evaluate the performance of the Printed Circuit Heat Exchanger in each orientation

1.3 Thesis Outline

Chapter 2 provides the theoretical background retrieved from the literature study explaining all the important terms which are used later in this study.

Chapter 3 provides the simplified governing equations based on the Boussinesq approximation and the Balanced Heat Exchanger's equations and formulas.

Chapter 4 presents the design of the Printed Circuit Heat Exchanger along with the boundary conditions and the solver used in OpenFOAM. The Heat Exchanger geometry and the Boussinesq approximation implementation are also validated.

Chapter 5 discusses the design of the simulations and identifies the two sets of simulations along with the under-investigation orientations.

Chapters 6/ 7/ 8 present the results of the assisted buoyancy, opposed buoyancy and horizontal simulations respectively. In each chapter the flow and heat transfer characteristics are described.

Chapter 9 investigates the performance of the heat exchanger in each orientation and presents relations between the Grashof number and the Heat Exchanger's parameters.

Chapter 10 summarises the most important outcomes of this study with recommendations for further investigation and improvement.

2 Literature Review

In this chapter the theoretical background retrieved from scientific articles is provided explaining the most important terms which are used in this work. Section 2.1 analyses the main aspects of supercritical fluids. Section 2.2 analyses the major advantages of supercritical fluids and their most important applications. In Section 2.3 the behavior of supercritical fluids is being described. Section 2.4, 2.5 and 2.6 distinguish the different heat transfer regimes at supercritical conditions and examines the heat transfer of sCO_2 at both laminar and turbulence flow. Finally, in Section 2.7 the printed circuit heat exchangers are introduced with performance results from the literature.

2.1 Aspects of Supercritical fluids

A supercritical fluid is a fluid with a pressure and temperature higher than its corresponding critical pressure and temperature value. At supercritical conditions, there are never two distinguishable liquid and vapor phases in equilibrium. The critical pressure for a pure substance is defined as the pressure above which liquid and gas cannot coexist at any temperature. The critical temperature for a pure substance is the temperature above which the gas cannot become liquid, regardless of the applied pressure. The intersection between critical pressure and critical temperature gives us the critical point in which distinction between the liquid and gas phase disappears. Both phases have the same temperature, pressure and density. The critical point is characterized by the phase-state parameters T_{cr}, p_{cr}, ρ_{cr} which have unique values for each pure substance. The critical pressure and temperature for CO_2 is 7.38 MPa and 31.0 °C respectively and can be seen in the Pressure Vs Temperature diagram of Figure 2.1 (Gupta, et al., 2013).

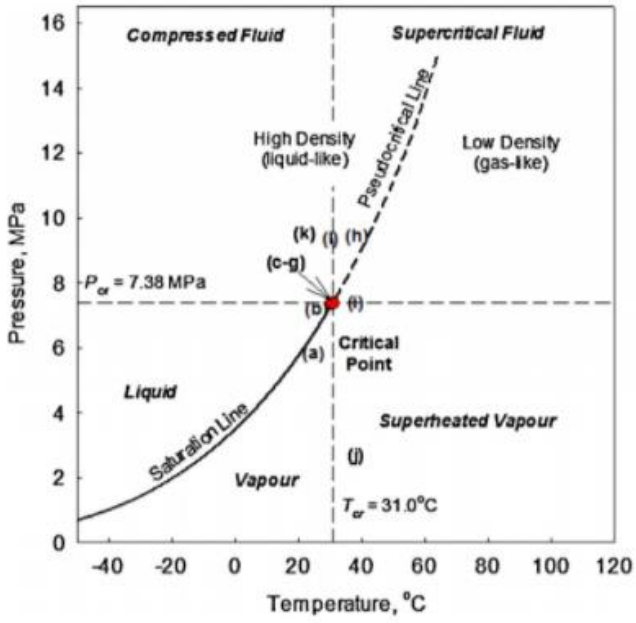

Figure 2.1: *P* Vs *T* Diagram for CO_2 (Gupta, et al., 2013).

Other important terms defined in Figure 2.1 are compressed fluid and superheated vapor. Compressed fluid is a fluid at a pressure above the critical pressure, but at a temperature below the critical temperature. Superheated vapor is a vapor at pressures below the critical pressure, but at temperatures above the critical temperature.

Photographs of the transition between different phases are shown in Figure 2.2 with alphabetical order and the position of this transition is exactly presented in Figure 2.1 (Gupta, et al., 2013).

Transition of CO_2: (a) Sub-critical CO_2, (b) – (g): Transition through the critical point, (h): Supercritical CO_2, (i): Between supercritical fluid and superheated vapor, (j): Superheated vapor, (k): Compressed fluid and (l): Between compressed fluid and supercritical fluid.

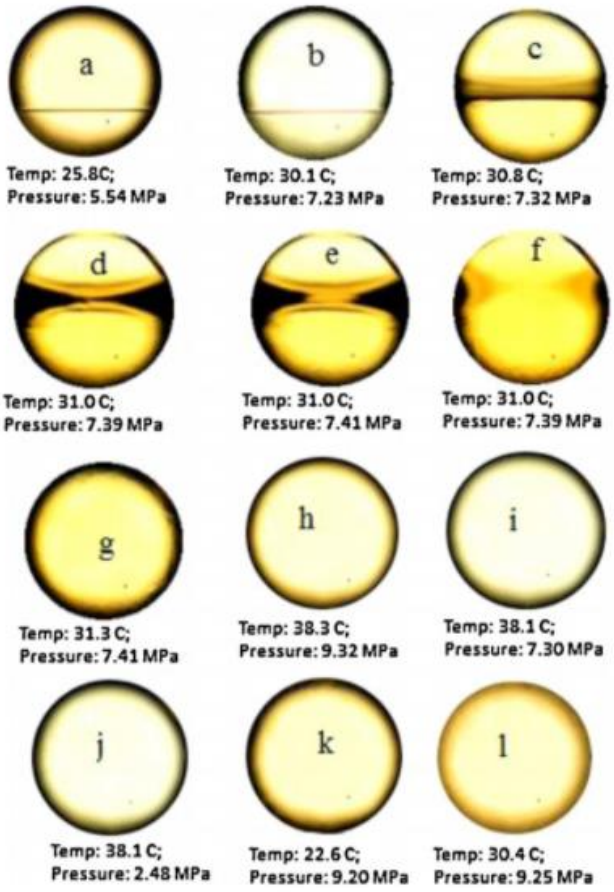

Figure 2.2: Transition of CO_2 through different phases (Gupta, et al., 2013).

2.2 Supercritical fluids applications

The performance of many engineering systems which use thermodynamic cycles is based on the pressure of the different components. In general, by increasing the pressure of the working fluid higher efficiencies can be achieved. Engineering systems that use supercritical pressure fluids take advantage of the single-phase behavior of the fluid which leads to better performance and more compact design (Pizzarelli, 2018). CO_2 is extensively used as the working fluid in many applications due to the fact that it is environmentally friendly natural material which can be found abundant in nature and it has low cost, it is non-toxic and chemically stable. Furthermore, it has no ozone depletion (ODP = 0) and low global warmth potential (GWP = 1). Also, CO_2 with relatively low costs can easily reach its critical conditions (P_{cr} = 7.38 MPa and T_{cr} = 31.0 °C) (Zhang, Xu, Liu, & Dang, 2020). As a result, supercritical fluids and especially supercritical CO_2 are used in many industrial applications, processes and systems. Some of the most relevant engineering applications are mentioned below:

- **Transcritical Supercritical Rankine Cycle:** The supercritical Rankine cycle has the same working principle as the normal Rankine cycle, but the fluid is pressurized beyond its critical point. It has efficient temperature matching between the heat source and the working fluid and it is more compact and environmentally friendly than the steam and organic Rankine cycle (Sarkar, 2015). An example of this cycle is the Water-Cooled Nuclear Reactor which operates at supercritical pressures and temperatures. This concept will simplify the nuclear system setup because steam generators, steam separators and steam dryers are not required. At the same time steam turbines and re-heaters size can be smaller but the steam cycle efficiency can be higher. One of the disadvantages of this technology is the occurrence of heat transfer deterioration with catastrophic results (Schulenberg, et al., 2011). Another example is the CO_2 fluid in collectors of solar Rankine cycle system which combines both solar power and a heat thermodynamic cycle with high efficiency. This innovation is very promising and can become competitive with fossil-fuel- based systems because it can reduce the cost, size and at the same time improve the thermodynamic performance. The solar energy

powered Rankine cycle system with supercritical CO_2 can generate electrical power and heat or refrigeration with very high system efficiency (Niu, Yamaguchi, Zhang, Iwamoto, & Hashitani, 2011). Figure 3 shows the Pressure Vs Volume and Temperature Vs Entropy diagram of a transcritical supercritical Rankine cycle (1 → 2 compression, 2 → 3 heating, 3 → 4 expansion and 4 → 1 cooling) (Sarkar, 2015).

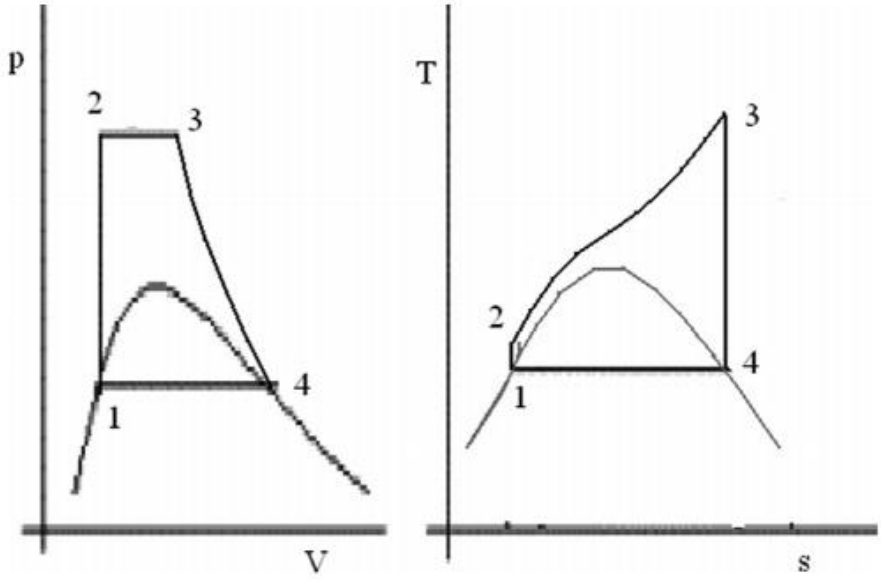

Figure 2.3: *P* Vs *V* and *T* Vs *S* diagram of a transcritical supercritical Rankine cycle.

- **Supercritical Carbon-Dioxide Brayton Cycle:** A power conversion system which combines the advantages of both steam Rankine cycle and gas turbine cycle. Supercritical CO_2 is compressed in the incompressible region (pseudo-liquid phase) and the turbine operates with a gaseous single-phase fluid (Ahn, et al., 2015). Some benefits of the supercritical CO_2 Brayton cycle when compared to the sub-critical Brayton cycle are high thermal efficiency (increase ~5%) with relatively low turbine inlet temperatures, compact design and simple system layout (Yoon, Ahn, Lee, & Addad, 2012). Figure 2.4 shows the Temperature Vs Entropy diagram of a Supercritical Brayton cycle (Li, Zhu, Guo , Wang, & Tao, 2017).

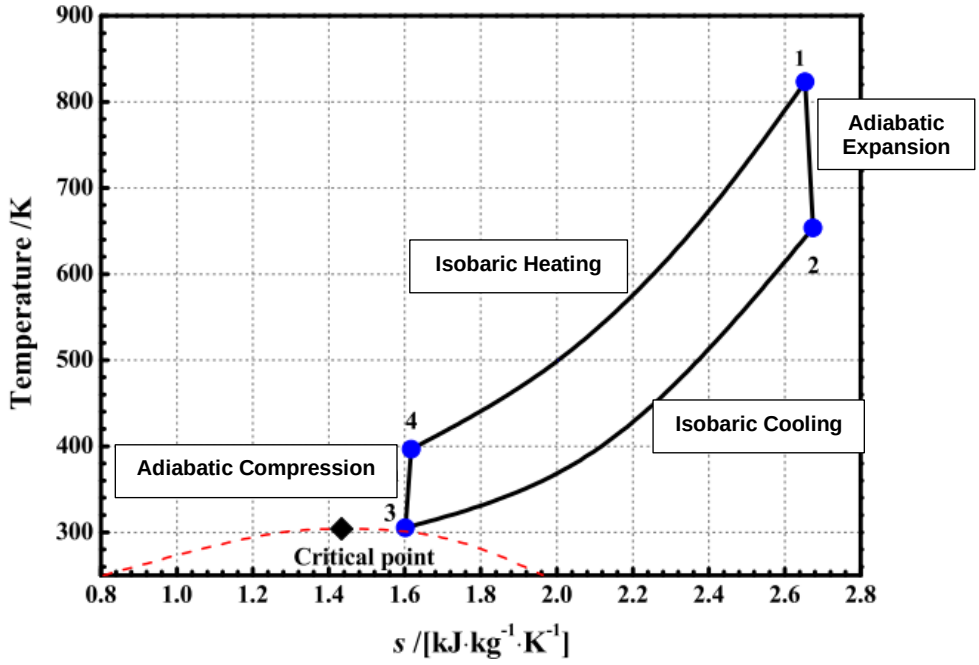

Figure 2.4: *T* Vs *S* diagram of a supercritical Brayton cycle (Li, Zhu, Guo , Wang, & Tao, 2017).

- **Transcritical Carbon-Dioxide Heat Pump Cycle:** The transcritical CO_2 Heat Pump cycle can be used to achieve high temperature lift due to the high volumetric heating capacity of these heat pumps, making them suitable for hot water applications. The high heat-output temperatures are possible even with a single-stage cycle, reducing the system size and cost. Furthermore, with simple configurations high efficiencies and high power densities can be achieved (Lecompte, et al., 2019).
- **Oxygen-Methane Rocket engine:** One of the first applications of supercritical fluids. The pressure in the combustion chamber is higher than the critical pressure of most of the propellants. Methane can be stored in liquid phase and the tank design can be more compact. In the current application methane is used for cooling the combustion chamber through cooling channels around the combustion chamber. One disadvantage of this application is the possible occurrence of heat transfer deterioration (Pizzarelli, 2018).
- **Supercritical Water Oxidation:** A homogeneous reaction between the oxidizable materials and oxygen is observed due to the high sensitivity of solubility at supercritical conditions (Sabirzyanov, Il'in, Akhunov, & Gumerov, 2000). A versatile technology able to destruct industrial wastes and sludges materials in small residence times (Bermejo & Cocero, 2006). Destruction efficiencies of 99.9% or higher have been reported for a variety of toxic and nontoxic materials.
- **Supercritical fluids as Solvents:** Supercritical fluids are attractive energy saving alternative to distillation and liquid extraction. Supercritical fluids high density high compressibility and high dissolving power can be used in various environmental separations, reaction processes and material processing. Major advantages of this kind of technologies are environmentally benign solvents can be used (e.g. CO_2 which is cheap non-toxic and non-flammable) and the reaction conditions are milder when solvents such as CO_2 with low critical pressure and temperature are used (Eckert, Knutson, & Debenedetti, 1996).

2.3 Thermophysical properties of SC fluids/ sCO_2

Supercritical fluids behave as a single-phase substance with variable thermophysical properties. The behavior of supercritical fluids crossing the pseudocritical line can be compared with crossing the saturation line from liquid to vapor. The biggest difference between crossing these two lines is that all variations in thermophysical properties at supercritical conditions are gradual and continuous. On the other hand, while crossing the saturation line at sub-critical pressures we observe a discontinuity in thermophysical properties with one value for liquid phase and another for vapor phase at the same temperature (Pioro & Mokry, 2011). Supercritical fluids despite ‘’acting’’ as a single-phase substance have three different states. The three possible states of supercritical fluids are Pseudoliquid state, Pseudophase transition (pseudo-boiling) and Pseudogas state.

Pseudoliquid state: The region where the supercritical fluid can be considered as a liquid with high values of density.
Pseudophase transition (pseudo-boiling): The region where the maximum specific heat capacity occurs and where the dependences of thermophysical properties on both pressure and temperature are peculiar. In this region supercritical fluids transform from a supercritical liquid-like fluid to a supercritical gas-like fluid when they cross the Widom line (Banuti, 2015).
Pseudogas state: The region where the supercritical fluid can be considered as a gas with low values of density (Kurganov, Zeigarnik, & Maslakova, Heat transfer and hydraulic resistance of supercritical pressure coolants. Part I: Specifics of thermophysical properties of supercritical pressure fluids and turbulent heat transfer under heating conditions in round tubes (state of the art), 2012).

As mentioned before, we observe a significant variation of thermophysical properties near the critical point. Properties such as density and dynamic viscosity decrease within a very narrow temperature range (transition from pseudoliquid state to pseudogas state). At the same temperature range thermal expansion coefficient, specific heat capacity, thermal conductivity and Prandtl number have peaks near the critical and pseudocritical points. The peak of specific heat capacity occurs at the pseudocritical temperature, while the peaks of thermal expansion coefficient and thermal conductivity may not correspond to the pseudocritical temperature. Pseudocritical point is a point at a pressure above the critical pressure and temperature. This particular point corresponds to the maximum value of the specific heat for this particular pressure. The pseudocritical point is characterized with unique P_{pc} and T_{pc} values for all the pressures above the T_{cr} (Gupta,

Farah, King, Mokry, & Pioro, 2010). The line which consists of pseudocritical points is the pseudocritical line (Pioro & Mokry, 2011). Also, it is observed that the kinematic viscosity and thermal diffusivity undergo through the minimum in this temperature range. The behavior of these properties is a function of pressure and by increasing the pressure the magnitudes of these peaks and minimums decrease very quickly (Pioro & Mokry, 2011).

Figure 2.5 shows the variation of thermophysical properties of CO_2 at 8 MPa as a function of temperature. The pseudocritical temperature of CO_2 at 8 MPa is 34.75 °C is also indicated in the figures. The values of the properties have been calculated using an Excel file of Coolprop (CoolProp).

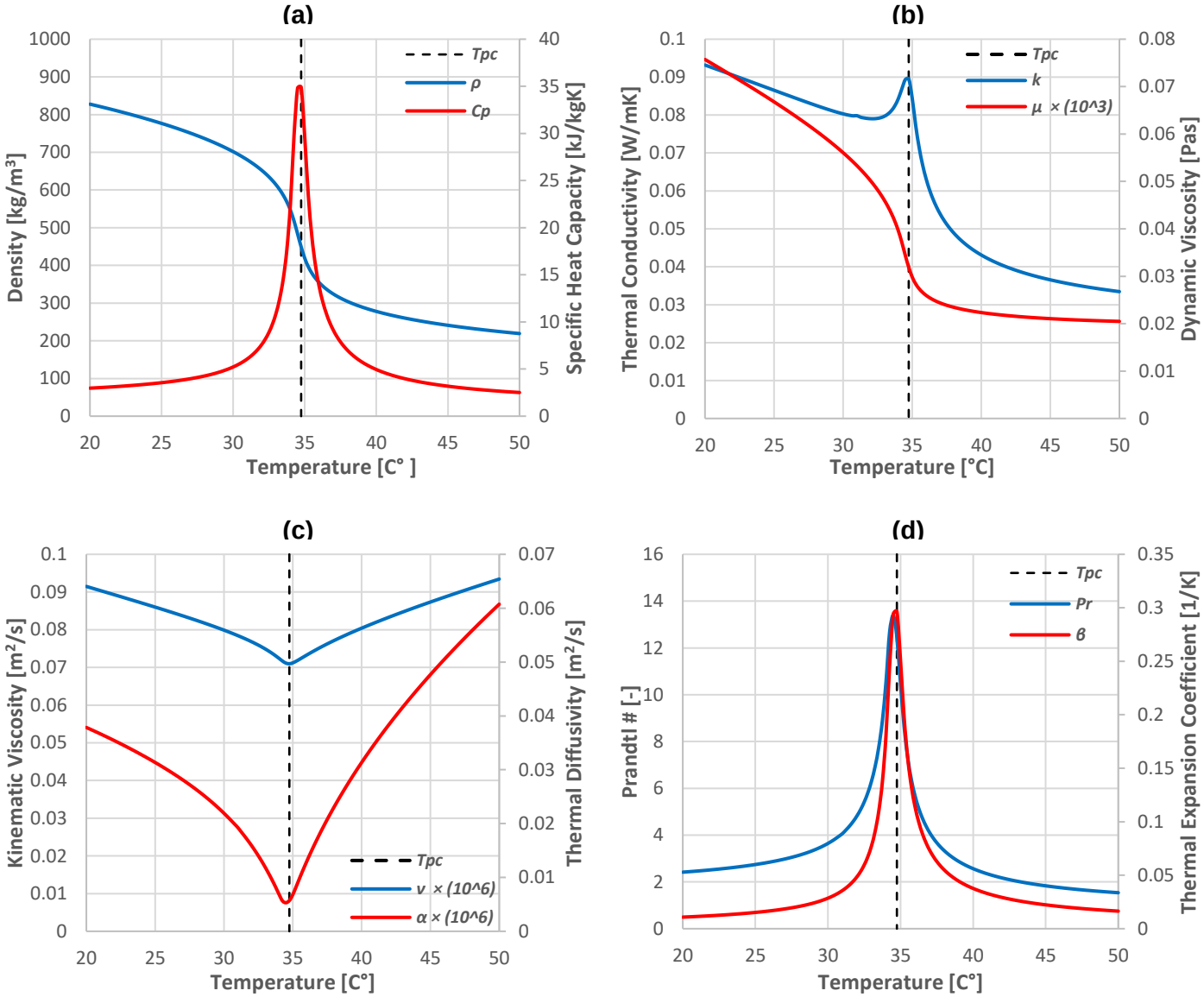

Figure 2.5: Thermophysical properties of CO_2 at 8 MPa as a function of Temperature. **(a)** Density and specific heat capacity, **(b)** Thermal conductivity and dynamic viscosity, **(c)** Kinematic viscosity and thermal diffusivity and **(d)** Prandtl number and thermal expansion coefficient (CoolProp).

2.4 Heat Transfer regimes of sCO_2

Due to the large variation of the thermophysical properties at supercritical pressures, heat transfer at these conditions is significantly affected. Under supercritical pressure depending on the heat load and the thermodynamic state three typical modes of heat transfer can occur: Three typical modes of heat transfer can occur: Normal heat transfer, Deteriorated heat transfer and Enhanced heat transfer (Yoo, 2013).
In order to evaluate and distinguish the three different types of heat transfer, three identification methods are used:

I. The wall temperature curve. It estimates how a single operation parameter such as the diameter of the tube, pressure of the fluid, heat flux, fluid velocity etc affect the wall temperature.
II. The correction term of supercritical fluids to constant fluid heat transfer (h / h_{DB}). This correction term shows the difference between the actual and ideal heat transfer which is due to thermophysical properties variations, buoyancy effects and thermal acceleration effects.
III. The heat transfer coefficient. It is used for identifying the type of heat transfer at heat exchangers with supercritical fluids as working fluids.

(Zhang, Xu, Liu, & Dang, 2020)

Using the identification methods mentioned above the definition of each heat transfer mode can be deduced:

- Normal Heat Transfer: It is characterized by normal heat transfer coefficient and wall temperatures values similar to these of convective heat transfer at sub-critical conditions. As a result, heat transfer is close to the one calculated with the Dittus-Boelter equation ($0.3 < h / h_{DB} < 1$).
- Heat Transfer Deterioration: It is characterized by higher values of wall temperature in some parts of the examined section and lower values of the heat transfer coefficient. The heat transfer is deteriorated compared to the normal heat transfer regime ($h / h_{DB} < 0.3$).
- Heat Transfer Enhancement: It is characterized by lower values of wall temperature in some parts of the examined section and higher values of the heat transfer coefficient. The heat transfer is enhanced compared to the normal heat transfer regime ($h / h_{DB} > 1$).

(Pioro I. , 2020)

Apart from the variable thermophysical properties, other effects such as the buoyancy force and flow acceleration affect the convection heat transfer and the effectiveness of heat transfer of fluids at supercritical conditions (Jiang, Liu, Zhao, & Luo, 2013).

-Buoyancy effects: Forces induced due to the density difference in the radial direction, between the high-density core and the low-density near the wall flow (Pitla, Robinson, Groll, & Ramadhyani, 1998). Buoyancy effects affect differently heat transfer depending on the direction of the flow. They can cause both enhanced or deteriorated heat transfer in upward flows and enhanced heat transfer in downward flows which depends on whether the flow is heated or cooled (Yoo, 2013). Furthermore, buoyancy affects turbulence through two mechanisms: 1) The indirect/external effect where buoyancy modifies the shear stress and the mean flow profile and 2) The direct/structural effect where turbulence is directly produced by buoyancy. The indirect one is more important while the direct one is negligible (Wang, et al., 2018) (Zhang, Xu, Liu, & Dang, 2020).

-Acceleration effects: Forces induced due to the fluid expansion which caused to density variations in the axial direction (Pitla, Robinson, Groll, & Ramadhyani, 1998). Acceleration forces can cause deteriorated heat transfer in both upward and downward flow (Yoo, 2013).

2.5 Heat Transfer of sCO_2 at Laminar flow

Buoyancy and acceleration effects, have different effects on heat transfer depending on the flow orientation. In this section heat transfer of supercritical CO_2 at various orientations and flow directions will be discussed.

Horizontal Flow:

Cao, Rao , & Liao , 2011 investigated laminar mixed convective heat transfer in horizontal tubes by comparing cases with and without gravity. They found out that gravity forces and buoyancy effects are very important parameters in determining the type of heat transfer in horizontal tubes at supercritical condition.

A significant difference is observed in the cross-section isotherms of the two cases. In the case without gravity isotherms are concentric circles and the maximum temperature occurs at the center of the tube. This pattern remains constant in the entire length of the tube while the maximum temperature at the center of the tube is slowly decreasing. On the other hand, the isotherms for the gravity case are distorted. In the entrance region the maximum temperature occurs at the location above the center point of the tube with the temperature gradient in the upper half being larger than those in the lower half. The distorted shapes of the isotherms are changing as the fluid moves downstream and concentric circles are observed with the maximum at a location above the center point. Furthermore, heat transfer is enhanced in the gravity case because the temperature contours have lower values than the non-gravity case at the same location. In Figure

2.6 the evolution of velocity and nondimensional temperature ($\Theta = \frac{T - T_w}{T_{in} - T_w}$ where T_{in}=120°C and T_w=25°C) are indicated (Cao, Rao , & Liao , 2011).

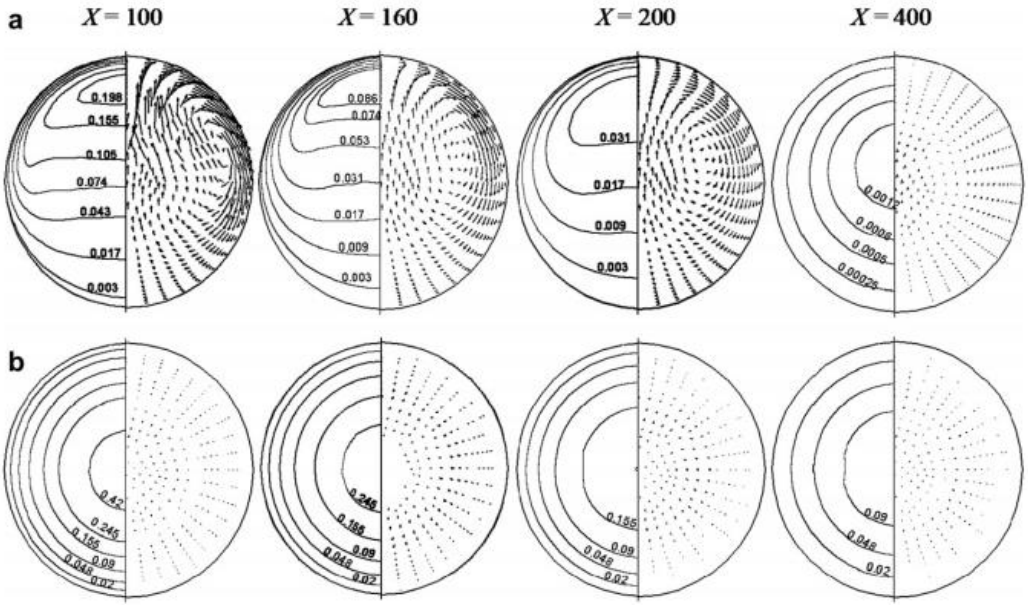

Figure 2.6: Velocity profile and temperature contours for (a) Gravity and (b) Without gravity case (Cao, Rao , & Liao , 2011).

The main difference between these two cases is the secondary flow induced in the gravity case which enhances heat transfer near the walls. This flow is produced from the large temperature difference between the fluid and the wall in the entrance region leading to sharp variation of the fluid density and consequently to induced buoyancy forces. The intensity of the secondary flow is enlarged when the bulk temperature of CO_2 reaches the pseudocritical temperature at which small temperature change of the fluid results to a bigger density variation (Yang, Xu, Wang, & Zhang, 2013). The direction of this secondary flow depends on the experiment's conditions. For cooling conditions, the fluid flow goes downwards along the wall and then moves upward as the flow approaches the vertical axis of the cross section. For heating conditions, the fluid goes upwards along the wall and then moves downwards as the flow approaches the vertical axis. Figure 2.7 shows the direction of the secondary flow for heating and cooling conditions.

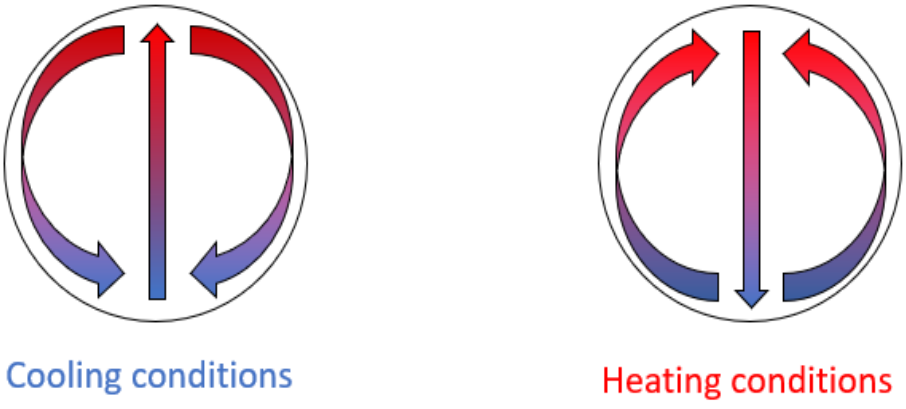

Figure 2.7: Direction of the secondary flow for cooling and heating conditions.

Due to the induced secondary flow and the variable thermophysical properties the maximum axial velocities occur near the top of the tube. Another parameter which is directly proportional to the axial velocity gradient is the wall shear stress. As a result, it varies along the circumference in the entrance region and the maximum occurs in the upper half of the tube. Similarly, parameters such as the Nusselt number and the heat transfer coefficient at the top surface are larger than those at the bottom surface. As a conclusion, the heat transfer is enhanced in the upper half of the tube and slightly deteriorated in the lower half. Figure 2.8 shows

the heat transfer coefficients vs bulk temperature at various inclination angles (α=90°, 0° and -90° referring to vertical upward flow, horizontal flow and downward flow) at the top and bottom surface. All these effects vanish as the fluid flows far downstream. The fluid temperature approaches the wall temperature and buoyancy forces and secondary flow become negligible (Yang, Xu, Wang, & Zhang, 2013).

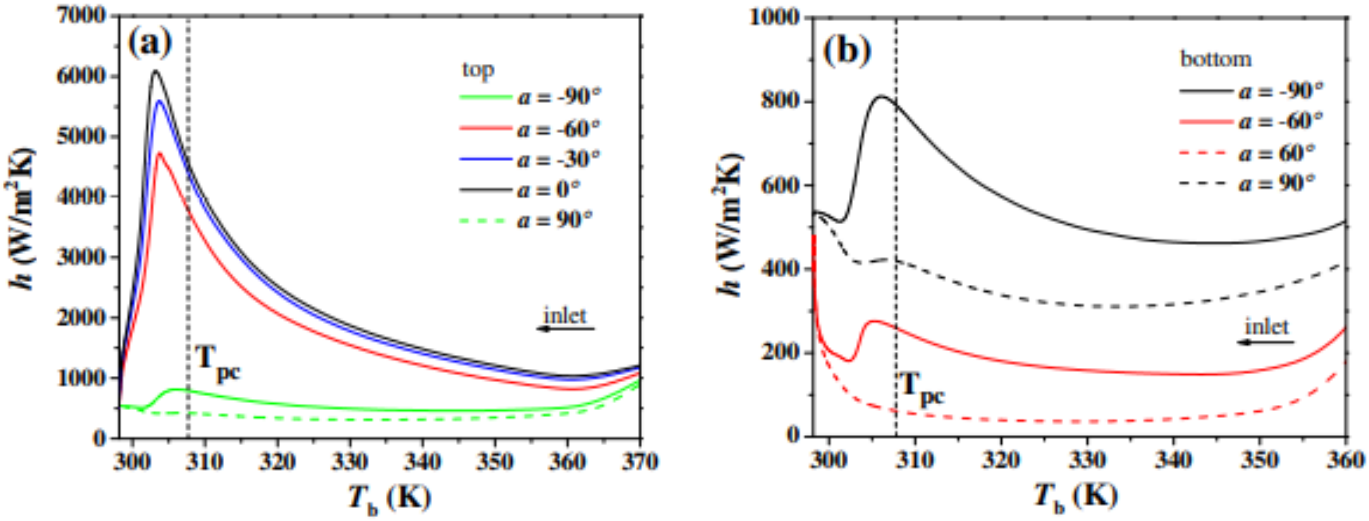

Figure 2.8: Heat transfer coefficient at the top and bottom surface for different inclination angles (Yang, Xu, Wang, & Zhang, 2013).

Similar experiments have been conducted by (Yang, Xu, Wang, & Zhang, 2013) in circular tubes at various inclination angles. Their results will be discussed in the next part of this section.

Vertical Upward Flow:

In cooled vertical upward flow the isotherms in the cross section of the tube are concentric circles and no induced secondary flow is observed. Heat transfer coefficient values are very low and heat transfer in vertical upward flows is mostly deteriorated (Figure 2.6). Despite that, a different phenomenon is observed in this kind of flow and it can be investigated by evaluating the dimensionless friction coefficient $C_f{*}Re_D$ (Where C_f is the local fanning friction factor which is the ratio between the local shear stress and the local flow kinetic energy density) (Khalesi & Sarunac, 2019).

$$C_f = \frac{\tau_w}{\frac{1}{A_c}\int \frac{1}{2}\rho u^2 dA}$$

The fluid in the bulk region is lighter and thus the buoyancy force is upward accelerating the fluid velocity in the bulk region but at the same time decelerating the fluid velocities near the wall. Under specific condition velocities near the wall can become negative yielding to the smallest dimensionless friction coefficient. Figure 2.9 indicates the $C_f{*}Re_D$ at various inclination angles.

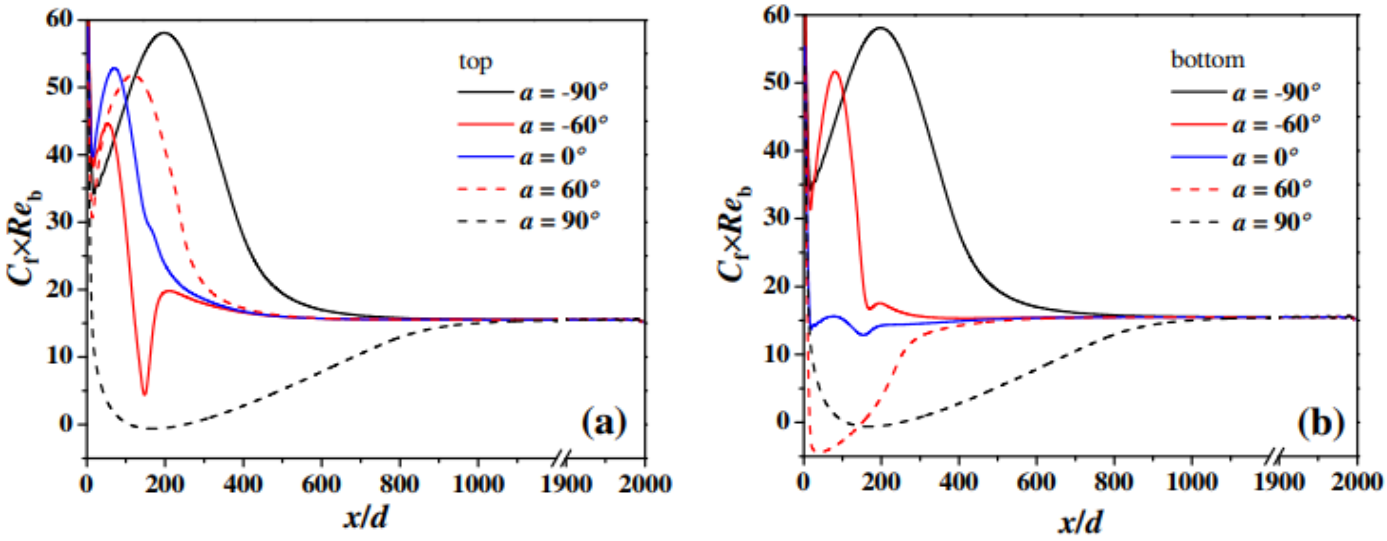

Figure 2.9: Dimensionless friction coefficient at the top and bottom surface for different inclination angles (Yang, Xu, Wang, & Zhang, 2013).

Vertical Downward Flow:

The case of the vertical downward flow is somewhere between the horizontal flow and the vertical upward flow. The isotherms in the cross section of the tube are distorted but not as much as the horizontal tubes and the temperature contours approach the concentric circles. The secondary flow is induced but it is very weak resulting to low values of heat transfer coefficient and deteriorated heart transfer. Nevertheless, the heat transfer performance of this kind of flow is better than the vertical upward flow (Figure 2.8). Furthermore, due to the lighter fluid at the bulk region the buoyancy force is upward decreasing the fluid velocity in the bulk region and at the same time increasing the fluid velocities near the wall. As a result, an M-shape velocity profile is observed and maximum dimensionless friction coefficient values (Figure 2.9).

One of the most important parameters in laminar flows of supercritical fluids is the Grashof number which quantifies the buoyancy force effect on the flow and the heat transfer. Using the Richardson number (Is defined as $\frac{Gr}{Re^2}$)we can evaluate whether the mixed convective flow is important or not in the range of C_{min} (Below that the flow approaches the forced convection flow) and C_{min} (Above that the flow approaches the pure free convective flow). The working fluid affects these limits and for CO_2 is $10^{-3}<Gr/Re^2<10^{-2}$.

2.6 Heat Transfer of sCO_2 at Turbulence flow

In this section heat transfer of supercritical CO_2 at turbulence flow and the various turbulence models used in simulations will be discussed.

Horizontal Flow:

Yu, et al., 2013, Wang, et al., 2018, Xiang, Guo, Huai, & Cui, 2017 and Wang, et al., 2018 in investigated the influence of buoyancy, mass flux, flow direction and tube diameter on heat transfer in horizontal tubes at turbulence flow, under supercritical pressure. Their results will be further analyzed.

In heated horizontal tubes the low-density hot fluid gathers in the upper part of the tube while the high-density cold fluid moves to the bottom regions. Due to the density variation between top and bottom part of the tube a vertical secondary flow is induced. Because of the secondary flow the hot fluid moves to the top surface of the tube where a stagnation region is formed. At the same time the fluid at the bottom surface circulated continuously and momentum is transferred to the fluid in the lower half. As a result, an asymmetric velocity profile is observed with maximum velocity at the bottom region. In cooling conditions, the hot fluid is again gathered in the upper part while the cold fluid moves to the bottom part forming a stagnation region. Now the velocity peaks are observed at the top part of the tube. The intense secondary flow produces a non-uniform wall distribution around the circumference with higher wall temperatures in the top surface. As the temperature at the top wall increases, the fluid in contact with the top surface will be the first to reach the pseudo-critical point. At that moment, a huge variation in thermophysical properties (density, thermal conductivity, heat capacity) is observed. Fluid in that region loses the capability of removing heat, the heat transfer coefficient is decreased and as expected heat transfer is deteriorated. On the other hand, the velocity

gradient of the fluid in the bottom surface keeps growing. Shear stress is directly proportional to the velocity and therefore the turbulence kinetic energy at the bottom surface has higher values. Higher turbulence level means higher mixing and higher thermal diffusivity leading to huge spikes in the local heat transfer coefficient, lower wall temperatures and enhanced heat transfer. Figure 2.10 shows the variation of the wall temperature and the heat transfer coefficient at horizontal tubes.

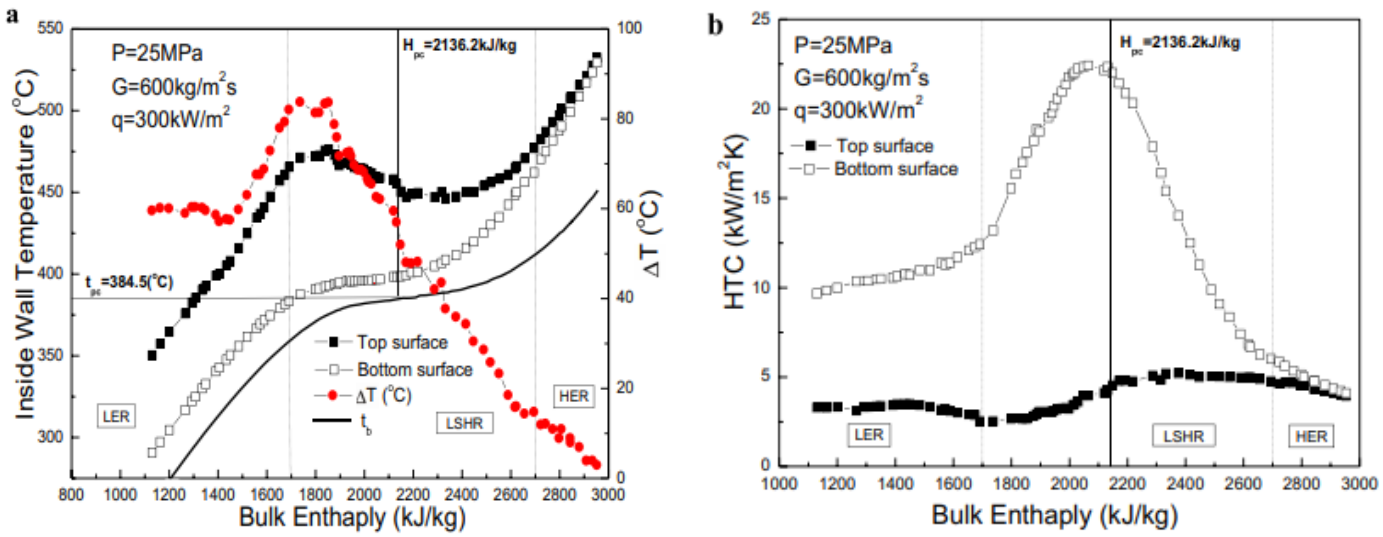

Figure 2.10: Variation of (a) The wall temperature and (b) The heat transfer coefficient at top and bottom surface (Yu, et al., 2013).

Effects such as the mass flux, the heat flux and the tube diameter affect differently heat transfer in horizontal tubes. By increasing the mass flux, the temperature difference between top and bottom surface decreases making buoyancy effects less dominant. Despite the absence of buoyancy effects wall temperatures have lower values and higher heat transfer coefficients leading to enhanced heat transfer in both top and bottom surface. Figure 2.11 shows the effects of mass flux at the wall temperature and the heat transfer coefficient.

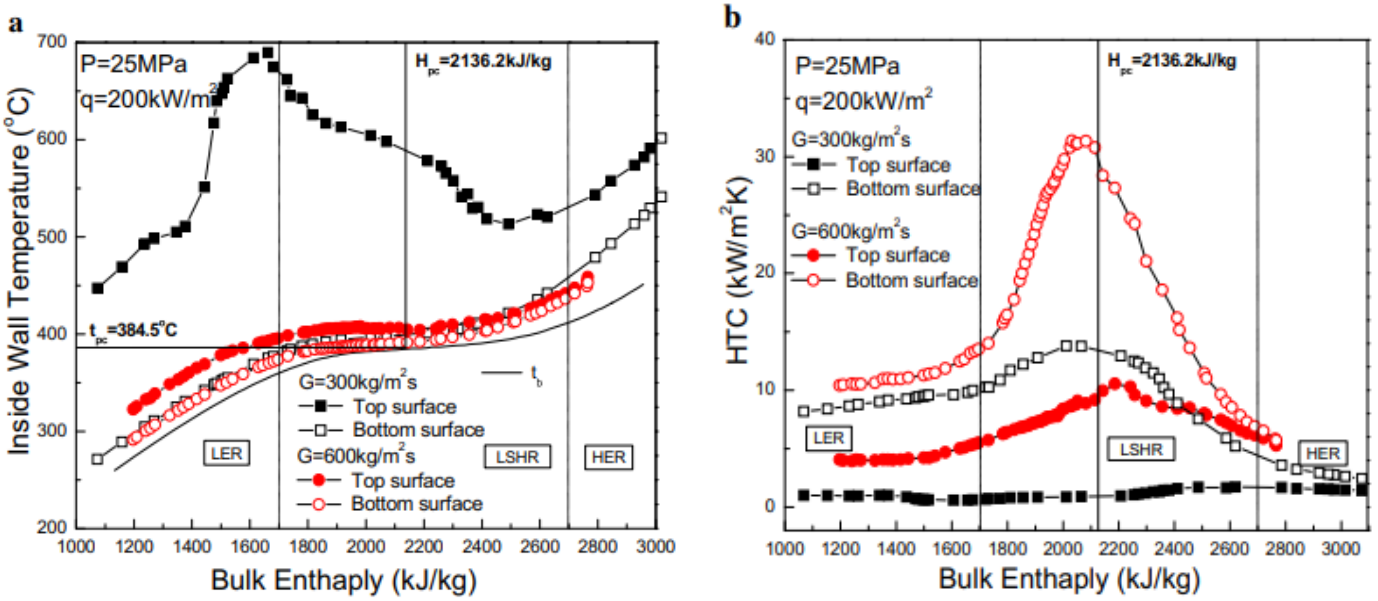

Figure 2.11: Variation of (a) The wall temperature and (b) The heat transfer coefficient at top and bottom surface for different mass flux (Yu, et al., 2013).

Heat flux is proportional to the Richardson number which is used for evaluating the buoyancy influence. As the heat flux increases, Richardson number increases and the buoyancy effects discussed before are more significant and obvious (Higher intensity of the secondary flow, larger velocity gradients in the bottom

of the tube and bigger temperature variation between top and bottom surface). Lastly, by increasing the tube diameter at bulk temperatures above T_{pc} the heat performance of the tube is higher. At temperatures lower than the T_{pc} the temperature diameter does not affect the heat performance of the tube. Figure 2.12 indicated the heat flux effect on the induced secondary flow.

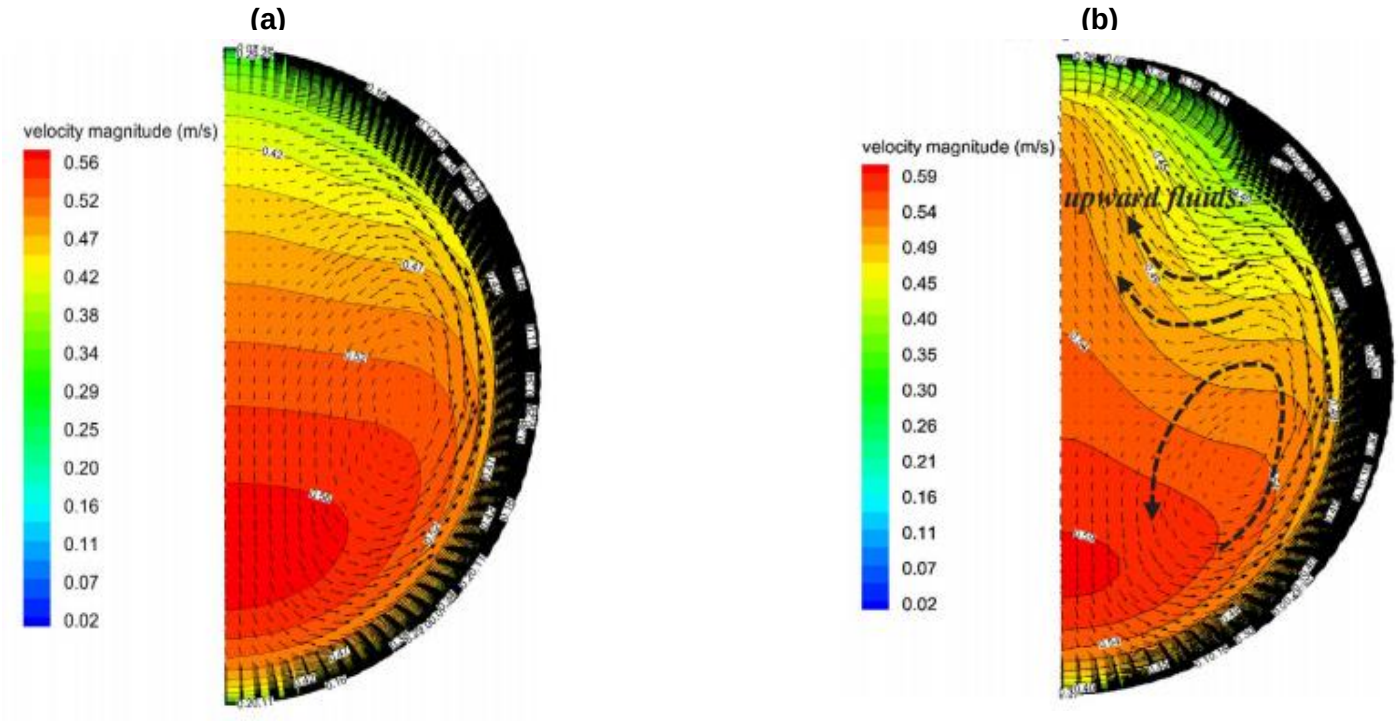

Figure 2.12: Induced secondary flow for (a) q=15.1 kW/m^2 and (b) q=21.5 kW/m^2 (Wang, et al., 2018).

Vertical Upward Flow:

In vertical upward and downward flow buoyancy and thermal acceleration behave differently. He, Kim, & Jackson, 2008, Cheng, Zhao, & Rowinski, 2017, Kurganov, Zeigarnik, & Maslakova, 2013, Kim & Kim, 2011 and Jackson, 2013 investigated these effects. Their results will be discussed in the next parts.

Depending on the buoyancy effects and thermal acceleration turbulence can be divided in three categories: Partially laminarized, Fully laminarized, Recovery flows. (Zhang, Xu, Liu, & Dang, 2020)

- **Partially laminarized:** At first the strong variation of density near the wall causes an increase of the velocity near the wall. Therefore, a transition of the velocity profile is observed. From the normal ‘’U-shape’’ transforms to a ‘’flattened-shape’’. Because of this flat-shape velocity profile, shear stress and turbulent kinetic energy decreases. As a result, the turbulent diffusion of heat is impaired causing an increase of the wall temperature and deteriorated heat transfer.
- **Fully laminarized:** Further increase of the buoyancy effects results to another increase of the velocity near the wall. The velocity profile is significantly distorted and changes from a ‘’flattened-shape’’ to an ‘’M-shape’’ (Wall velocity increases while bulk velocity remains the same). At this moment, laminarization of the flow occurs and turbulence almost disappears consequently the wall temperature is maximum and heat transfer is strongly deteriorated.
- **Recovery regime:** The process continues until turbulence production builds up again and the flow becomes unstable. The velocity profile keeps the ‘’M-shape’’ but the increased velocity region near the wall extends and the bulk velocity reduces. Due to the large variation of the velocity across the tube, the velocity gradient increases, the sign of shear stress changes and an increase of shear stress and turbulent kinetic energy is observed. Now the turbulent diffusion heat transfer has improved, the wall temperature has decreased and enhanced heat transfer is observed.

Figure 2.13 indicates the transformation of the velocity profile and the corresponding shear stress distribution caused by buoyancy and acceleration effects.

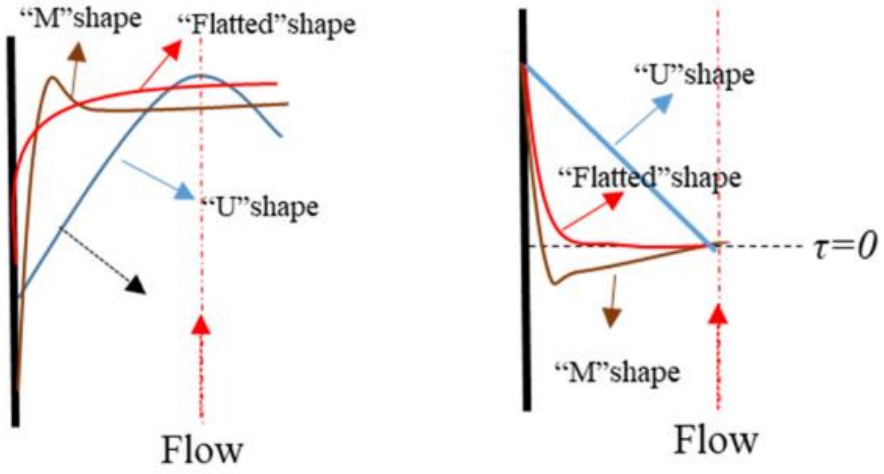

(a) The modifications of velocity profile (b) The corresponding shear stress distribution

Figure 2.13: Transformation of velocity profile and shear stress in vertical upward flows (Zhang, Xu, Liu, & Dang, 2020).

Vertical Downward Flow:

In contrast, downward flows behave differently. Strong buoyancy effects cause the velocity to reduce near the wall and to increase in the bulk region of the flow. A transformation from the normal ''U-shape'' to a sharpened ''U-shape'' velocity profile is observed. The gradient of the velocity across the tube is increased which induces a larger shear stress and improvement of turbulent diffusion. At this kind of flows the wall temperature instead of having a peak it increases monotonically and heat transfer is enhanced.

2.7 Heat Exchangers and Supercritical fluids

In this final section the basics of heat exchangers with supercritical fluids as a working fluid will be discussed and some results from actual supercritical heat exchangers will be analyzed.

One of the most important devices which can be used in the applications mentioned in section 2.2 are heat exchangers. Heat exchangers are devices which transfer energy between fluids at different temperatures and pressures. They can perform both heat recovery from waste heat and heat transfer between working fluids. Printed circuit heat exchanger (PCHE) is an attractive option for supercritical fluid applications. PCHEs are compact heat exchangers with large specific heat transfer area (Ratio of effective heat transfer area to the heat exchanger core volume ~4000 m^2/m^3 and higher) which can withstand high pressures (up to 60 MPa) and wide range of operating temperatures (Khalesi & Sarunac, 2019). Figure 2.14 shows an illustration of a printed circuit heat exchanger.

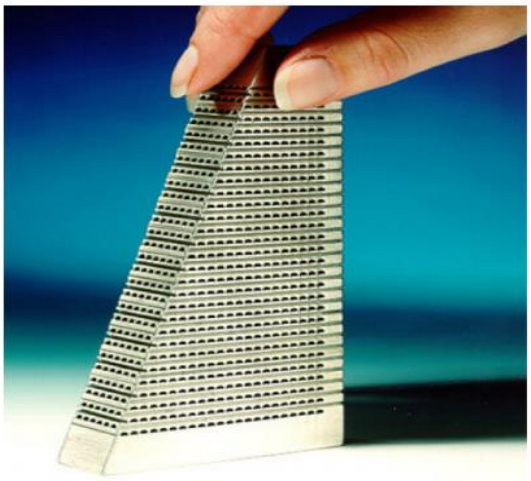

Figure 2.14: Printed Circuit Heat Exchanger (Luo, Flamant, Qi, Xigang, & Pierre, 2011).

Nikitin, Kato, & Ngo, 2006 investigated heat transfer and pressure drop characteristics of a PCHE in an experimental supercritical CO_2 loop by varying the inlet temperature, pressure and mass flow rate of hot and cold fluid. The local heat transfer coefficient of hot and cold fluid and heat loss effect were compared using CFD simulations (The variable thermophysical properties of CO_2 were installed in the simulations using a PROPATH package). Their findings were, overall heat transfer coefficient ~ 300 – 650 W/m^2K, compactness ~ 1050 m^{-1} and maximum power density of ~ 4.4 MW/m^3. Guo & Huai, 2017 investigated the performance of a PCHE with supercritical CO_2 as a working fluid and they investigated how local heat capacity rate ratio, heat transfer entropy generation and axial conduction affect the thermal performance of the heat exchanger. The variable properties of CO_2 were deducted from the National Institute of Standards and Technology (NIST) web book. They found that the local heat capacity rate ratio is very important and affects the local effectiveness of the PCHE, while the variable properties make the calculation of thermal performance very complex. Furthermore, the heat transfer entropy generation is more significant than the frictional entropy and the axial conduction effect is not negligible in these conditions. Meshram, et al., 2016 studied the performance of a PCHE with straight channels in a supercritical CO_2 based Brayton cycle. For their simulations, they used ANSYS Fluent and the variable properties of CO_2 were implemented with NIST database REFPROP. According to their results, the pressure drop of hot side is three times larger than the cold side due to lower density. Also, the Nusselt number is higher at the cold side than the hot side with values in the range of 20-70. Finally, the heat transfer coefficient is affected by Reynolds number and the channel diameter (smaller diameter will result to higher heat transfer coefficient). Kruizenga, et al., 2011 compared experimental data of a PCHE with supercritical CO_2 as a working fluid under cooling conditions with computational results at different system pressure, inlet temperature and heat flux. For their simulations, they used FLUENT 12.0 and the variable thermophysical properties of CO_2 were calculated using the NIST database. Their results were in a very good agreement with computational results. Major finding from their study is the fact that, by decreasing the fluid pressure while staying above the critical pressure the heat transfer and consequently the heat transfer coefficient will increase. Apart from that, the heat flux is directly proportional to the heat transfer and the heat transfer coefficient of the system. Also, they concluded that by increasing the fluid temperature more than the pseudocritical temperature a deterioration in the heat removal will occur which will result in decrease of the system's heat performance.

As mentioned in Section 2.2, engineering systems operating at supercritical conditions have many advantages and can be a promising technology in the future. These studies show that better performances can be achieved but the variable thermophysical properties of supercritical fluids complicate the design and the operation of heat exchangers. Phenomena such as heat transfer deterioration can occur which will result to low heat transfer coefficients and high wall temperatures with catastrophic results. It is very important to better understand how the thermophysical properties of supercritical fluids behave and affect heat transfer in heat exchangers.

3 Governing Equations

The mathematical description of this study will be provided in this chapter. The fundamental concepts that are used, are the conservation laws for a medium in motion (fluid) and a stationary medium (solid). The flow conservation equations are modified based on the Boussinesq approximation. Also, the balanced heat exchanger's equations and terms related to the performance of the heat exchanger are also provided and explained.

3.1 Conservation Laws

A steady fluid flow is described by equations of mass, momentum and energy, also known as the Navier-Stokes. The working fluid will be air and the flow is assumed to be laminar and incompressible where the fluid properties are constant except of the density. Below you can find the continuity, momentum and energy equations (Kundu, Cohen, & Dowling, 2016).

$$\frac{\partial u_i}{\partial x_i} = 0 \quad [1]$$

$$\rho u_j \frac{\partial u_i}{\partial x_j} = -\frac{\partial p}{\partial x_i} + \mu \frac{\partial^2 u_i}{\partial x_j^2} + \rho g_i \quad [2]$$

$$\rho u_j \frac{\partial e}{\partial x_j} = -p \frac{\partial u_i}{\partial x_i} + \rho \varepsilon + k \frac{\partial^2 T}{\partial x_i^2} \quad [3]$$

Important dimensionless numbers that will be used for describing the flow and the heat transfer are the Reynolds and the Nusselt number.

$$\text{Reynolds numver: } Re = \frac{\text{Inertial Forces}}{\text{Viscous Forces}} = \frac{\rho u_o d_h}{\mu} \quad [4]$$

$$\text{Nusselt numer: } Nu = \frac{\text{Convective Heat Transfer}}{\text{Conductive Heat Transfer}} = \frac{h_c d_h}{k} \quad [5]$$

For a stationary medium (solid) the balance equations reduce to the energy equation.

$$0 = k \frac{\partial^2 T}{\partial x_i^2} \quad [6]$$

3.2 The Boussinesq Approximation

In this study the variation of fluid density is calculated based on the Boussinesq approximation, which also treats other properties of the fluid (μ, C_p, k) as constants. The density changes are produced by the temperature variation and according to (Kundu, Cohen, & Dowling, 2016) the Boussinesq approximation applies when the temperature variations in the flow are small. However, in this study higher temperature differences are observed, hence all the fluid's thermophysical properties should depend on the temperature. Based on (Laaroussi, Lauriat, & Desrayaud, 2009) flow reversal occurs with and without variable thermophysical properties. Therefore, the Boussinesq approximation is used for the sake of simplicity.

$$\rho = \rho_o[1 - \beta(T - T_o)] \quad [7]$$

The density variations can be no larger than a few percent of the velocity difference. To evaluate this, the flow field is characterized by a length scale *L*, a velocity scale *U* and a temperature scale δT (Velocity variations of *U* and temperature variation of δT over a distance *L*).

$$\frac{\left(\partial\rho/\partial x\right)u}{\left(\partial u/\partial x\right)\rho} \sim \frac{\left(\delta\rho/L\right)U}{\left(U/L\right)\rho} = \frac{\delta\rho}{\rho} = \beta\delta T \ll 1$$

The density variations are negligible compared to the velocity variations and the incompressible form of the continuity equation can be used.

Further simplification of the momentum equation can be done when applying the Boussinesq approximation. When the flow velocity is zero equation 2 reduces to a balance between the hydrostatic pressure p_s and the hydrostatic density ρ_s.

$$0 = -\frac{\partial p_s}{\partial x_i} + \rho_s g_i \qquad [8]$$

Equation 8 is subtracted from equation 2 and the pressure difference from hydrostatic $p' = p - p_s$ and the density difference from hydrostatic $\rho' = \rho - \rho_s$ appear (Where p' and ρ' pressure and density fluctuations).

$$\rho u_j \frac{\partial u_i}{\partial x_j} = -\frac{\partial p'}{\partial x_i} + \mu \frac{\partial^2 u_i}{\partial x_j^2} + \rho' g_i \qquad [9]$$

All terms are divided by ρ_s and for small density fluctuations $\rho/\rho_s \cong 1$ and $\mu/\rho_s \cong \nu$

$$u_j \frac{\partial u_i}{\partial x_j} = -\frac{1}{\rho_s}\frac{\partial p'}{\partial x_i} + \nu \frac{\partial^2 u_i}{\partial x_j^2} + \frac{\rho'}{\rho_s} g_i$$

The final form of the momentum equation can be seen below. Where ρ_0 is a constant reference value of ρ_s. This equation implies that density changes in the momentum equation are negligible except when they are multiplied with gravity.

$$u_j \frac{\partial u_i}{\partial x_j} = -\frac{1}{\rho_0}\frac{\partial p'}{\partial x_i} + \nu \frac{\partial^2 u_i}{\partial x_j^2} + \frac{\rho'}{\rho_0} g_i \qquad [10]$$

The Boussinesq approximation will be also applied in each term of equation 3 in order to get the simplified form of the energy equation. One important note is that the volume expansion term $p(\nabla \cdot u)$ is not negligible despite being used in the continuity equation where $\nabla \cdot \vec{u} = 0$.

$$-p(\nabla \cdot \vec{u}) = -p\left(-\frac{1}{\rho}\frac{D\rho}{Dt}\right) = \frac{p}{\rho}\frac{D\rho}{Dt} \cong \frac{p}{\rho}\left(\frac{\partial\rho}{\partial T}\right)_p \frac{DT}{Dt} = -p\beta\frac{DT}{Dt}$$

Since air is assumed to be a perfect gas the following formulas can be used: $p = \rho RT$, $C_p - C_v = R$ and $\beta = 1/T$. The volume expansion term simplifies to:

$$-p(\nabla \cdot \vec{u}) = -\rho RT\beta\frac{DT}{Dt} = -\rho(C_p - C_v)\frac{DT}{Dt}$$

Also, by using the definition of the material derivative $\frac{De}{DT} = u_j\frac{\partial e}{\partial x_j}$ and $e = C_v T$ (perfect gas) equation 4 becomes:

$$\rho C_v \frac{DT}{Dt} + \rho\left(C_p - C_v\right)\frac{DT}{Dt} = \rho C_p \frac{DT}{Dt} = \rho\varepsilon - \nabla \cdot \vec{q} \qquad [11]$$

The viscous heating term is also negligible under the restriction of the Boussinesq approximation. A comparison between the magnitude of the left-hand side term and the viscous heating term shows:

$$\frac{\rho\varepsilon}{\rho C_p\left({}^{DT}/_{Dt}\right)} \sim \frac{2\mu S_{ij}S_{ij}}{\rho C_p u_i\left({}^{\partial T}/_{\partial x_i}\right)} \sim \frac{\mu U^2/L^2}{\rho C_p U\left({}^{\delta T}/_{L}\right)} = \frac{\nu U}{\left(C_p \delta T\right)L}$$

In typical situations this term is very small (~10^{-7}) and can be assumed negligible. The final form of the energy equation can be seen below.

$$u_j \frac{\partial T}{\partial x_j} = \frac{k}{\rho C_p}\frac{\partial^2 T}{\partial x_i^2} \qquad [12]$$

Finally, the important equations for describing the fluid flow are the continuity (Eq.1), momentum (Eq.10) and energy (Eq.12) and density equation (Eq.7) and have been derived based on the Boussinesq approximation.

3.3 Counterflow Balanced Heat Exchanger

A balanced counterflow heat exchanger is a heat exchanger where the cold and hot stream have equal flow thermal capacity and they are heading in the opposite direction. To derive the differential equation describing the temperature profiles inside the heat exchanger, the steady-flow energy equation is applied in a control volume of the heat exchanger (Figure 3.1). The steady-flow energy balance simplifies to an enthalpy balance since no external work is done, there is no heat transfer in the system and both kinetic and potential energy are assumed negligible (Mills, 1999).

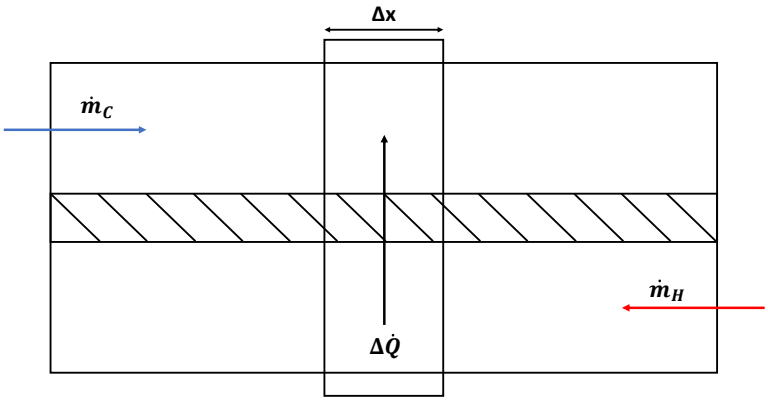

Figure 3.1: Elemental control volume of a coaxial-tube counter-flow exchanger.

For the cold stream,

$$UP\Delta x(T_H - T_C) = (\dot{m}C_p)_C \Delta T_C = \dot{Q} \qquad [13]$$

and for the hot stream.

$$-UP\Delta x(T_H - T_C) = \left(-\dot{m}C_p\right)_H \Delta T_H = \dot{Q} \qquad [14]$$

Where $\dot{Q}$ is the heat transferred from the hot to the cold stream and $\dot{m}C_p$ is the flow thermal capacity of each stream (The amount of heat a stream gains or loses for a temperature change of 1 K). In this study the flow thermal capacity of the cold and hot stream is assumed to be equal

$$(\dot{m}C_p)_C = (\dot{m}C_p)_H = C \quad [15]$$

Dividing each equation [13 and 14] by Δx, rearranging, and letting Δx → 0 gives the differential equations of each stream.

$$C\frac{dT_c}{dx} = UP(T_H - T_C) \quad [16]$$

$$C\frac{dT_H}{dx} = UP(T_H - T_C) \quad [17]$$

Subtracting equation [13] from [14] gives

$$\frac{d(T_H - T_C)}{dx} = 0 \quad [18]$$

Integrating, along the length of the heat exchanger

$$T_H - T_C = T_{H,in} - T_{C,out} = T_{H,out} - T_{C,in} = \text{Constant} \quad [20]$$

For balanced heat exchangers the temperature difference between the hot and cold stream remains constant along the heat exchanger.
Substituting this in equation [13], and again integrating along the length of the heat exchanger

$$\frac{dT_C}{dx} = \frac{UP}{C}(T_{H\,in} - T_{C\,out}) \xrightarrow{\text{yields}} \int_0^L dT_C = \int_0^L \frac{UP}{C}(T_{H\,in} - T_{C\,out})dx$$

$$T_{C\,out} = \frac{1}{\left(1 + \frac{UPL}{C}\right)}\left(T_{C\,in} + \frac{UPL}{C}T_{H\,in}\right) \quad [21]$$

Similarly, from equation [14],

$$T_{H\,out} = \frac{1}{\left(1 + \frac{UPL}{C}\right)}\left(T_{H\,in} + \frac{UPL}{C}T_{C\,in}\right) \quad [22]$$

The equations that describe the temperature of each stream at different positions can then be derived.

$$T_{C\,x} = T_{C\,in} + \frac{UPx}{C}(T_{H\,in} - T_{C\,out}) \quad [23]$$

$$T_{H\,x} = T_{H\,out} + \frac{UPx}{C}(T_{H\,out} - T_{H\,in}) \quad [24]$$

Other important formulas related to the heat exchangers, which will be used in this study are the overal heat transfer coefficient and the logarithmic mean temperature difference.

$$\dot{Q} = UPL\Delta T_{lm} \quad [25]$$

$$\frac{1}{UP} = \left(\frac{1}{h_c w}\right)_{cold} + \frac{l_s}{k_s w} + \left(\frac{1}{h_c w}\right)_{hot} \quad [26]$$

$$\Delta T_{lm} = \frac{1}{\ln\left[\frac{(T_H - T_C)_L}{(T_H - T_C)_0}\right]}\left[(T_H - T_C)_L - (T_H - T_C)_0\right] \quad [27]$$

Furthermore the effectiveness of the heat excahnger is calculated based on:

$$\varepsilon = \frac{\dot{Q}}{\dot{Q}_{max}} = \frac{T_{H\,in} - T_{H\,out}}{T_{H\,in} - T_{C\,in}} = \frac{T_{C\,out} - T_{C\,in}}{T_{H\,in} - T_{C\,in}} \quad [28]$$

Also, for the fluid's temperature at any position inside the heat exchange the bulk temperature is used:

$$T_b = \frac{\int_0^D u_x T dy}{\int_0^D u_x dy} \quad [29]$$

One crucial parameter which will be used in this study for identifying the buoyancy effects inside the heat exchanger is the Grashof number. In this study the Grashof number based on the constant heat flux will be used, as in the work of (Nguyen, Maiga, Landry, Galanis, & Roy, 2004).Its final form is presented below. One important note is that the acceleration of the gravity will vary depending on the orientation. For the vertical upward [Assisted buoyancy] and horizontal cases, g=-9.81 m/s^2 resulting to negative Grashof numbers. For the vertical downward [Opposed buoyancy] cases, g=9.81 m/s^2 resulting to positive Grashof numbers.

$$Gr = \frac{g\beta q d_h^4}{k\nu^2} \quad [30]$$

4 Numerical Methods

In this chapter the geometrical characteristics and thermophysical properties of the printed circuit heat exchanger will be defined. In addition, the boundary conditions used in the simulations along with the OpenFOAM solver will be analysed. In the last two sections of this chapter the heat exchanger and flow reversal validation are presented.

4.1 Design of Printed Circuit Heat Exchanger Geometry

From the literature (Chen, et al., 2013), (Ravindran, Sabharwall, & Anderson, 2010) and (Yoon, Sabharwall, & Kim) it was understood that the most common printed circuit heat exchanger channel geometry are the semi-circular channels. The main focus of this study is the investigation of buoyancy effects inside heat exchangers which are observed regardless of the geometry. Therefore, a more simplified geometry with square channels was chosen. The transformation is achieved by using the suggested formulas from (Ravindran, Sabharwall, & Anderson, 2010) where the semi-circular channels are transformed into rectangular. Figure 4.1 depicts the main parameters used for this transformation.

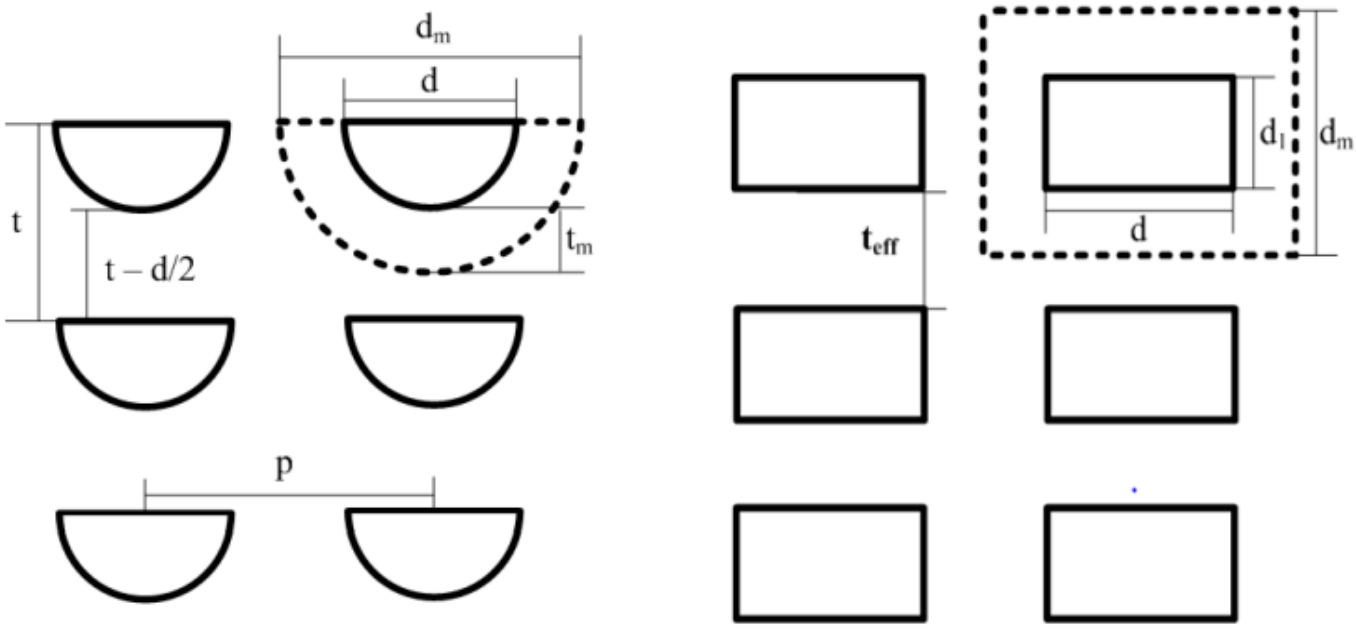

Figure 4.1: Mapping a semi-circular channel to a rectangular channel (Ravindran, Sabharwall, & Anderson, 2010).

The calculation of the square channels is based on this transformation and geometrical characteristics from (Chen, et al., 2013) where *d*=20 mm, *p*=25 mm, *t*=16 mm and *L*=1 m. The area of semi-circular channels and the square channels must be equal.

$$A_{square} = A_{semi-circular} \Rightarrow\ d_l^2 = \frac{\pi d^2}{8} \Rightarrow\ d_l = 12.5\ mm$$

According to (Ravindran, Sabharwall, & Anderson, 2010) for the calculation of d_m the total volume of the alloy of the heat exchanger, the total number of the channels and the length of the heat exchanger are needed. In this study, these parameters are not defined (One cold and one hot channel will be evaluated). As a result, d_m=18.75 mm. The rest of the of the parameters are calculated based on the following formulas.

$$t_m = \frac{d_m - d_l}{2} = 3.125\ mm$$

$$t_{eff} = t - \frac{d_m}{4} = 11.3\ mm$$

Table 4.1 summarises the final dimensions of the square channels of the printed circuit heat exchanger

Table 4.1: Dimensions of the Printed Circuit Heat Exchanger.

d_l [mm]	d_m [mm]	p [mm]	t_m [mm]	t_{eff} [mm]
12.5	18.75	20	3.125	11.3

The next step is the choice of the appropriate printed circuit heat exchanger material. Yoon, Sabharwall, & Kim in their study stated that the most common structural materials of a printed circuit heat exchanger are the nickel-based alloys (Alloy 617, Alloy 800H and Hastelloy N). Table 4.2 outlines the ththermophysical properties of each alloy.

Table 4.2: Thermophysical properties and cost of structural materials of the Printed Circuit Heat Exchanger (Yoon, Sabharwall, & Kim).

Material	ρ [kg/m^3]	k [W/mK]	C_p [J/kgK]	Cost [USD/kg]
Alloy 617	8360	23.9	586	120
Alloy 800H	7940	22.8	460	120
Hastelloy N	8860	23.6	523	124

According to (Yoon, Sabharwall, & Kim) the Alloy 617 has the lowest structural expenses, and it will be the one used in the current study.

4.2 Boundary Conditions

The initial geometry is a rectangle with six boundaries. Boundaries minX and maxX are defined as patch, minY and maxY as cyclic and minZ and maxZ as empty for the 2D simulations or as patch for the 3D simulations. Figure 4.2 shows the initial geometry with the boundaries.

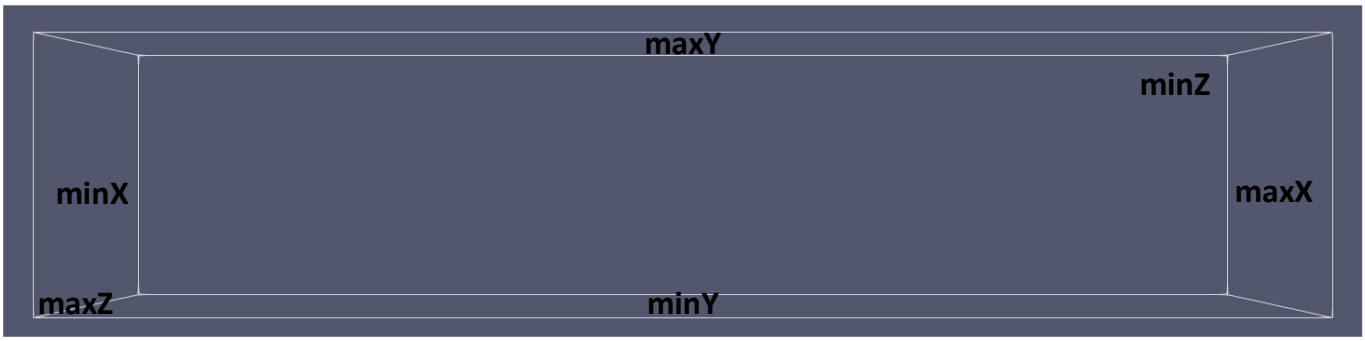

Figure 4.2: Initial heat exchanger geometry.

Using the appropriate commands in OpenFOAM (topoSet & splitMeshRegions) the domain is divided into five different regions (fluid_up/ fluid_down/ solid_up/ solid_mid/ solid_down). Each region has its own boundaries and at the interface of two different regions a coupling boundary is generated. Due to the cyclic boundary at minY and maxY, a boundary is also generated between the top boundary of solid_up and bottom the bottom boundary of solid_down (Behaves as there is another hot stream on top of the cold and another cold stream under the hot). In Figure 4.3 the final heat exchanger geometry is shown.

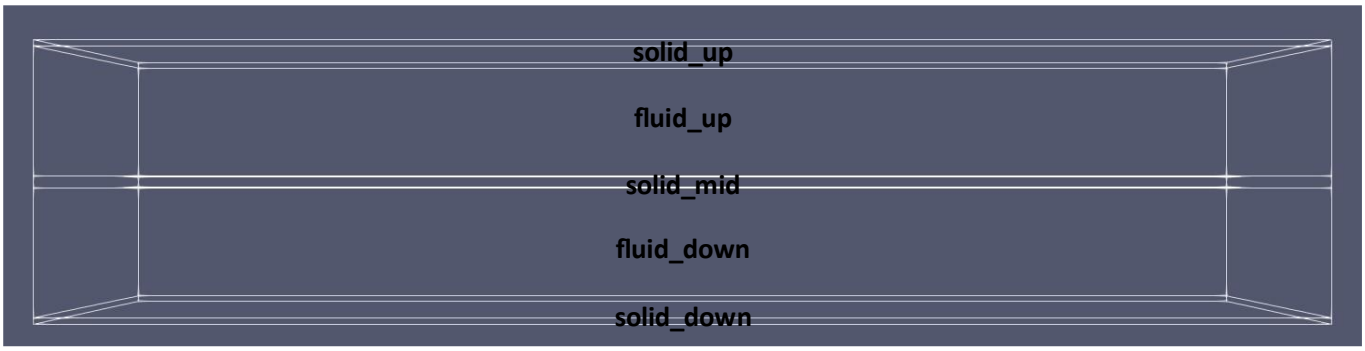

Figure 4.3: Heat exchanger geometry divided into five regions.

For the fluid regions at the inlet of each channel streamwise velocity and temperature are specified

$$T = T_o \text{ and } u = u_x \quad [31]$$

At the channel walls the usual no slip boundary condition is applied.

$$u_x = u_y = u_z = 0 \quad [32]$$

At the outlet of each fluid region zero gradient velocity and zero gradient temperature boundary condition is applied. These conditions can be applied because the flow is assumed to be fully developed and the Peclet number in the channels is large (Pe≫1), which suggests that neglecting diffusion across the outlet is not a bad approximation.

$$\frac{\partial T}{\partial n} = \frac{\partial u_x}{\partial n} = \frac{\partial u_y}{\partial n} = \frac{\partial u_z}{\partial n} = 0 \quad [33]$$

For the solid regions, the boundaries are specified as zero gradient which is an adiabatic boundary condition (e.g., adiabatic walls).

$$\frac{\partial T}{\partial n} = 0 \quad \text{where n is the normal unit vector} \quad [34]$$

At the fluid-solid (f-s) or solid-solid (s-s) interface a conjugate heat transfer boundary condition is applied. At the interface, the temperature of both regions is the same and the heat flux entering one region is equal to the heat flux leaving the other region.

$$T_f = T_s \quad \text{and} \quad k_f \frac{dT}{dn} = -k_s \frac{dT}{dn} \quad [35]$$

4.3 chtMultiRegionSimpleFoam

The chtMultiRegionSimpleFoam solver is a pre-compiled solver available in OpenFOAM. It is a steady state solver for fluid flow and solid heat conduction, with conjugate heat transfer between regions and buoyancy effects. The solver follows a segregated solution strategy. This means that the equations of each region are solved sequentially, and the solution of the preceding equations is used in the next equation. The same strategy is followed at coupling between the fluid and the solid region. Initially, the fluid equations are being solved using the temperature of the solid of the previous iteration. For each fluid region the Navier Stokes equations described in Section 3.1 are solved using a pressure base solver (A pressure equation is used to establish the connection between the momentum and the continuity equation). At first, the density is updated from the continuity equation and an initial velocity field is calculated from the momentum equation. Next, the energy equation is solved (Internal energy or enthalpy, in this study enthalpy is calculated), and the temperature of the new time step is computed. Finally, the pressure equation is solved to ensure mass

conservation. In this step the velocity field and the density (From the Equation of State with the updated temperature) are being corrected. After that, the solid equations are being solved using the temperature of the fluid of the previous iteration. For each solid region the energy equation is solved (Section 3.1), and the temperature of the new time step is calculated. Finally, the temperature of the coupling boundaries (fluid-solid or solid-solid) is calculated based on the temperature and the heat flux of each region (Section 4.2). Figure 4.4 shows a flow diagram which describes the flow of the chtMultiRegionSimpleFoam solver. (OpenFOAMWiki, 2019)

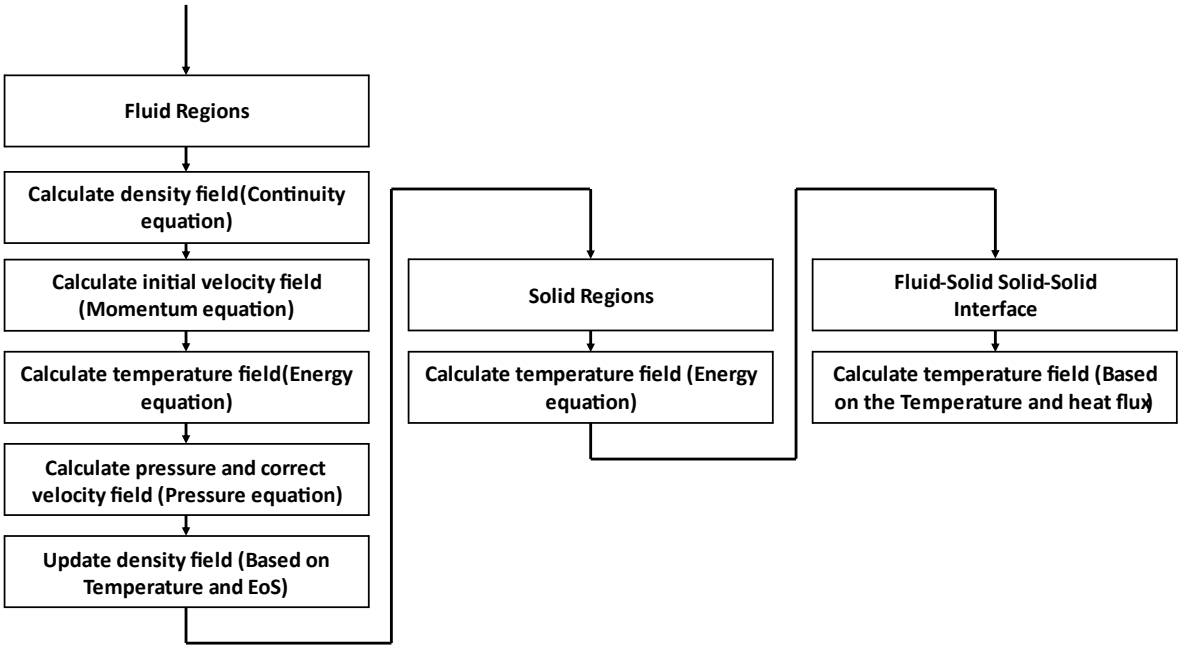

Figure 4.4: Flow diagram of chtMultiRegionSimpleFoam.

4.4 Heat Exchanger Validation

To verify that the numerical results from the OpenFOAM simulations agreed with the analytical solutions and the equations derived in Section 3.3, a 2D heat exchanger validation study is conducted (Figure 4.3 without the top and bottom solid regions, where the top surface of fluid_up and bottom surface of fluid_down behave as adiabatic walls). In this validation all the fluid's thermophysical properties are constant and do not depend on the fluid's temperature. Furthermore, the gravitational acceleration is being neglected (g=0 m/s^2). Table 4.3 summarises the inlet conditions of the cold and hot stream for the validation study.

Table 4.3: Inlet conditions of cold and hot stream.

	u_o [m/s]	T_{in} [K]	ρ [kg/m^3]	C_p [J/kgK]	μ [Ns/m^2]	k [W/mK]
Hot Stream	0.1	353.15	1.25	1005.87	$1.77*10^{-5}$	0.025
Cold Stream	0.1	273.15	1.25	1005.87	$1.77*10^{-5}$	0.025

For calculating the analytical solution values apart from the inlet conditions, the value of the heat transfer coefficient (h_c) of each stream is needed. This value is derived from the Nusselt number which is equal to 5.385 (Constant axial wall heat flux at one surface while the other one is insulated for infinite width geometry (Mills, 1999)). The value of h_c is derived from the formula presented in Section 3.1 (The d_h of this problem where the width is infinite is equal to: d_h=2D). The temperature of the cold and hot stream at each position of the heat exchanger is calculated based on the formulas derived in Section 3.3.

The inlet conditions mentioned in Table 4.3 are used in OpenFOAM to calculate the numerical results. The bulk temperature of each stream is calculated at six different positions (0/ 0.2/ 0.4/ 0.6/ 0.8/ 1 m).

Figure 4.5 shows a comparison between the analytical and numerical results. As can be seen from the graph there is a great agreement between the results.

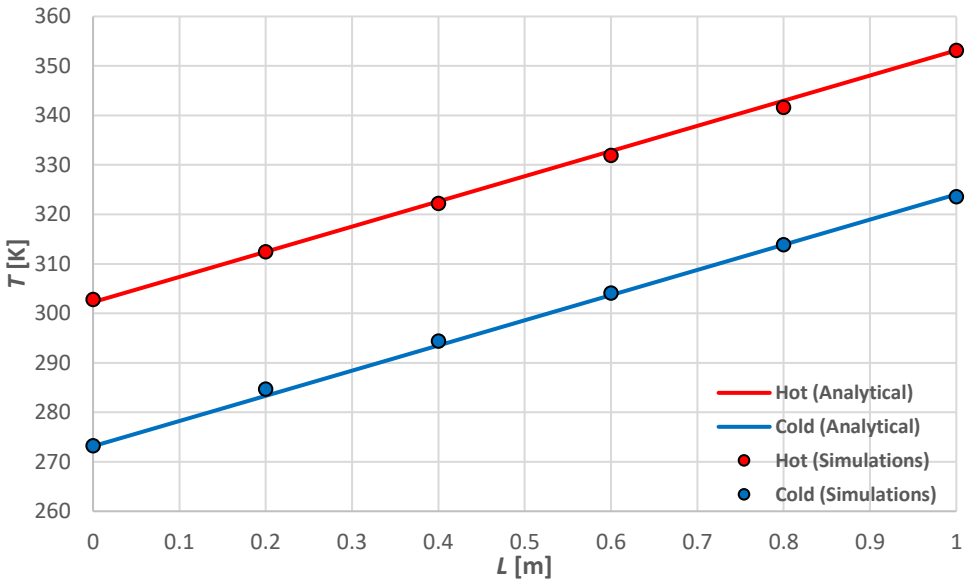

Figure 4.5: Heat exchanger validation between analytical and numerical results.

4.5 Mesh Independence Study

A mesh independence study is also conducted to ensure that the results are independent of the grid size and to identify the optimum number of cells. In this study six different grids (110/ 440/ 1760/ 7040/ 15840 and 28160 Cells) are compared with the analytical solution. At the same time the convergence time of each simulation is calculated (u_x and u_y residuals in the order of 10^{-8} and h residuals in the order of 10^{-6}). Table 4.4 contains results from this study.

Table 4.4: Results from mesh independence study.

	x [m]	0	0.2	0.4	0.6	0.8	1	Total error [%]	Convergence time [s]
Analytical / Cells	T_{Cold} [K]	273.15	283.33	293.50	303.68	313.86	324.04	0	-
	T_{Hot} [K]	302.26	312.44	322.62	332.80	342.97	353.15	0	
110	T_{Cold} [K]	273.24	284.76	294.52	304.30	314.10	323.72	$9.01*10^{-6}$	5
	T_{Hot} [K]	302.58	312.20	322.00	331.78	341.54	353.06	$5.15*10^{-6}$	
440	T_{Cold} [K]	273.22	284.72	294.44	304.17	313.91	323.64	$1.42*10^{-6}$	10
	T_{Hot} [K]	302.66	312.39	322.13	331.86	341.58	353.08	$8.19*10^{-7}$	
1760	T_{Cold} [K]	273.21	284.69	294.41	304.12	313.85	323.56	$9.66*10^{-8}$	20
	T_{Hot} [K]	302.74	312.44	322.17	331.92	341.61	353.09	$3.99*10^{-8}$	
7040	T_{Cold} [K]	273.20	284.66	294.38	304.11	313.84	323.53	$3.56*10^{-7}$	150
	T_{Hot} [K]	302.76	312.46	322.19	331.92	341.64	353.10	$1.70*10^{-7}$	
15840	T_{Cold} [K]	273.19	284.64	294.37	304.10	313.83	323.52	$3.34*10^{-7}$	600
	T_{Hot} [K]	302.77	312.46	322.20	331.93	341.66	353.11	$1.41*10^{-7}$	
28160	T_{Cold} [K]	273.18	284.63	294.36	304.09	313.83	323.52	$3.04*10^{-7}$	1800
	T_{Hot} [K]	302.77	312.46	322.20	331.93	341.67	353.12	$1.05*10^{-7}$	

As can be seen from the table, the solution is independent from the cells number. The most accurate grid size is the one with 1760 cells. For the other three bigger grid sizes a very small difference in the total error is observed but the computational time needed for the solution to converges is relatively higher as the grid size increases. Having in mind both the total error, the convergence time but also the fact that another two solid regions will be added along with buoyancy effects in the main sets of simulations the grid with 7040 cells is picked.

4.6 Flow Reversal Validation

The final part of the numerical methods chapter, the implementation of the Boussinesq approximation with the chtMultiRegionSimpleFoam solver will be evaluated. In this validation the work of (Desrayaud & Lauriat, 2009) will be reproduced in OpenFOAM. In this study flow reversal phenomena for laminar, mixed convection of air in a vertical parallel-plate channel with constant wall temperature are being evaluated. Figure 4.6 shows the results of (a) the streamwise velocity (b) the temperature at four different positions inside the channel (x=0.18/ 0.3/ 0.6/ 1.35m) along the width of the channel and (c) the streamwise velocity at the centreline along the length of the channel (In all three graphs dots represent the paper's results and lines OpenFOAM's results)

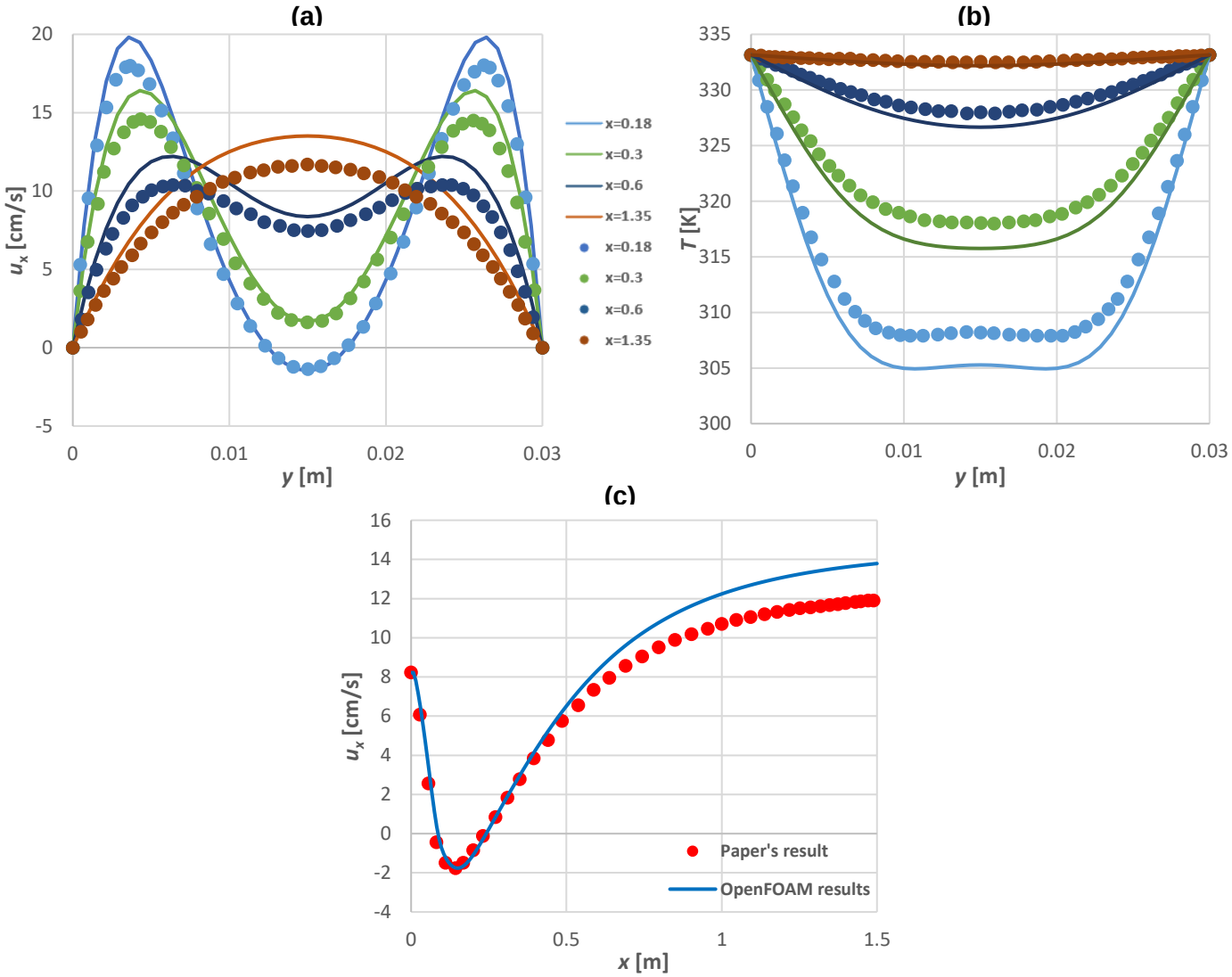

Figure 4.6: Flow reversal validation (a) Streamwise velocity and (b) Temperature along the width of the channel and (c) Streamwise velocity at the centreline along the length of the channel.

By evaluating the OpenFOAM's result the most important conclusion is that flow reversal phenomena and the M-shape velocity profile are reproduced and they are in a very good agreement with the paper's result. A small overprediction of the streamwise velocity (at the outlet of the channel) and a small underprediction of the temperature (at the inlet of the channel) is also observed which can be due to the different reference temperature used in the simulations.

5 Design of Numerical Experiments

In this chapter, using the heat exchanger geometry created in OpenFOAM and the Desrayaud's paper (Desrayaud & Lauriat, 2009) where flow reversal in a vertical channel is observed, the right conditions for achieving similar phenomena inside the heat exchanger will be identified. Also, the choice of parameter variations and thus simulations will be discussed as well as the heat exchanger geometry and flow orientation.

5.1 Flow Reversal inside a Heat Exchanger

According to the paper by (Desrayaud & Lauriat, 2009) the flow reversal phenomena for laminar mixed convection of air going upwards in a vertical channel is observed under certain conditions. In their study, cold air is being heated by the higher temperature walls. The temperature of the walls is kept constant along the entire length of the channel. The main difference between their study and the current study is the condition of heating. In the former, the temperature of the walls is uniform and in the latter, the heat flux through the channel walls is uniform. Therefore, the heat flux in the Desrayaud's paper must be calculated and converted in the heat exchanger geometries. The heat flux is calculated based on (In this formula the total heat load is divided by the length of the channel instead of the total area, because the height of the channel is unknown):

$$q = \frac{Q}{L} = \frac{\dot{m} C_p (T_{out} - T_{in})}{L} = \frac{\rho u_o D C_p (T_{out} - T_{in})}{L}$$

Where T_{out} and T_{in} are the bulk temperatures of the fluid calculated at the inlet and the outlet of the channel. ρ and C_p are calculated from CoolProp (CoolProp) at atmospheric pressure and 308.6 K (average temperature of air). D and L is the channel's width and length and u_o is the inlet velocity of the fluid. Table 5.1 summarizes the value of each parameter.

Table 5.1: Inlet conditions of air in (Desrayaud & Lauriat, 2009).

D [m]	L [m]	ρ [kg/m^3]	u_o [m/s]	C_p [J/kgK]	T_{out} [K]	T_{in} [K]
0.03	1.5	1.145	0.0822	1006.70	332.64	283.54

Finally:

$$q = \frac{\rho u_o D C_p (T_{out} - T_{in})}{L} = 93.1\ W/m^2$$

The under-investigation geometries are 0.03 m (Same geometry as in the Desrayaud paper), 0.025 m, 0.02 m, 0.015 m and 0.01 m (Similar geometry as the one used in the Section 4.4). In each geometry the flow thermal capacity of both streams is kept constant and equal (Balanced heat exchanger), and the Reynolds number of the under-investigation cold fluid is equal to ~ 300. At the same time the inlet temperature of each stream is varied until the desired q = 93.1 W/m^2 is achieved in each heat exchanger. After identifying the right inlet conditions, for each geometry two different simulations are conducted and the induced buoyancy effects are evaluated: **1)** Heat exchanger where both cold and hot fluid have constant thermophysical properties and **2)** Heat exchanger where the Boussinesq approximation is implemented in the cold fluid and it has variable density (the rest of the thermophysical properties are constant), and the hot fluid has constant thermophysical properties. Then these two simulations are compared and the effect of buoyancy on heat exchangers is identified.

The inlet conditions of each case and stream (u_o and T) along with the results of these simulations are summarized in Table 5.2. The deformation of the velocity field of each case at the middle and the outlet of the heat exchanger is presented in Figure 5.1.

Table 5.2: Inlet conditions of air in the heat exchanger.

	Stream	D [m]	u_o [m/s]	T_{in} [K]	ΔQ [W/m]	ΔQ [%]	$\Delta\varepsilon$ [%]	Re [-]	Gr [-]	Flow Deformation
1st Case	Hot	0.03	0.0875	355.15	11.521	7.95	5.30	303.397	11185171	M-shape
	Cold	0.03	0.0675	273.15						
2nd Case	Hot	0.025	0.103	350.15	6.760	4.73	3.26	303.397	5176366	M-Shape
	Cold	0.025	0.081	273.15						
3rd Case	Hot	0.02	0.1275	346.15	3.096	2.17	1.54	302.648	2066319	M-Shape
	Cold	0.02	0.101	273.15						
4th Case	Hot	0.015	0.1685	341.15	0.974	0.69	0.47	303.397	636300	Parabolic
	Cold	0.015	0.135	273.15						
5th Case	Hot	0.01	0.248	337.15	0.302	0.30	0.07	302.648	125163	Parabolic
	Cold	0.01	0.202	273.15						

Where:

$$\Delta\varepsilon = \varepsilon_2 - \varepsilon_1 \ [\%] \quad [33]$$

$$\Delta Q = Q_2 - Q_1 \ [W/m] \quad [34]$$

$$\Delta Q = \frac{Q_2 - Q_1}{Q_1} \ [\%] \quad [35]$$

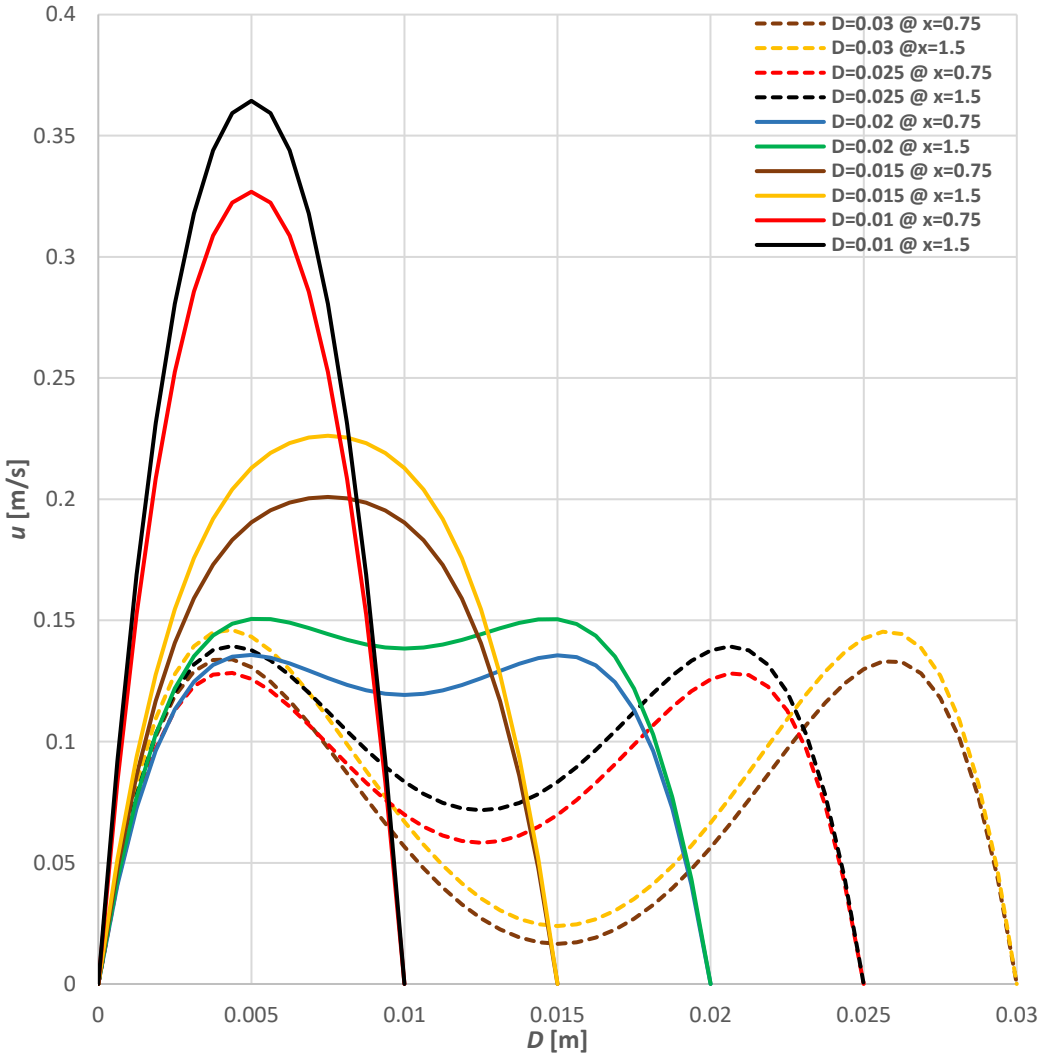

Figure 5.1: Velocity profile at the middle and the outlet of the heat exchanger for the five different geometries.

Results from these simulations are showing a clear dependence of the diameter on the observed buoyancy effects. For the bigger diameter cases (0.03 and 0.025 m) a clear flow deformation is observed. In these cases, the effect of the natural convection is present. The fluid near the walls is being heated first resulting to rapid density decrease. As a result, the flow near the walls region accelerates and decelerates in the center of the channel keeping a constant mass flow rate. Because of the that an M-Shaped velocity profile similar to the Desrayaud paper (Desrayaud & Lauriat, 2009) is observed in both cases. Nevertheless, despite using the same heat flux and Reynolds number as in the Desrayaud paper (Desrayaud & Lauriat, 2009) flow reversal, even in the 0.03 is not observed. For the 0.02 m case the temperature difference between the cold and hot stream is not big enough to fully transform the flow field. As a result, a very weak M-Shape velocity profile is observed where the value of the velocity is more or less constant across the width of the channel. Finally, for the smaller cases (0.01 and 0.015 m) no flow deformation occurs and the expected parabolic velocity profile is observed, suggesting that buoyancy has negligible effect in smaller diameters. Another interesting finding which can be seen in Figure 4.1 is the fact that the velocity profile remains qualitatively constant along the length of the heat exchanger (Small increase in the magnitude of the velocity due to the density increase). In the Desrayaud paper (Desrayaud & Lauriat, 2009; Desrayaud & Lauriat, 2009) M-shaped velocity profile and flow reversal is observed at the inlet of the channel, but the normal parabolic velocity profile returns at the outlet of the channel.

Furthermore, it is notable to refer to the increase of the total heat load (Q [W/m]). By comparing the two different simulations for each case an 8%, 5%, 2% and less than 1% increase is noted for the 0.03 m, 0.025 m, 0.02 m and (0.015 m 0.01 m) respectively. Due to the buoyancy effects and the flow deformation which are present in the first three cases, heat transfer is enhanced. As a result, the effectiveness of the heat exchanger in the bigger diameters is strongly affected. In the smaller diameter cases the flow field and the heat transfer are unaffected, therefore changes in the effectiveness of the heat exchanger are negligible.

Another important parameter which is affected and varies in these different simulations is the Grashof number. Grashof number is directly proportional to the effectiveness increase suggesting that this dimensionless number can be used for determining the importance of buoyancy in heat exchangers. As can be seen from the results for the 0.03 m case the Grashof number is two orders of magnitudes higher than the Grashof number of the smaller cases (0.01 m & 0.015 m) and it is one order of magnitude higher for the 0.025 m and 0.02 m.

From these simulations some important conclusions have been drawn but at the same time new questions arises. Most importantly, buoyancy effects can affect both the flow field and the heat transfer inside the channels of the heat exchangers. Moreover, the diameter is one of the most important parameters in observing buoyancy effects. In bigger diameters, buoyancy effects are present and they can affect the flow field and the heat transfer resulting to an increase of the heat exchanger's effectiveness. Also, these simulations has shown that the Grashof number can be a good indicator of the existence of buoyancy effects because of the big difference between the five geometries. Further studies will be conducted for understanding the relation between Grashof and buoyancy effects in heat exchangers.

5.2 Set of Simulations

After observing different buoyancy effects for the heat exchanger geometry in Section 5.1 it is necessary to investigate the diameter dependence on buoyancy effects. In order to do so three different geometries with channel heights of 0.015, 0.03 and 0.06 m will be compared respectively. Simulations will be conducted in three different orientations: 2D Vertical Upward, where the cold fluid is going upwards and the hot fluid is going downwards (Assisted Buoyancy), 2D Vertical Downward, where the cold fluid going downward and the hot fluid is going upwards (Opposed Buoyancy) and 3D Horizontal. An illustration of the orientations can be seen in Figure 5.2.

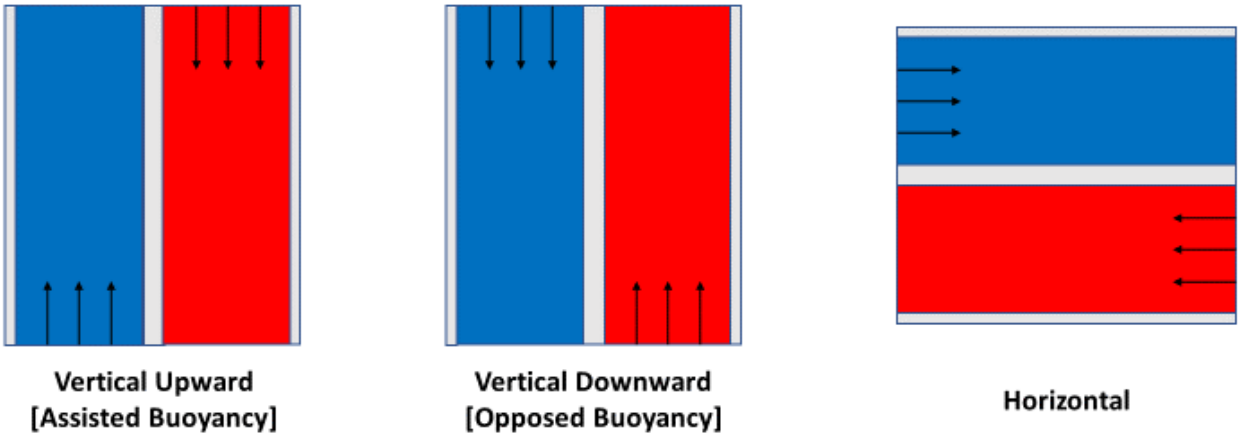

Figure 5.2: Illustration of the three Heat Exchanger orientations.

For each heat exchanger geometry two different set of simulations will be conducted. Table 5.3 summarizes the initial conditions of the first set of simulations. In the first set of simulations the dependence of the Grashof number on the buoyancy effects will be determined. For the three geometries the Reynolds number and the flow thermal capacity will be kept constant and the Grashof number will be kept nearly constant (It depends on the outlet temperature of the fluid and thus maintaining a constant Grashof number requires multiple iterations). In this study balanced heat exchangers are used where the flow thermal capacity of the cold and the hot stream is equal. Therefore, instead of a constant inlet velocity, constant flow thermal capacity is defined. The inlet velocity of the streams is adjusted based on their heat capacity (Which is calculated from Coolprop (CoolProp) based on the inlet temperature of the fluid). To achieve the same order of Grashof number the temperature difference of each geometry will be adjusted. Eight different cases were chosen such that a particular range of Reynolds number was considered and a large spread of the Grashof number. Table 5.4 summarizes the initial conditions of the second set of simulations. In the second set of simulations the performance of heat exchangers under real working conditions will be investigated and the importance of the buoyancy effects will be evaluated. In these simulations the Reynolds number, the flow thermal capacity and the temperature difference between the cold and hot stream will be kept constants for all three geometries and orientations. Three different cases were chosen to get a better understanding of the heat exchanger's performance when affected by the buoyancy effects. For each one of the eleven cases two different simulations are conducted: **1)** In the first simulation both cold and hot fluid have constant thermophysical properties and **2)** In the second simulation the Boussinesq approximation is implemented in both hot and cold fluid while the rest of the thermophysical properties are constant.

Table 5.3: Inlet conditions of air for the first set of simulations.

	$\dot{m}Cp$ [W/mK]	Re [-]	T_{in} [K]	0.015 m	0.03 m	0.06 m
1	2.919	337.108	T_{H_in}	423.15	283.15	274.15
			T_{C_in}	273.15	273.15	273.15
2	3.502	404.530	T_{H_in}	403.15	283.15	274.15
			T_{C_in}	273.15	273.15	273.15
3	3.502	404.530	T_{H_in}	473.15	293.15	275.15
			T_{C_in}	273.15	273.15	273.15
4	4.281	494.425	T_{H_in}	423.15	283.15	274.15
			T_{C_in}	273.15	273.15	273.15
5	4.865	561.847	T_{H_in}	403.15	283.15	274.15
			T_{C_in}	273.15	273.15	273.15
6	5.351	618.031	T_{H_in}	473.15	293.15	275.15
			T_{C_in}	273.15	273.15	273.15
7	5.834	674.216	T_{H_in}	423.15	283.15	274.15
			T_{C_in}	273.15	273.15	273.15
8	5.834	674.216	T_{H_in}	473.15	293.15	275.15
			T_{C_in}	273.15	273.15	273.15

Table 5.4: Inlet conditions of air for the second set of simulations.

	$\dot{m}Cp$ [W/mK]	Re [-]	T_{H_in} [K]	T_{C_jn} [K]
1	2.627	303.397	303.15	273.15
2	3.891	449.477	298.15	273.15
3	5.254	606.794	293.15	273.15

6 Assisted Buoyancy

In this chapter results from the assisted buoyancy simulations will be presented and analysed. An analysis of the heat transfer and the flow characteristics inside this geometry will follow. Table 6.1 and Table 6.2 summarize the parameters and results of the first and second set of simulations in the vertical assisted buoyancy heat exchangers. As explained in the previous chapter, in the first set of simulations the Reynolds number is kept constant and the inlet temperature of each stream is adjusted to achieve a nearly constant Grashof number for each case. In the second set of simulations the temperature difference and the Reynolds number of each case are kept constant for all three geometries.

Table 6.1: Results from the first set of simulations [Assisted buoyancy].

	D [m]	T_{H_out} [K]	T_{C_out} [K]	ΔQ [%]	$\Delta\varepsilon$ [%]	Re [-]	Gr [-]
1	0.06	273.648	273.652	7.20	3.37	337.108	-1568769
	0.03	276.563	297.740	3.88	2.50	337.108	-1376360
	0.015	303.194	383.280	1.46	1.14	337.108	-1678875
2	0.06	273.692	273.608	7.07	3.02	404.530	-1837590
	0.03	276.951	279.352	4.06	2.47	404.530	-1554151
	0.015	302.899	373.552	1.55	1.18	404.530	-1573152
3	0.06	274.175	274.125	12.82	5.54	404.530	-3913627
	0.03	280.323	285.989	7.12	4.31	404.530	-3217781
	0.015	316.901	429.919	1.92	1.47	404.530	-2456408
4	0.06	273.740	273.560	6.75	2.60	494.425	-2012268
	0.03	277.405	278.899	4.18	2.35	494.425	-1760225
	0.015	311.833	384.827	1.90	1.39	494.425	-2138305
5	0.06	273.769	273.531	6.45	2.31	561.847	-2123032
	0.03	277.704	278.600	4.20	2.24	561.847	-1896124
	0.015	310.130	366.460	1.91	1.34	561.847	-2029990
6	0.06	274.384	273.917	11.41	3.93	618.031	-4698496
	0.03	282.309	284.015	7.56	3.85	618.031	-4157911
	0.015	331.270	416.114	2.61	1.81	618.031	-3420969
7	0.06	273.809	273.491	5.93	1.91	674.216	-2280910
	0.03	278.136	278.169	4.15	2.04	674.216	-2094762
	0.015	320.559	376.322	2.30	1.54	674.216	-2692899
8	0.06	274.424	273.876	10.96	3.59	674.216	-4856955
	0.03	282.733	283.591	7.54	3.70	674.216	-4358227
	0.015	334.692	412.856	2.76	1.87	674.216	-3646537

Table 6.2: Results from the second set of simulations [Assisted buoyancy].

	D [m]	T_{H_out} [K]	T_{C_out} [K]	ΔQ [%]	$\Delta\varepsilon$ [%]	Re [-]	Gr [-]
1	0.06	281.571	294.427	39.57	21.12	303.397	-64066227
	0.03	281.592	294.441	7.30	5.76	303.397	-4003376
	0.015	279.486	296.823	0.50	0.38	303.397	-278230
2	0.06	282.528	288.793	48.82	20.42	449.477	-69768795
	0.03	282.481	288.840	8.56	4.91	449.477	-4368878
	0.015	279.975	291.334	0.55	0.37	449.477	-316522
3	0.06	282.477	283.843	49.14	17.67	606.794	-64372121
	0.03	282.216	284.104	7.56	3.79	606.794	-4115879
	0.015	279.788	286.521	0.52	0.31	606.794	-314112

6.1 Flow Characteristics

In the first set of simulation where the Grashof number was kept in the same order of magnitude for the three heat exchangers, different flow characteristics are observed in each channel. Figure 6.1 depicts a comparison of the velocity field at the middle of the heat exchanger (Fully developed flow) between the case where the Boussinesq approximation is implemented and the cases where the density is constant for three different geometries.

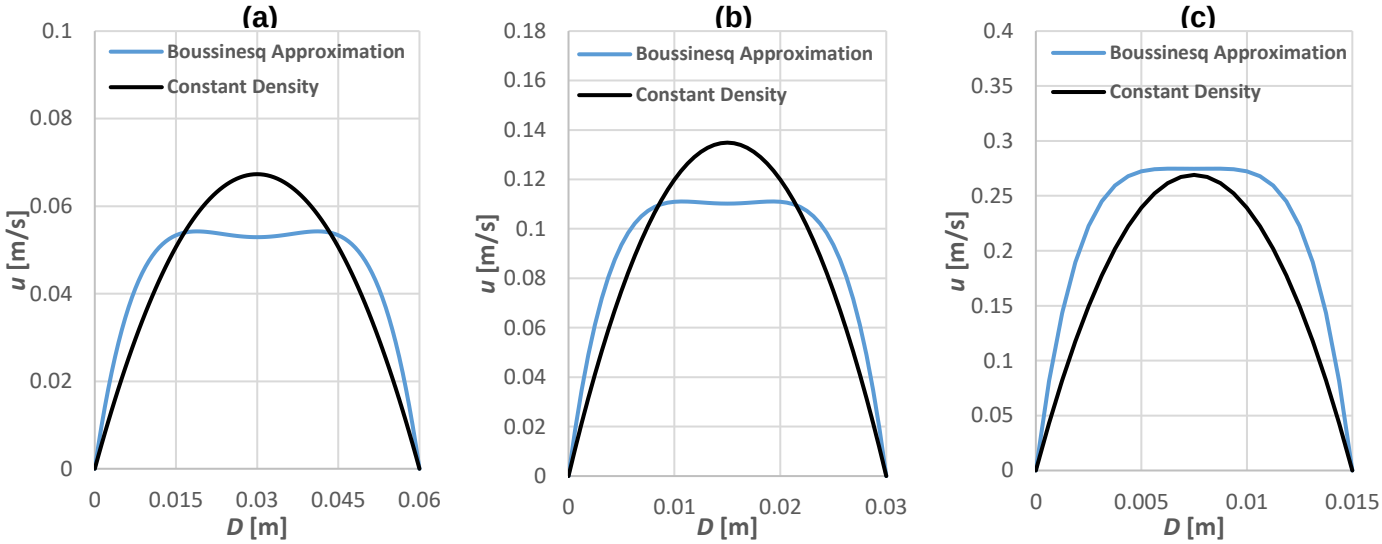

Figure 6.1: Comparison of the velocity field for (a) 0.06 m, (b) 0.03 m and (c) 0.015 m [Assisted buoyancy/ 1st Set of Simulations].

In each geometry the profile of the velocity is different suggesting that the magnitude of the flow deformation and the induced buoyancy effects are directly proportional to the diameter of the channel (Verifying the conclusions of Section 5.1). Instead of the common parabolic velocity profile for the 0.015 m geometry a flat velocity profile is observed with a uniform maximum velocity at the core of the channel. This flat velocity profile is an indication of the weak buoyancy forces which have negligible effect on the flow. In the 0.03 and 0.06 m geometries the cold fluid near the wall is being heated causing an acceleration of the flow near the walls and a deceleration of the flow near the center of the channel. The maximum velocity is shifted from the middle of the channel to the regions adjacent to the walls, resulting to the formation of a weak M-shape velocity profile. The velocity field of the 0.015 m geometry despite having the biggest temperature difference (130 K) becomes flat and not M-shape. The evolution of the velocity profile of the three different geometries can be seen in Figure 6.2. The velocity profile is evaluated in four different positions (0.05/ 0.5/ 1/ 1.45 m). The 0.05 & 1.45 m positions were picked in order to avoid any inlet or outlet effects which would affect the results. The temperature of the cold fluid increases steadily resulting to a uniform and constant increase of the velocity along the heat exchanger (Constant mass flow rate along the heat exchanger). On the other hand, for the 0.06 m geometry despite having only (1 K) temperature difference the velocity profile is changing along the heat exchanger. Initially, a weak M-shape velocity profile is observed which becomes more obvious at the outlet where the velocity near the walls is accelerating. Finally, the 0.03 m geometry is in between the two other cases. A very weak M-shape velocity profile is observed which is more or less constant along the length of the heat exchanger.

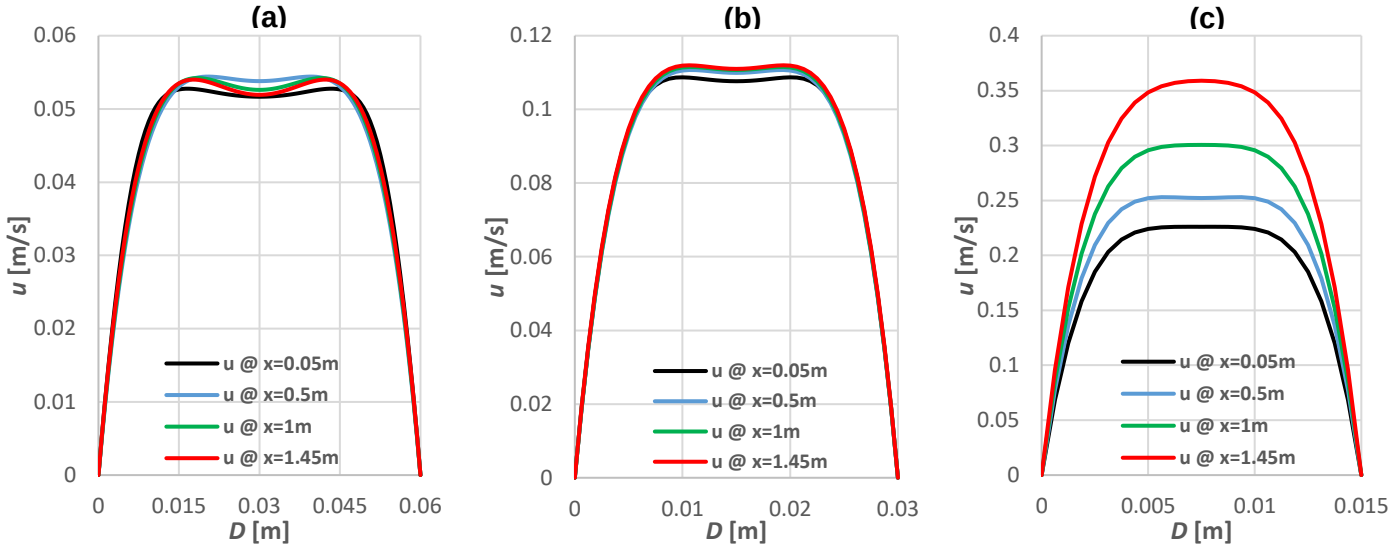

Figure 6.2: Evolution of the velocity profile along the length of the heat exchanger for (a) 0.06 m, (b) 0.03 m and (c) 0.015 m [Assisted buoyancy/ 1st Set of Simulations].

In the second set of simulations where the temperature difference and the Reynolds number are kept constant and the performance of the three heat exchangers was evaluated under real working conditions, a clear difference among the three cases is observed. Results from these simulations are showing the importance and the big dependence of the diameter on the intensity of the buoyancy effects. Figure 6.3 shows a comparison of the streamwise velocity at the middle of the heat exchanger (Fully developed flow) between the case where the Boussinesq approximation is implemented and the cases where the density is constant for three different geometries. The biggest deformation of the velocity profile can be seen in the 0.06 m heat exchanger, where buoyancy effects create an M-Shape velocity profile with flow reversal. In this case velocity, near the walls accelerates resulting to a huge increase of the streamwise velocity in these regions. At the same velocity at the core of the channel decelerates and as a result negative velocity is observed. In the 0.03 m heat exchanger the induced buoyancy effects create an M-Shape velocity profile. Finally, in the 0.015 m heat exchanger buoyancy effects are very weak and the deformation of the velocity profile can be assumed negligible. In all three heat exchangers the transformation of the velocity profile occurs very close to the inlet. The transformed velocity profile of each heat exchanger remains qualitatively unchangeable along the length of the channel.

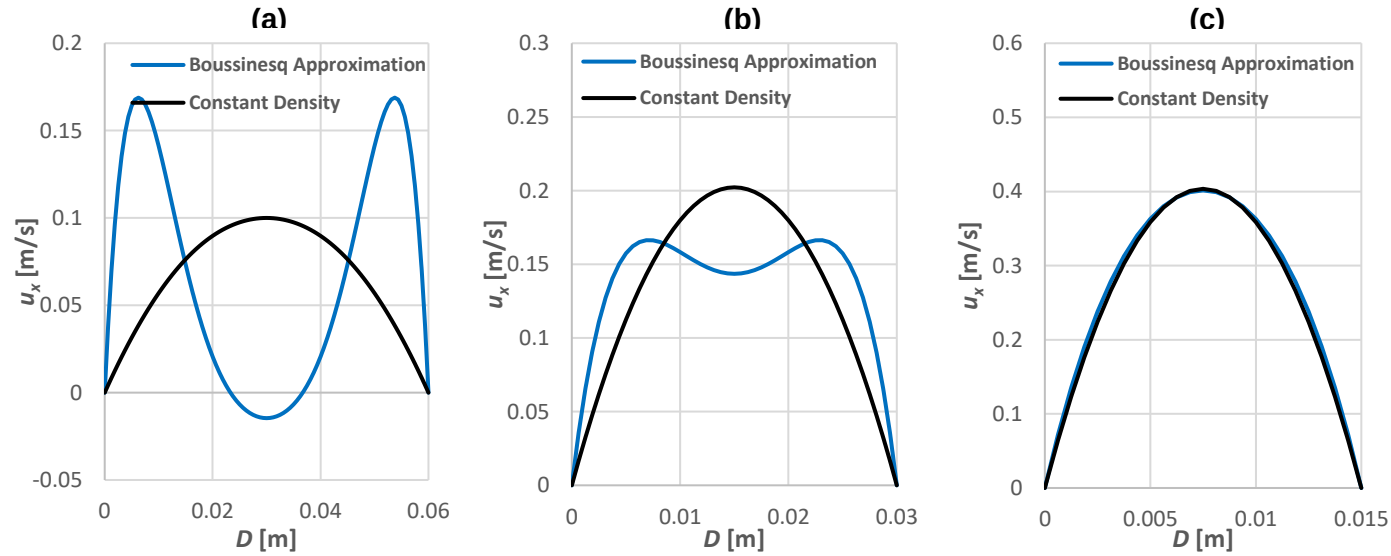

Figure 6.3: Comparison of the streamwise velocity for (a) 0.06 m, (b) 0.03 m and (c) 0.015 m [Assisted buoyancy/ 2nd Set of Simulations].

6.2 Heat Transfer Characteristics

Results from the first set of simulations suggest that the temperature in the core of the channel (Cold stream) at the middle of the heat exchanger is higher in the simulations where the buoyancy effects are significant. This difference for the three geometries varies due to the varying temperature difference which was applied in each geometry. A comparison of the temperature between the two cases for all three geometries can be seen in Figure 6.4.

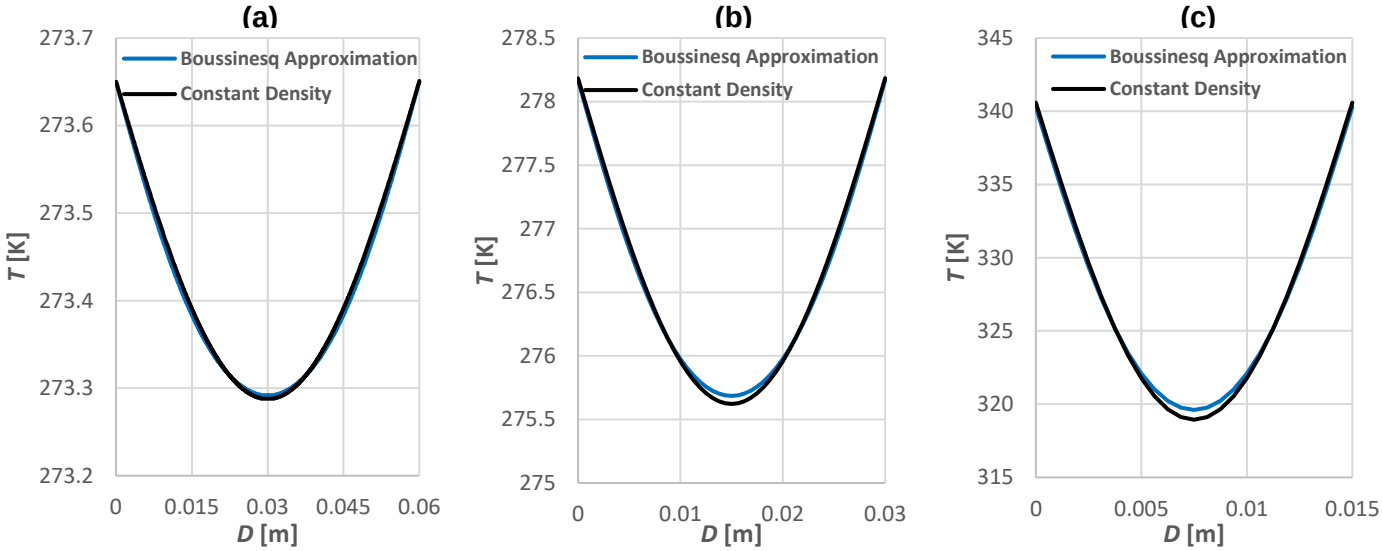

Figure 6.4: Comparison of the temperature for (a) 0.06 m, (b) 0.03 m and (c) 0.015 m [Assisted buoyancy/ 1st Set of Simulations].

Figure 6.5 shows a comparison of the temperature between the two cases for all three geometries. The biggest difference in the temperature is observed in the results from the second set of simulations. In the 0.015 m geometry, the intensity of buoyancy effects is very low. Therefore, the temperature profile of the case where the Boussinesq approximation is implemented is identical to the one where the density is constant. In the 0.03 m geometry the temperature profile deforms as in the first set of simulations. Again, the fluid's temperature is higher in the core of the channel. The biggest transformation of the temperature profile occurs in the 0.06 m geometry. In this heat exchanger instead of the expected reversed parabolic temperature profile, a reversed M-shape temperature profile with very high temperature in the core is observed. Temperatures in the core of the channel can be up to (2 K) higher which is very significant and improves the performance of the heat exchangers.

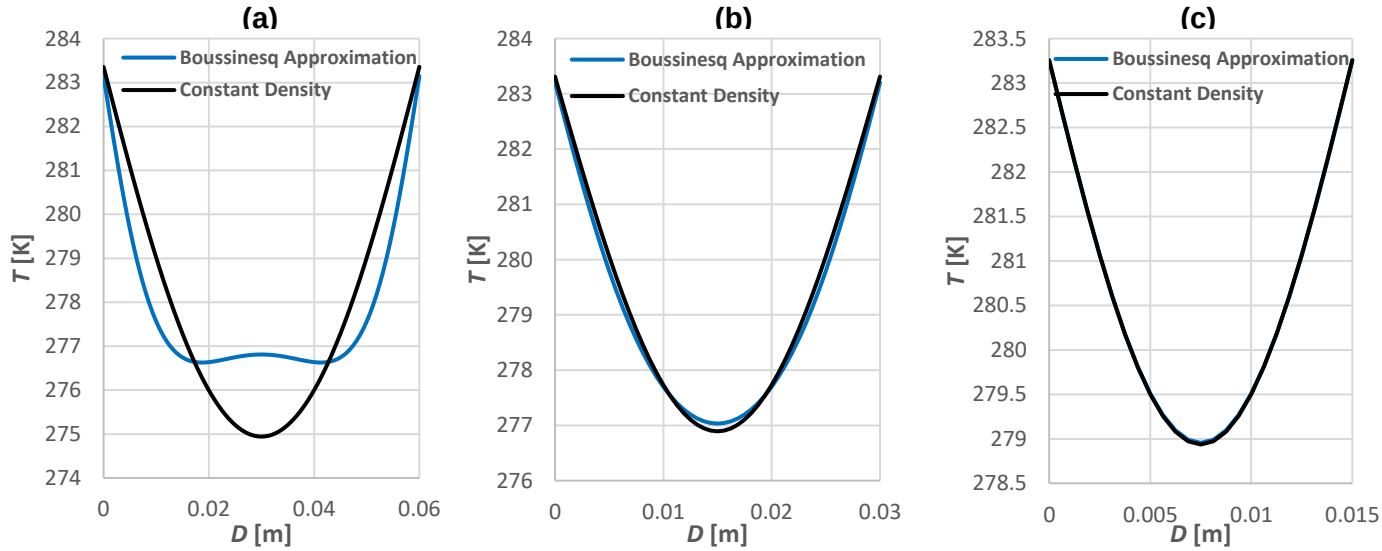

Figure 6.5: Comparison of the temperature for (a) 0.06 m, (b) 0.03 m and (c) 0.015 m [Assisted buoyancy/ 2nd Set of Simulations].

To investigate the mechanism behind the enhancement of heat transfer an order of magnitude analysis is conducted in the 0.06 m geometry in the first set of simulations (In both constant and varying density cases). In this analysis four parameters are compared. The conductive heat transfer, convection heat transfer based on the wall normal velocity and the convection heat transfer based on the streamwise velocity which is divided to the convection heat transfer close to the walls (Between 0-0.01 m and 0.05-0.06 m) and the one in the core of the channel (Between 0.01-0.05 m). Then, the transformation of these four terms is being investigated and their magnitudes is being compared. The units of these four parameters is [W/m] (same as Section 5.1) because the width of the channel is unknown.

Conductive heat transfer: $\int_0^D \frac{-k\frac{dT}{dy}}{D} dy$

Convection heat transfer based on u_y: $\int_0^D \frac{\rho u_y C_p (T_w - T_b)}{D} dy$

Convection heat transfer based on u_x (Close to the wall): $\int_0^{B.C.} \frac{\rho u_x C_p (T_w - T_b)}{Bottom\ wall} dy + \int_{T.C.}^{D} \frac{\rho u_x C_p (T_w - T_b)}{Top\ wall} dy$

Convection heat transfer based on u_x (In the core): $\int_{B.C.}^{T.C.} \frac{u_x C_p (T_w - T_b)}{Core\ length} dy$

Table 6.3 summarizes the results from the order of magnitude analysis. These results suggest that the conduction heat transfer along the height of the channel remains constant for the two simulations. Convection heat transfer based on u_y has increased (twice as high as in the constant density cases) but still its magnitude is very small compared to the other three parameters. Furthermore, the convection heat transfer based on u_x remains also constant. The main difference between the two cases is observed in the third term (convection heat transfer based on u_x close to the walls). In this term a ~27.5% increase is observed due to the formation of the M-shape velocity profile, where the magnitude of the u_x increases radically. The same result holds for all the assisted buoyancy simulations indicating that the main component affecting heat transfer is the increase of u_x close to the walls.

Table 6.3: Results of the order of magnitude analysis.

Case	Conduction HT [W/m]	Convection HT u_y [W/m]	Convection HT u_x (Close to the walls) [W/m]	Convection HT u_x (In the core) [W/m]
Constant Density	4917.12	5.26	22891.49	42788.30
Boussinesq Approximation	4863.46	10.87	29162.39	41784.75

To further quantify the effects of buoyancy on heat transfer the convective heat transfer coefficient (h_c), wall heat flux (q_s), thermal boundary layer (δ_T) and the Nusselt number (Nu #) and are going to be discussed in this section.

Comparison of the convective heat transfer coefficient and the Nusselt number in all three geometries at the fully developed region for both set of simulations can be seen in Figure 6.6 (The black line represents a trend that is qualitatively similar for all the first set of simulation cases and the blue line for the second set of simulation respectively). The heat transfer coefficient is calculated along the length of the heat exchanger based on the heat flux on the wall (q_s), the temperature of the wall (T_s) and the bulk temperature of the fluid (T_b). The h_c is directly proportional to the wall heat flux which is maximum at the inlet of the heat exchanger because of the thin thermal boundary layer. Along the channel the thermal boundary layer is increasing, leading to the decrease of the wall heat flux and of the h_c. As we enter the fully developed region, the thickness of the thermal boundary layer is constant (It is equal to the half height of the diameter) and consequently the wall heat flux and h_c remain constant. A small increase of the h_c is observed at the outlet of the heat exchanger due to the strong heat transfer happening at the inlet of the hot stream. Both wall heat flux and h_c in the Boussinesq approximation simulations are larger than in the constant density simulations. This result suggests an increase in the heat flux and an enhancement of heat transfer. The Nusselt number has a similar behavior. For all the constant density cases the Nusselt number in the fully developed region attains a constant value of ~8.2 which is in great agreement with the Nusselt number for constant axial wall heat flux for infinite width geometries (8.235) from (Mills, 1999). In the first set of simulations where the Boussinesq approximation is implemented, a large increase in the Nusselt number is observed (8.8% for the 0.015 m geometry, 12.6% for the 0.03 m geometry and 14.7% for the 0.06 m geometry) verifying the fact that

convective heat transfer is increased inside the heat exchanger. In the second set of simulations the Nusselt number increases by 1% for the 0.015 m geometry, 21% for the 0.03 m geometry and a massive increase of 125% is observed in the 0.06 m geometry. An increase of the *Nu* # in assisted buoyancy flows while heating is also observed in the work of (Wang, Tsuji, & Nagano, 1994). One of the most obvious and important results of the vertical assisted buoyancy simulations is the fact that enhanced heat transfer is observed in all the simulations of this orientation due to the increase of both Nusselt number and heat transfer coefficient.

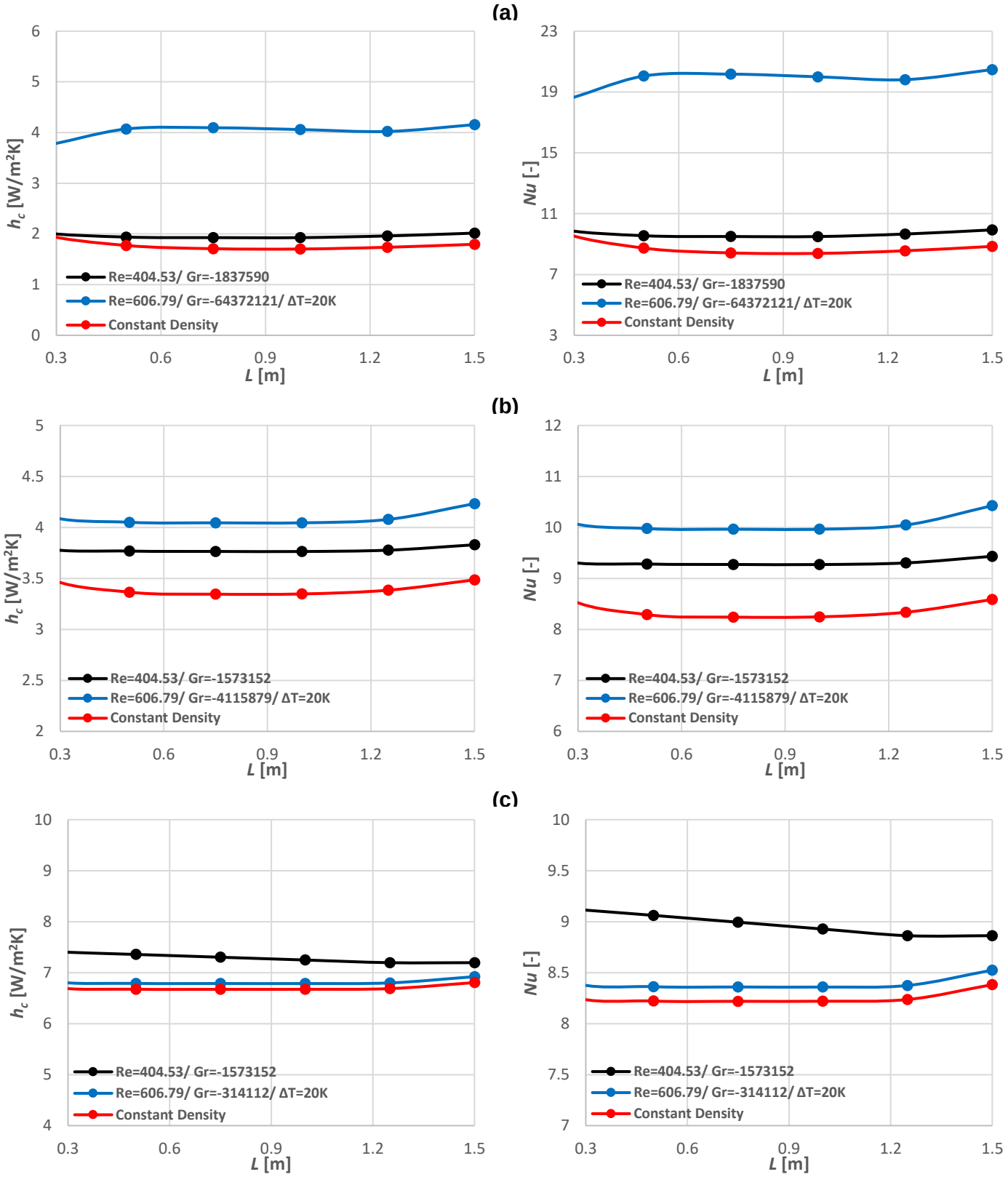

Figure 6.6: Left column: Heat Transfer Coefficient and Right column: Nusselt number for (a) 0.06 m, (b) 0.03 m and (c) 0.015 m in the fully developed region [Assisted buoyancy/ 1st and 2nd Set of Simulations].

7 Opposed Buoyancy

In this chapter results from the opposed buoyancy simulations will be presented and analysed. An analysis of the heat transfer and the flow characteristics inside this geometry will follow. Table 7.1 and Table 7.2 summarize the results of the first (The Reynolds number is kept constant and the inlet temperature of each stream is adjusted to achieve a nearly constant Grashof number) and second (Constant temperature difference and Reynolds number) set of simulations for each case in the vertical opposed buoyancy heat exchangers.

Table 7.1: Results from the first set of simulations [Opposed buoyancy].

	D [m]	T_{H_out} [K]	T_{C_out} [K]	ΔQ [%]	Δε [%]	Re [-]	Gr [-]
1	0.06	273.708	273.596	-7.65	-3.69	337.108	1492691
	0.03	277.092	279.210	-4.65	-2.90	337.108	1265434
	0.015	305.884	380.048	-9.75	-0.76	337.108	1395514
2	0.06	273.740	273.563	-6.95	-3.09	404.530	1657493
	0.03	277.465	278.838	-4.77	-2.80	404.530	1424901
	0.015	306.157	370.313	-1.76	-1.33	404.530	1522034
3	0.06	274.326	273.979	-5.95	-2.61	404.530	3323636
	0.03	281.728	284.328	-6.89	-2.85	404.530	2799557
	0.015	321.764	412.492	-9.45	-1.23	404.530	2182431
4	0.06	273.776	273.526	-6.60	-2.65	494.425	1841141
	0.03	277.887	278.416	-4.81	-2.61	494.425	1612074
	0.015	316.166	380.510	-2.07	-1.51	494.425	2055039
5	0.06	273.798	273.503	-6.29	-2.37	561.847	1964711
	0.03	278.159	278.145	-4.78	-2.46	561.847	1737293
	0.015	313.656	362.946	-1.97	-1.38	561.847	1953017
6	0.06	274.525	273.778	-11.19	-3.95	618.031	3848309
	0.03	283.663	282.687	-5.77	-2.85	618.031	3647746
	0.015	338.319	409.031	-2.52	-1.75	618.031	3250160
7	0.06	273.828	273.472	-5.73	-1.96	674.216	2152327
	0.03	278.545	277.760	-4.65	-2.21	674.216	1923622
	0.015	325.064	371.815	-2.21	-1.48	674.216	2574419
8	0.06	274.555	273.748	-11.24	-3.78	674.216	4000325
	0.03	284.028	282.243	-6.54	-3.12	674.216	3793418
	0.015	341.789	405.703	-2.54	-1.72	674.216	3458382

Table 7.2: Results from the second set of simulations [Opposed buoyancy].

	D [m]	T_{H_out} [K]	T_{C_out} [K]	ΔQ [%]	$\Delta\varepsilon$ [%]	Re [-]	Gr [-]
1	0.06	283.095	294.090	37.21	16.00	303.397	63040678
	0.03	283.443	292.678	-1.68	-0.45	303.397	3669991
	0.015	279.718	296.592	-0.51	-0.41	303.397	275495
2	0.06	282.809	288.673	47.41	19.26	449.477	69219046
	0.03	284.180	286.721	-6.25	-3.54	449.477	3775870
	0.015	280.162	291.147	-0.53	-0.41	449.477	313261
3	0.06	282.854	284.265	55.25	15.69	606.794	66896408
	0.03	283.547	282.541	-7.99	-2.96	606.794	3525839
	0.015	279.911	286.398	-0.48	-0.35	606.794	311213

7.1 Flow Characteristics

In the vertical opposed Buoyancy orientation for the first set of simulation, buoyancy effects produce some unique flow characteristics in each channel. Figure 7.1 depicts a comparison of the velocity field at the middle of the heat exchanger (Fully developed flow) between the case where the Boussinesq approximation is implemented and the cases where the density is constant for three different geometries.

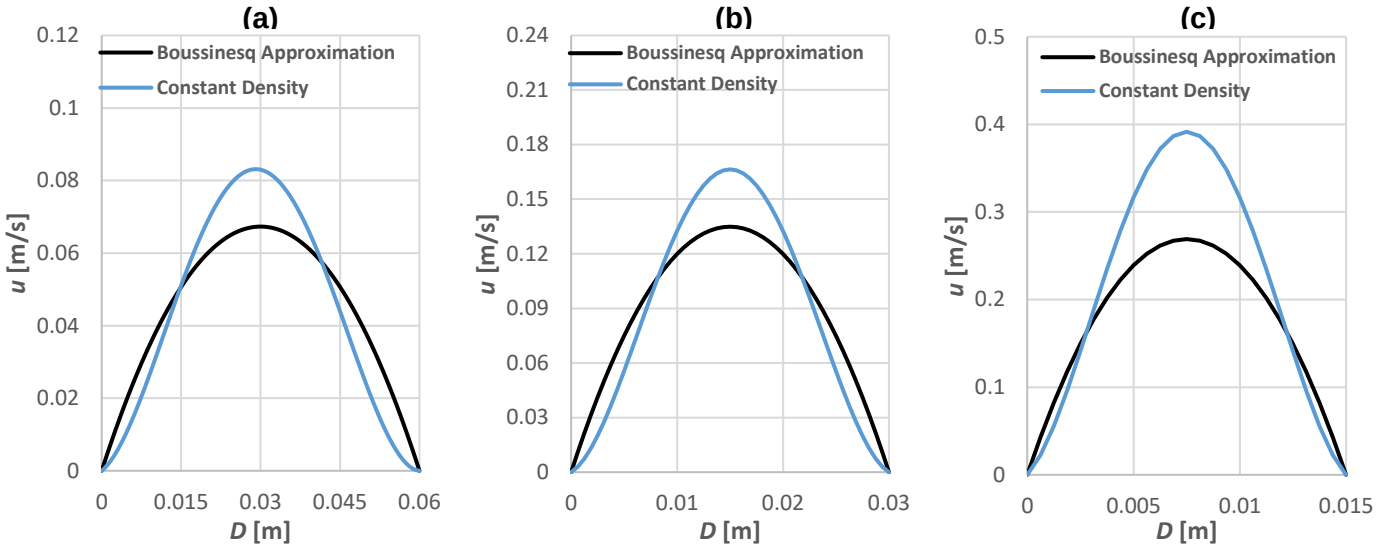

Figure 7.1: Comparison of the velocity field for (a) 0.06 m, (b) 0.03 m and (c) 0.015 m [Opposed buoyancy/ 1st Set of Simulations.

In heated vertical opposed buoyancy flows an opposite flow deformation is observed in comparison to the assisted buoyancy flows. In these simulations instead of the common parabolic velocity profile a bell-shaped velocity profile is observed. The magnitude of the flow deformation and the induced buoyancy effects are again directly proportional to the diameter of the channel (Verifying the conclusions of Section 5.1). The evolution of the velocity profile of the three different geometries can be seen in Figure 7.2 The velocity profile is evaluated in four different positions (0.05/ 0.5/ 1/ 1.45 m). Once again, the 0.05 & 1.45 m positions were picked in order to avoid any inlet or outlet effects. In all these geometries the cold fluid in the core of the channel is being accelerated and the fluid adjacent to the wall is being decelerated. In the 0.015 m geometry the magnitude of the velocity is increasing steadily due to the large temperature difference and the huge density decrease. Despite, having such a large temperature difference (130 K), fluid velocity near the walls is not affected suggesting that the buoyancy effects have minimum effect on the velocity profile. For the bigger geometries (0.03 m and 0.06 m), the magnitude of the velocity remains constant along the heat exchanger due to the small temperature difference (10 K and 1 K respectively) but due to the buoyancy effects a more obvious transformation of the velocity profile is observed.

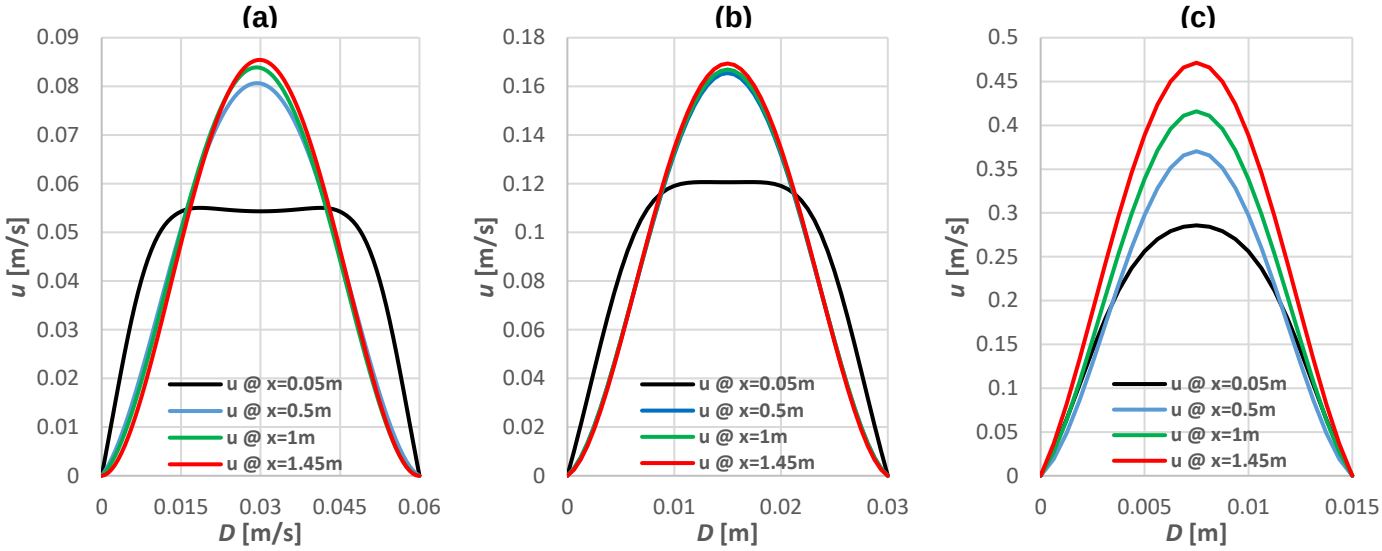

Figure 7.2: Evolution of the velocity profile along the length of the heat exchanger for (a) 0.06 m, (b) 0.03 m and (c) 0.015 m [Opposed buoyancy/ 1st Set of Simulations].

In the second set of simulations where the Reynolds number and the temperature difference was kept constant and the performance of the three heat exchangers is evaluated under real working conditions, an interesting phenomenon is observed. In the 0.015 m geometry both the temperature difference and the diameter of the channel are very small. As a result, the intensity of the buoyancy effects is very low and the velocity profile remains unaffected along the channel. In the bigger geometries (0.03 & 0.06 m) where the induced buoyancy effects are more obvious, instabilities of the flow are produced. The onset of instabilities in vertical opposed buoyancy flows was mentioned and observed experimentally in vertical tubes at low Reynolds numbers by (Harnatty, Rosen, & Kabel, 1958). These instabilities were then investigated by (Nguyen, Maiga, Landry, Galanis, & Roy, 2004) but due to severe limitations of the computer capabilities the extraction of clear conclusions was difficult. The produced instabilities of the streamwise velocity in the 0.06 and 0.03 m geometry can be seen in Figure 7.3 (In the next figures the gravitational acceleration is pointing towards the right-hand side). In the 0.03 m heat exchanger the start of the unstable flow occurs very close to the middle of the heat exchangers. In this section of the heat exchanger the velocity in the core of the channel keeps accelerating and consequently velocity near the walls decelerates. This deceleration of the velocity can lead to flow reversal, negative velocities and recirculation which will create the instabilities in the flow. As a result, instabilities of the streamwise velocity are observed in the rest of the channel. These instabilities create meandering flow which is unsteady over time. In the 0.06 m the intensity of buoyancy effects is producing instabilities of the flow in the entire channel.

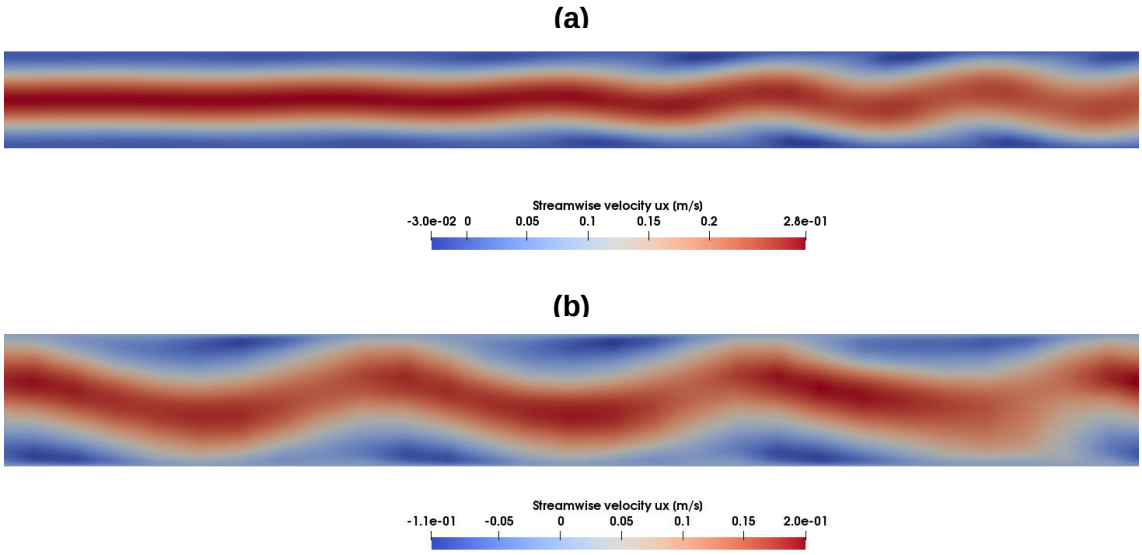

Figure 7.3: Instabilities of the streamwise velocity u_x for (a) 0.03 m and (b) 0.06 m [2nd Set of Simulations].

Figure 7.4 shows the vectors of the streamwise velocity in the 0.06 and 0.03 m geometry. Figure 7.4 (a) is located at x=0.95 m where the transformation of the velocity profile occurs. Small recirculation zones are created at the left and right wall of the heat exchanger. In the 0.06 m geometry the unstable flow is observed in the entire length of the channel. The intensity of the buoyancy effects inside the heat exchanger is larger and therefore clear recirculation zones are formed near the walls of the heat exchanger.

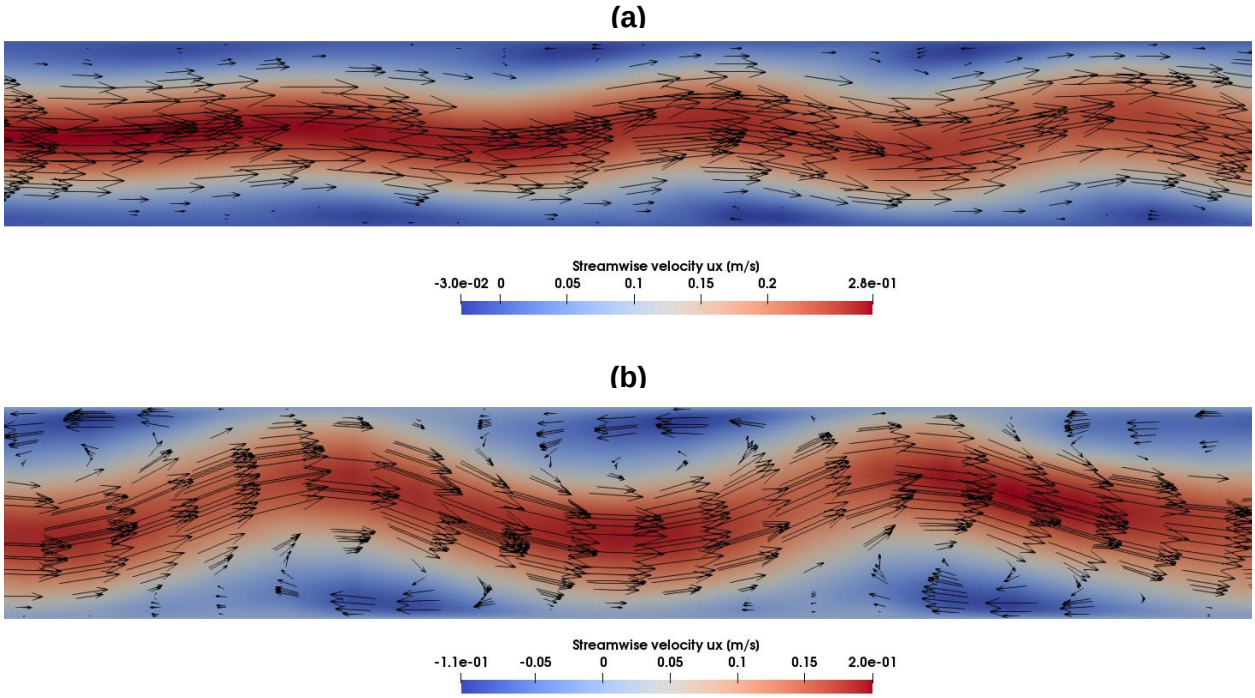

Figure 7.4: Vectors of the streamwise velocity u_x for (a) 0.03 m and (b) 0.06 m [2nd Set of Simulations].

7.2 Heat Transfer Characteristics

Results from the first set of simulations show that the temperature in the core of the channel (Cold stream) at the middle of the heat exchanger is lower in the simulations where the Boussinesq approximation is implemented. A comparison of the temperature for all three geometries can be seen in Figure 7.5.

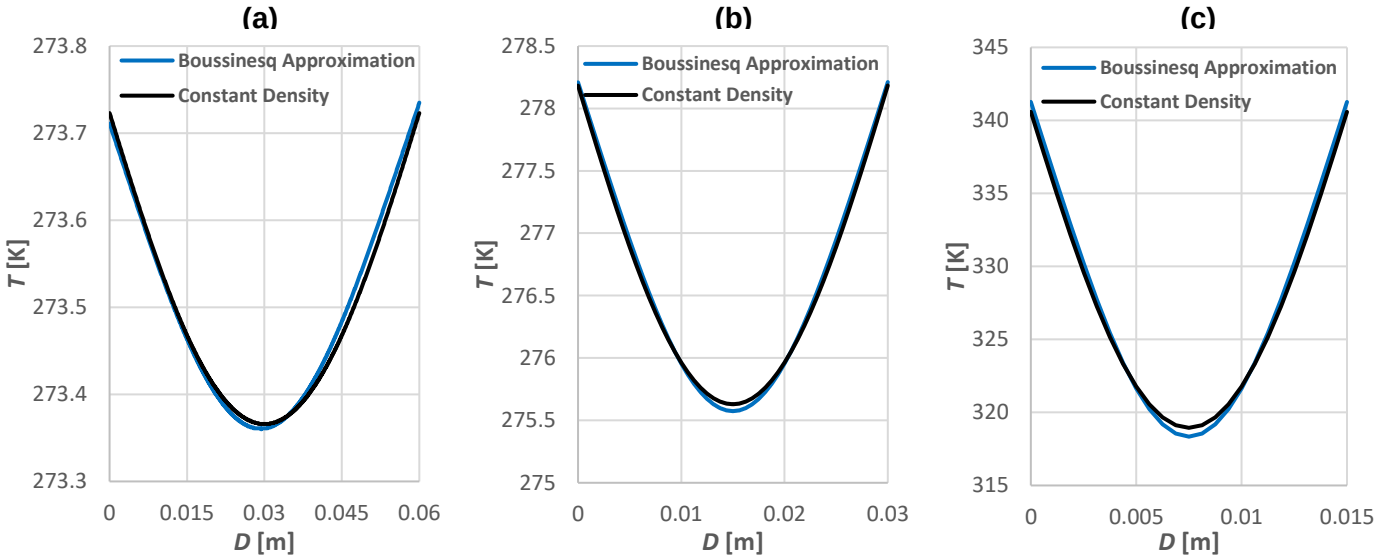

Figure 7.5: Comparison of the temperature for (a) 0.06 m, (b) 0.03 m and (c) 0.015 m [Opposed buoyancy/ 1st Set of Simulations].

In the second set of simulations in the 0.03 m and 0.06 m geometry, as mentioned in Section 7.1 instabilities of the flow field are also observed. As expected, the temperature field is also affected. Figure 7.6 depicts the temperature of the 0.06 m and 0.03 m geometry. Because of the instabilities of the flow and the recirculation zones the heat flux along the channel is not constant. At the positions where there is no recirculation zone the wall normal temperature gradient and thus the heat flux is larger than in the positions where there is recirculation zone.

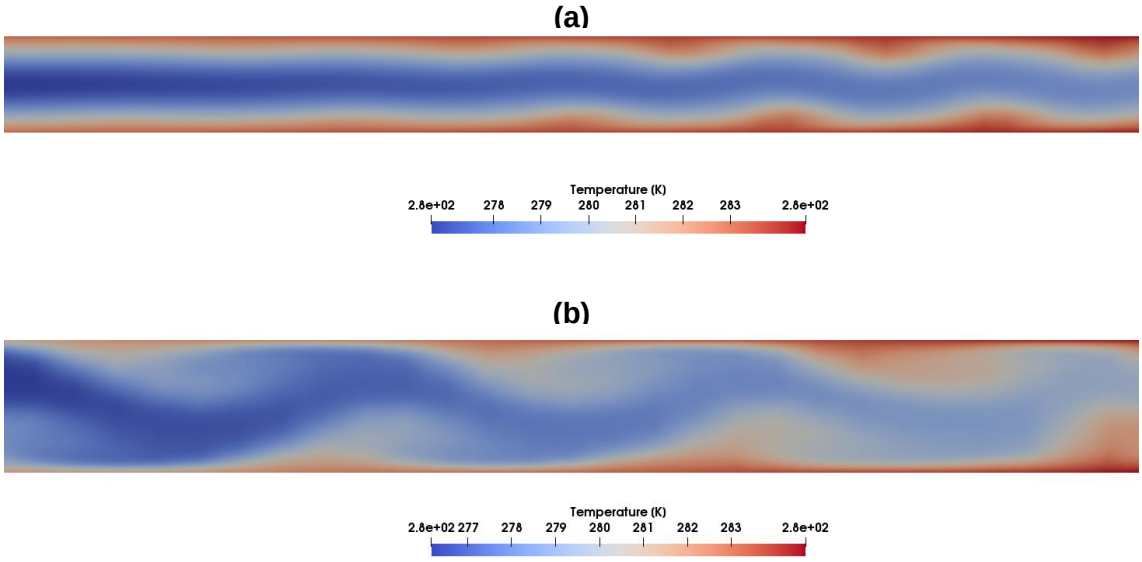

Figure 7.6: Temperature of the instability case for (a) 0.03m and (b) 0.06m [2nd Set of Simulations].

Similar order of magnitude analysis as in Section 6.2 is conducted for the opposed buoyancy simulations (For the 0.06 m geometry first set of simulations and for the 0.06 m geometry second set of simulations). In this analysis the same parameters as in Section 6.2 are calculated based on the same formulas. Table 7.3 summarises the results of this analysis.

In the 0.06 m geometry first set of simulations, once again conduction heat transfer along the height of the channel remains the same for the two simulations. Convection heat transfer based on u_y has increased (six times as in the constant density cases) but still its magnitude is very small and can be assumed insignificant. Moreover, the convection heat transfer based on u_x remains once again constant for both constant density and variable density simulations. The main difference between the two cases is observed in the convection heat transfer based on u_x close to the walls term. This term decreases by ~42.2% due to the formation of the bell-shaped velocity profile, where deceleration of the u_x occurs adjacent to the walls. The same result holds for all the simulations in the vertical opposed buoyancy orientation (Apart from the instability cases) indicating that the main component affecting heat transfer is the decrease of u_x close to the walls.

In the 0.06 m geometry second set of simulations where the instabilities in the flow field and temperature field are observed results from the order of magnitude analysis show a different behavior of these four parameters. The conduction parameter remains again constant in the two simulations. The production of the instabilities inside the heat exchanger strongly affects the remaining three parameters. In the constant density cases the convection heat transfer based on u_x close to the walls is responsible for ~65% of the total u_x convection heat transfer and the remaining 35% comes from the u_x convection heat transfer near the walls. In the simulations where the Boussinesq approximation is implemented these two terms have equal contribution to the total u_x convection heat transfer due to the formation of the instabilities. Apart from that, as shown in Figure 7.4 recirculation zones are created. Consequently, convection heat transfer based on u_y is affected directly. This parameter, in these simulations is three orders of magnitudes larger than in the constant density simulations and is not negligible anymore. These three parameters analyzed in this paragraph are the main reason why enhanced heat transfer is observed instead of deteriorated.

Table 7.3: Results of the order of magnitude analysis.

Case	Conduction HT [W/m]	Convection HT u_y [W/m]	Convection HT u_x (Close to the walls) [W/m]	Convection HT u_x (In the core) [W/m]
Constant Density (1st Set)	4772.14	5.10	22231.23	41530.82
Boussinesq Approximation (1st Set)	4828.01	29.04	12853.03	41023.08
Constant Density (2nd Set)	113830.90	568.60	799389.20	1467442.00
Boussinesq Approximation (2nd Set)	19396.75	856577.80	408086.50	448491.30

Parameters such as the convective heat transfer coefficient (h_c), wall heat flux (q_s), thermal boundary layer (δ_T) and the Nusselt number (Nu #) are crucial in analyzing the intensity of heat transfer inside the heat exchanger and are going to be discussed in this section.

The heat transfer coefficient is once more calculated along the length of the heat exchanger (For the instability cases the time averaged velocity and temperature fields are used in all the calculations). Comparison of the convective heat transfer coefficient and the Nusselt number at the fully developed region of the heat exchanger for all three geometries for both set of simulations can be seen in Figure 7.7 (The black line represents a trend that is qualitatively similar for all the first set of simulation cases and the blue line for the second set of simulation respectively). The h_c follows the same pattern as in the assisted buoyancy cases described in section 6.2. For all three geometries, the wall heat flux and h_c of the constant density simulations are larger than the corresponding parameters of the simulations where the Boussinesq approximation is implemented. Similarly, the Nusselt number is calculated. For all the first case simulations the Nusselt number in the fully developed region attains the same constant value of ~8.2 as in the assisted buoyancy section which agrees with the Nusselt number (8.235) from (Mills, 1999). In the first set of simulations where the Grashof number was kept in the same order of magnitude, a huge decrease in the Nusselt number is observed (-10% for the 0.015 m geometry, -10% for the 0.03 m geometry and -11% for the 0.06 m geometry. Decrease of the Nu # in downward flows while heating is also observed in the work of (Wang, Tsuji, & Nagano, 1994). In the second set of simulations where the focus was on the performance of the heat exchangers under real working conditions different results are observed. In the 0.015 m geometry buoyancy effects hardly affect heat transfer inside the heat exchanger. Therefore, a minimal decrease of the Nusselt number is observed (-1.8%). similar behavior as in the first set is observed. In the 0.03m geometry as mentioned in Section 6.1 the flow initially is stable. In the corresponding part of the heat exchanger h_c and Nusselt number have lower values. Once the instabilities of the flow are produced both these values are increasing. Despite this increase an overall decrease of the average Nusselt number along the channel is observed (-1.4%). In the vertical opposed buoyancy simulations decrease in both the h_c and the Nusselt number is observed implying that deteriorated heat transfer is present in this orientation. In the biggest geometry buoyancy effects are producing instabilities of the flow and recirculation zones in the entire channel of the heat exchanger. As mentioned in the previous paragraphs the wall normal temperature gradient along the channel is not constant. Consequently, parameters such as the heat flux, heat transfer coefficient and Nusselt number vary accordingly along the heat exchanger (Oscillating form of the h_c and the Nu #). The value of both the heat transfer coefficient and the Nusselt number (90% increase) in this simulation is way larger than the constant density cases. This result suggests that the formation of the instabilities and of the recirculation zones produce enhanced heat transfer instead of the expected deteriorated which is observed in the opposed buoyancy simulations.

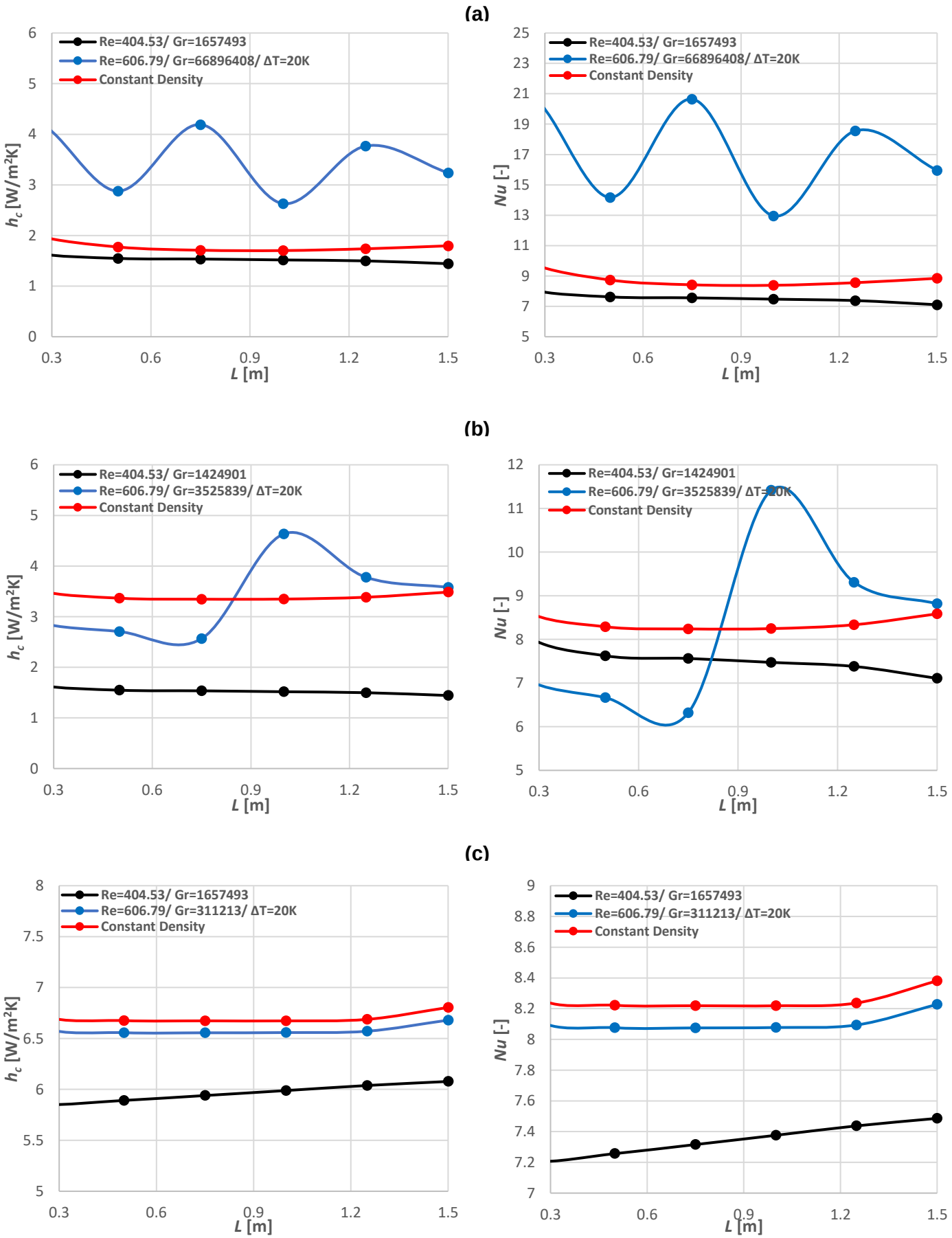

Figure 7.7: Left column: Heat Transfer Coefficient and Right column: Nusselt number for (a) 0.06 m, (b) 0.03 m and (c) 0.015 m in the fully developed region [Opposed buoyancy / 1st and 2nd Set of Simulations].

8.Horizontal

In this chapter results from the horizontal simulations will be presented and analysed. An analysis of the heat transfer and the flow characteristics inside this geometry will follow. Table 8.1 and Table 8.2 summarize the results of the first (The Reynolds number is kept constant and the inlet temperature of each stream is adjusted to achieve a nearly constant Grashof number) and second (Constant temperature difference and Reynolds number) set of simulations for each case in the horizontal heat exchangers.

Table 8.1: Results from the first set of simulations [Horizontal].

	D [m]	T_{H_out} [K]	T_{C_out} [K]	ΔQ [%]	$\Delta\varepsilon$ [%]	Re [-]	Gr [-]
1	0.06	273.669	273.632	5.40	2.47	168.554	-6053
	0.03	276.752	279.546	3.03	1.88	168.554	-2508
	0.015	304.619	391.369	0.88	0.68	168.554	-1449
2	0.06	273.710	273.591	6.02	2.50	202.265	-6635
	0.03	277.113	279.187	3.97	2.30	202.265	-2841
	0.015	304.156	371.820	1.06	0.80	202.265	-1451
3	0.06	274.200	274.103	14.51	6.04	202.265	-14349
	0.03	280.475	285.831	8.62	5.03	202.265	-5967
	0.015	318.442	427.478	1.59	1.21	202.265	-2269
4	0.06	273.756	273.545	6.50	2.41	247.213	-7274
	0.03	277.536	278.769	5.06	2.71	247.213	-3230
	0.015	313.026	382.947	1.76	1.26	247.213	-1973
5	0.06	273.786	273.515	6.09	2.10	280.924	-7635
	0.03	277.818	278.486	5.73	2.89	280.924	-3487
	0.015	311.186	364.803	1.89	1.31	280.924	-1872
6	0.06	274.400	273.900	15.21	4.95	309.016	-17241
	0.03	282.245	284.071	12.48	6.06	309.016	-7851
	0.015	332.200	414.003	3.07	2.10	309.016	-3164
7	0.06	273.833	273.468	3.15	0.97	337.108	-7972
	0.03	278.233	278.071	6.54	3.02	337.108	-3859
	0.015	321.431	374.671	2.82	1.86	337.108	-2488
8	0.06	274.431	273.868	16.44	5.07	337.108	-18020
	0.03	282.628	283.687	13.30	4.32	337.108	-8263
	0.015	335.470	410.869	3.47	2.31	337.108	-3375

Table 8.2: Results from the second set of simulations [Horizontal].

	D [m]	T_{H_out} [K]	T_{C_out} [K]	ΔQ [%]	$\Delta\varepsilon$ [%]	Re [-]	Gr [-]
1	0.06	285.176	291.834	22.61	9.10	151.699	-211057
	0.03	282.166	294.143	7.89	5.02	151.699	-7409
	0.015	279.791	296.505	0.06	0.03	151.699	-257
2	0.06	285.07	286.63	28.29	10.23	224.739	-225543
	0.03	282.593	288.726	10.98	6.00	224.739	-8144
	0.015	280.297	290.996	0.08	0.04	224.739	-292
3	0.06	283.62	282.40	29.67	11.95	303.397	-208989
	0.03	282.160	284.155	12.35	5.89	303.397	-7767
	0.015	280.086	286.209	0.08	0.03	303.397	-288

8.1 Flow Characteristics

In the horizontal heat exchangers, the induced buoyancy effects produce a secondary flow perpendicular to the main flow. Depending on the channels condition (Hot fluid which is being cooled or cold fluid which is being heated) the peak of the velocity will shift either at the top or the bottom surface of the heat exchanger. In the cold stream the peak of the velocity profile is shifted at the bottom surface of the channel and in the hot stream the peak of the velocity moves at the top surface of the channel. A comparison of the velocity field between the first case (Implementation of the Boussinesq approximation) and the second case (Constant density) for three different geometries for both hot and cold fluid can be seen in Figure 8.1. In the figures of this section the 0 in the x axis represents the bottom surface and the 0.015, 0.03, 0.06 the top surface.

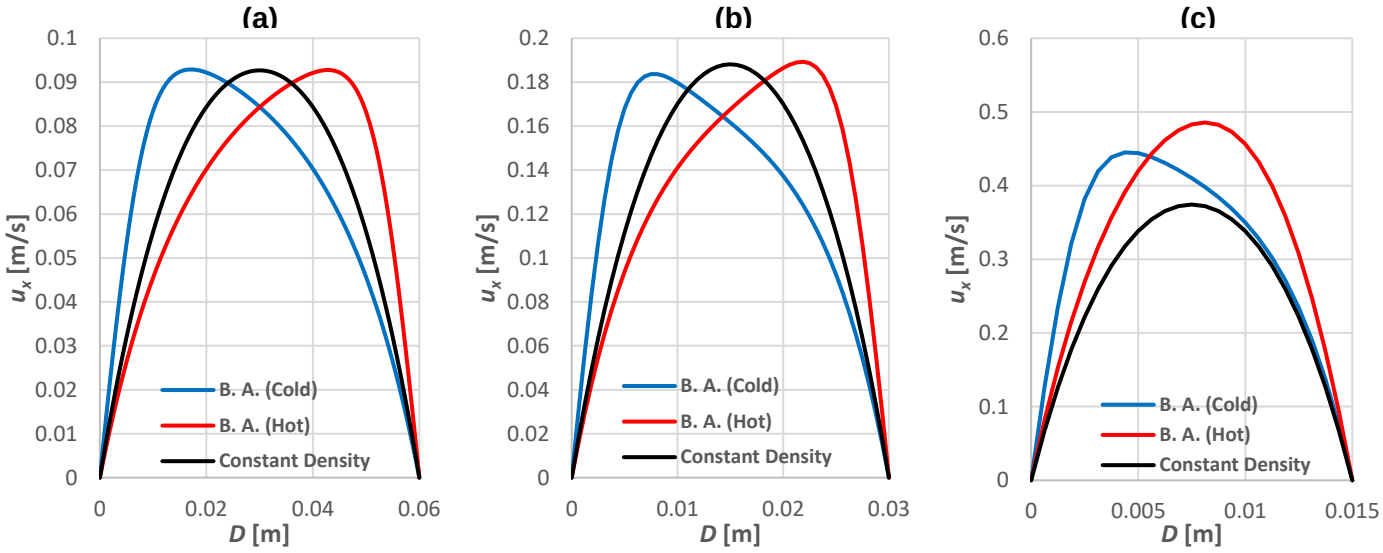

Figure 8.1: Comparison between the streamwise velocity of the hot and the cold stream where the Boussinesq approximation is implemented and the constant density cases for (a) 0.06m, (b) 0.03m and (c) 0.015m [Horizontal/ 1st Set of Simulations].

In these geometries we can divide the fluid flow in to two directions, the horizontal and the vertical. The horizontal flow consists of the streamwise velocity u_x which is the main component of the flow. The vertical-secondary flow consists of u_y and u_z. Buoyancy effects in horizontal flows directly affect the secondary flow and indirectly the horizontal flow. For heating conditions (cold stream), hot fluid with lower density moves at the top surface along the walls and then moves at the bottom surface as the flow approaches the vertical axis. For cooling conditions (hot stream), the opposite phenomenon is observed. The cold fluid with higher density moves downwards along the walls and then upwards as it approaches the vertical axis. The induced secondary flow will then shift the maximum velocity of the cold flow near the bottom surface and of the hot flow near the top surface.

In the first set of simulations creation of the secondary flow is observed in all three geometries. The evolution of the velocity profile of the cold stream for the three different geometries can be seen in Figure 8.2. The velocity profile is evaluated in four different positions. At the inlet of the heat exchanger, at the region where the transformation of the velocity profile occurs and at the fully developed region. In the 0.015 m geometry due to the big temperature difference the initiation of the secondary flow occurs very close to the inlet of the heat exchanger (~ 0.15 m). Then due to the large temperature difference and the density decrease of the fluid, maximum velocity of the fluid keeps increasing along the length of the heat exchanger. For the 0.03 m geometry the initiation of the secondary flow is shifted more downwards (~ 0.3 m). In the largest geometry, despite having only 1 K temperature difference, induced secondary flow is observed close to the middle of the heat exchanger (~0.55 m). Because of the small temperature difference in the 0.03 m and 0.06 m heat exchanger the velocity magnitude remains constant after being transformed.

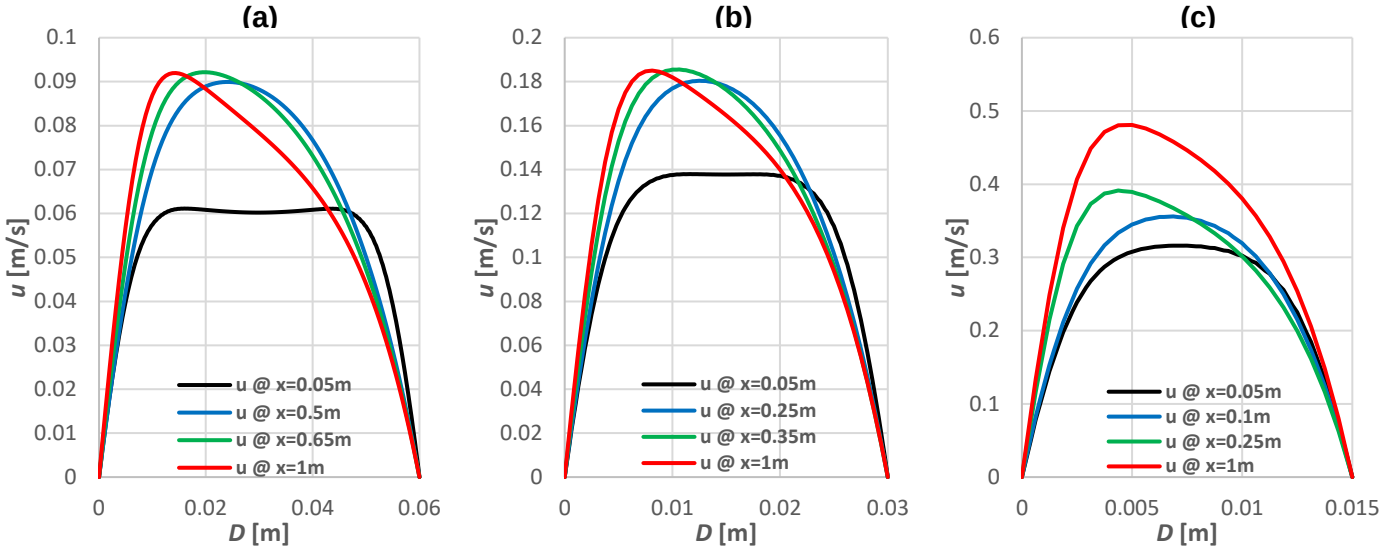

Figure 8.2: Evolution of the velocity profile along the length of the heat exchanger for the cold stream for (a) 0.06 m, (b) 0.03 m and (c) 0.015 m [Horizontal/ 1st Set of Simulations].

In the horizontal simulations where the density is constant, secondary flow is not created and the horizontal flow remains parabolic and unaffected. As a result, the magnitude of u_y and u_z along the length of the heat exchanger is very small and they can be assumed negligible. In the second case of simulations where the density varies buoyancy effects and secondary flow are induced. The velocity magnitude of the secondary flow of the cold and hot stream in the fully developed region is shown in Figure 8.3. In heating conditions (cold stream) the warm and lighter fluid moves upwards along the walls and then downwards when reaching the center of the channel. Because of this motion two recirculation zones are formed near the bottom surface. In cooling conditions (hot stream) the exact opposite phenomenon is observed. The warm and lighter fluid moves upwards through the center of the channel and then downwards along the channel walls. Now the secondary flow forms two recirculation zones at the top surface. The induced secondary flow is observed in all three geometries in both cold and hot stream. The main difference between the three geometries is the fact that the magnitude of the secondary flow in the 0.06 m geometry is one order of magnitude smaller than the magnitude of the streamwise velocity. The secondary flow in the 0.03 m and 0.015 m geometry is two order of magnitudes smaller than the order of magnitude of the streamwise velocity. This result suggests that buoyancy effects have bigger influence in the bigger diameter heat exchangers, where they can affect the velocity profile

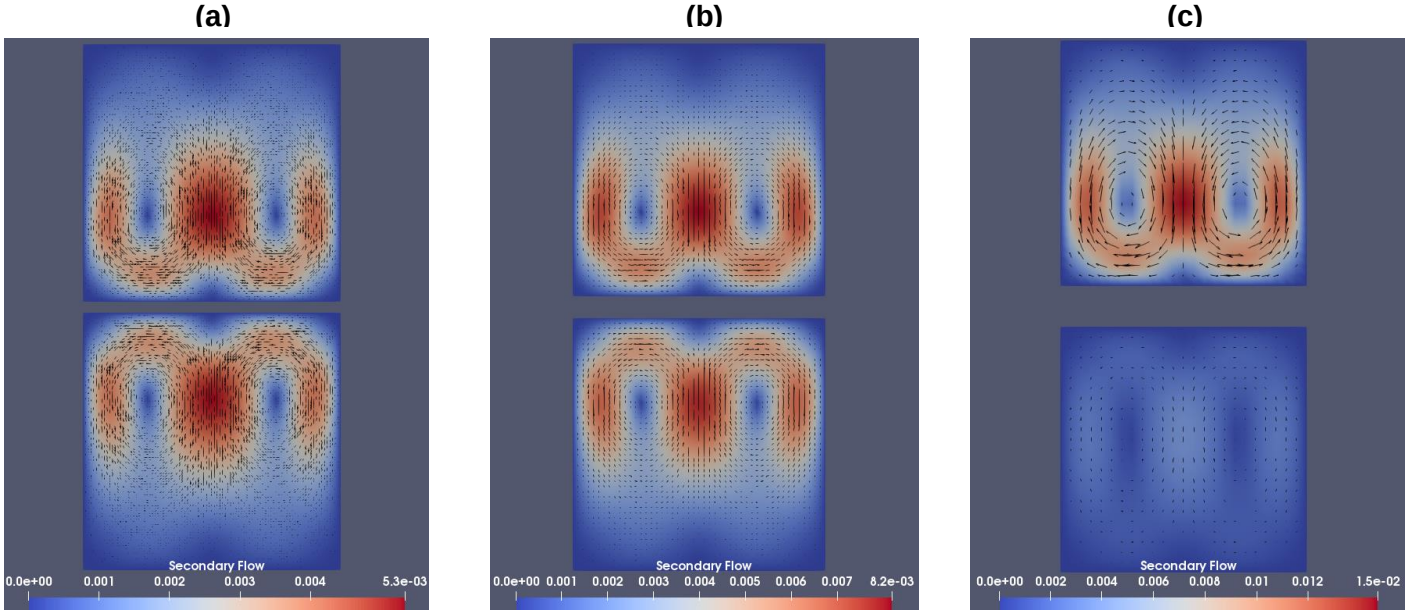

Figure 8.3: Velocity magnitude of the secondary flow at the fully developed region (Top: Cold stream, Bottom: Hot stream) for (a) 0.06 m, (b) 0.03 m and (c) 0.015 m [Horizontal/ 1st Set of Simulations].

In the second set of simulations where the performance of the heat exchangers was evaluated under real working conditions different flow characteristics are observed. Initially, in the smallest heat exchanger (0.015 m) buoyancy effects are very weak. Hence, both u_y and u_z are weak and they fail to produce any secondary flow. In the 0.03 m geometry similar flow characteristics as in the first set of simulations are observed. Now, due to the intense buoyancy effects the start of the secondary flow occurs very close to the inlet of the heat exchanger. Two recirculation zones are formed at the top or the bottom surface depending at the stream and remain unaffected along the length of the heat exchanger. In the biggest geometry where buoyancy effects are very high a different pattern of the secondary flow is observed, and it will be explained using Figure 8.4 (For the cold stream) where the evolution of the secondary flow at the nine different positions along the length of the heat exchanger is shown. Very close to the inlet of the heat exchanger and at the bottom of the surface the first recirculation zones appear.

(1) Due to the strong buoyancy effects the secondary flow instead of being adjacent to the bottom surface moves to the middle of the channel. Furthermore, the velocity magnitude near the walls is higher than the velocity in the centre of the channel. This pattern appears at x=0.25 m and remains the same until x=0.65 m.

(2) Because of the strong buoyancy effects inside the heat exchanger, another two recirculation zones form at the bottom surface. The direction of these vortices is opposite to the direction of the initial vortices. At x=0.7 m the velocity magnitude and the size of the initial recirculation zones is bigger than the size and the velocity magnitude of the new recirculation zones.

(3) At x=0.75 m the new recirculation zones are growing even more. At the same time the initial recirculation zones are being divided and they are shifted closer to the wall. At this position four clear recirculation zones can be observed inside the heat exchanger.

(4) The new recirculation zones are growing even more. Now the velocity magnitude and the size of these recirculation is way higher than the initial's recirculation zones which are being pushed even closer to the walls (x=0.8 m).

(5) At x=0.9 m the intense buoyancy effects are forcing the recirculation zones to move right in the centre of the channel. Still, they have the same size and velocity magnitude. The initial recirculation zones are being pushed in the corners of the channel and they shrink in size.

(6) At x=0.95 m the initial recirculation zones at the corners of the channel start growing again and the new recirculation zones are positioned right the in the centre of the channel. Again, similar to x=0.75 m four clear recirculation zones with the same velocity magnitude and size appear inside the heat exchanger.

(7) At x=1 m the strong buoyancy effects help the initial recirculation zones at the corners which are growing even more. The new recirculation zones at the centre of the channel are being pushed higher in the channel and start dissolving.

(8) The recirculation zones at the centre of the channel have dissolved and they are merging with the recirculation zones at the corners of the channel. At the same time, at the middle of the bottom surface the formation of two new recirculation zones is observed (x=1.05 m).

(9) At x=1.15 m the new recirculation zones are growing again and they have similar velocity magnitude and size as the two initial recirculation zones. At x=1.15 m we observe the same behavior as at x=0.75 m where four clear recirculation zones appear.

The same pattern is repeated in the rest of the heat exchanger. The formation of four vortices inside the channel is an indicator that the flow despite having a very small Reynolds number (~300), the strong induced buoyancy effects can highly transform and affect the flow.

During the transformation of the secondary flow the streamwise velocity is also being affected. As mentioned before, the streamwise velocity is indirectly affected from the buoyancy effects and its deformation is based on the intensity of the secondary flow. In the second set of simulations the streamwise velocity is mostly affected by the motion of the new recirculation zones. Initially, the streamwise velocity behaves as in the first set of simulations. At the inlet of the heat exchanger, it has a parabolic profile and slowly the maximum streamwise velocity is shifted at the bottom surface of the heat exchanger. By the time the two new recirculation zones are created the motion of the streamwise velocity is connected to them. As the new recirculation zones are growing the maximum streamwise velocity is being pushed in the middle of the channel. As the two new recirculation zones move upwards towards the centre of the channel the maximum streamwise velocity is being shifted at the top surface of the heat exchanger. When the recirculation zones at the middle of the channel start dissolving the streamwise velocity regains a parabolic similar profile. With the formation of the new recirculation zones the maximum streamwise velocity is being shifted again at the

bottom surface of the heat exchanger. Similarly to the secondary flow, the streamwise velocity follows the same pattern along the length of the channel.

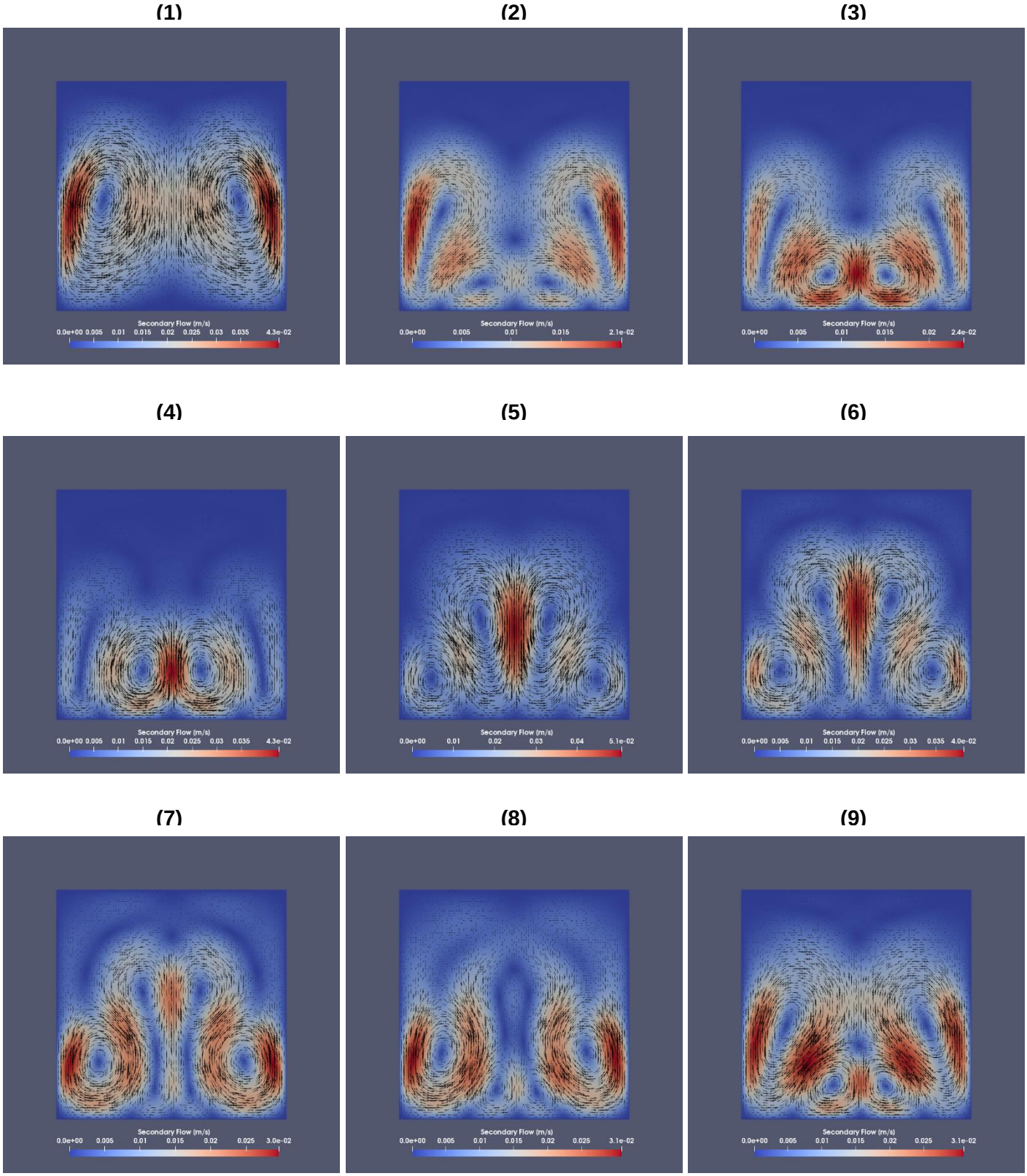

Figure 8.4: Evolution of the secondary flow at: (1) x=0.25 m, (2) x=0.7 m, (3) x=0.75 m, (4) x=0.8 m, (5) x=0.9 m, (6) x=0.95 m, (7) x=1 m, (8) x=1.05 m and (9) x=1.15 m [Horizontal/ 2nd Set of Simulations].

8.2 Heat Transfer Characteristics

In the first set of simulations (constant Reynolds number and nearly constant Grashof number) and specifically in the cold stream the normal reversed parabolic temperature profile is not observed. Instead in all three geometries the minimum of the temperature profile is being shifted at the bottom of the surface. A comparison of the temperature of the cold stream for all three geometries can be seen in Figure 8.5. Also, in all three geometries the minimum of the temperature is higher than the corresponding minimum of the cases where the density is constant. Another important observation can be viewed in the 0.015 m geometry by comparing the constant density temperature line and the Boussinesq approximation line. At the bottom surface the temperature is lower, while at the top surface is higher than in the constant density case. The same phenomenon is present in 0.03 m and 0.06 m geometry but because of the small temperature difference between the cold and hot stream this decrease in the bottom surface and the increase in the top surface is not visible in these graphs.

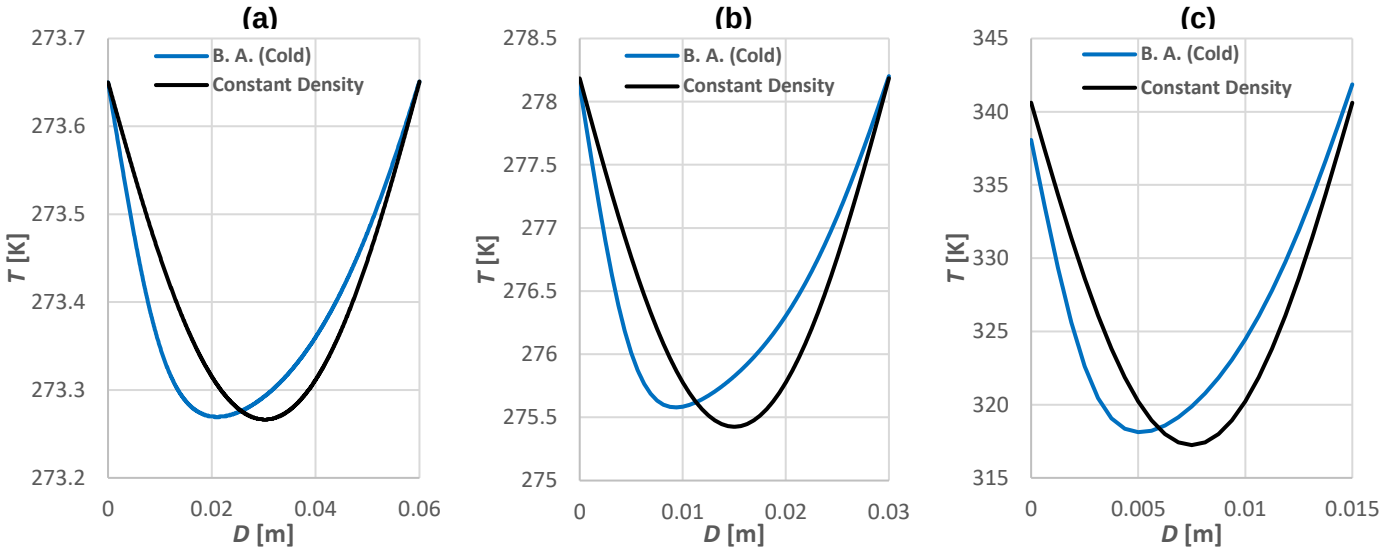

Figure 8.5: Comparison of the temperature for (a) 0.06 m, (b) 0.03 m and (c) 0.015 m [Horizontal (Cold Stream)/ 1st Set of Simulations].

In the second set of simulations where the focus was on the performance of the heat exchangers under real working conditions (Constant Reynolds number and constant temperature difference) the temperature profile for the three geometries varies. Figure 8.6 shows a comparison of the temperature of the cold stream for all three geometries at the middle of the heat exchanger. In the 0.015m geometry the weak buoyancy effects hardly affect the temperature profile. Instead of the normal reversed temperature profile, the minimum of the temperature profile is shifted slightly towards the bottom surface. In the 0.03m geometry where the intensity of the buoyancy effects is higher, deformation of the temperature profile is observed. The minimum of the temperature profile is shifted even closer to the bottom surface compared to the first set of simulations. Furthermore, the minimum which is observed is (1 K) higher than the corresponding minimum of the constant density cases. In the 0.06 m geometry the temperature profile is strongly affected by the secondary flow and the formation of the two recirculation zones as mentioned in Section 8.1. Therefore, the temperature profile is also distorted. The mechanism behind the deformation of the temperature profile will be analyzed in the next section.

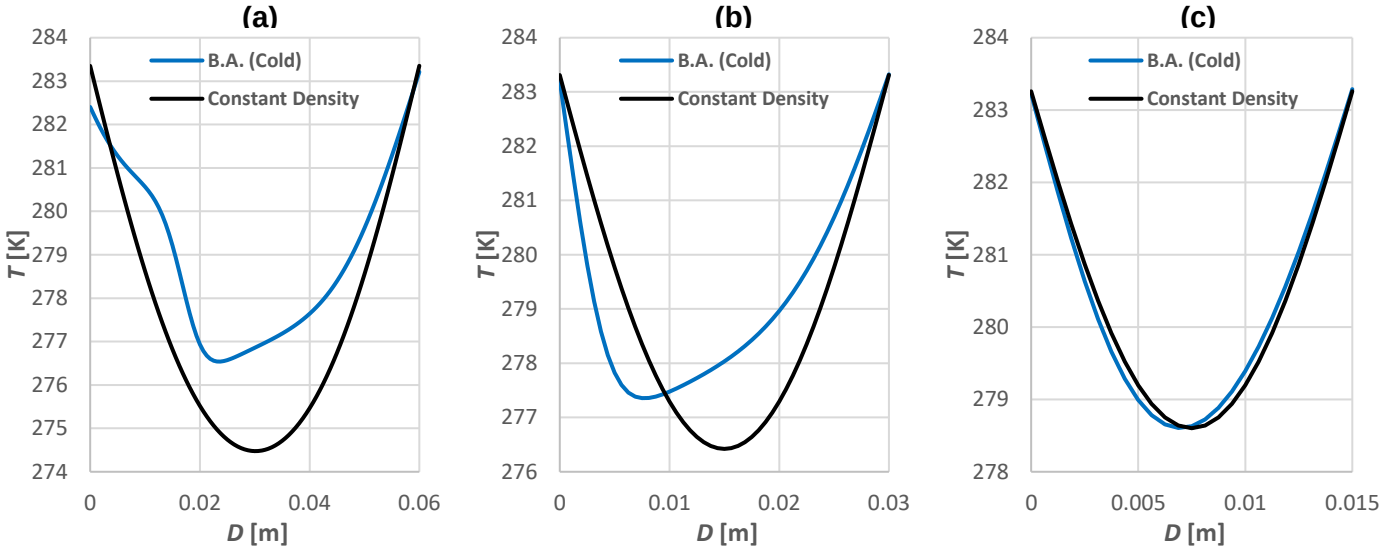

Figure 8.6: Comparison of the temperature for (a) 0.06 m, (b) 0.03 m and (c) 0.015 m [Horizontal (Cold Stream)/ 2nd Set of Simulations.

At the inlet of the 0.06 m heat exchanger and until the formation of the two new recirculation zones occurs the heat transfer in the channel is as described in section 8.1. Warm fluid from the bottom surface is being transported in the core of the channel with the help of the secondary flow, through the walls of the heat exchanger. As expected, the formation of the two new recirculation zones has a significant influence on the velocity field and heat transfer inside the heat exchanger. Figure 8.7 shows the evolution of the secondary flow and the temperature at three different positions (x =0.75 m/ x=0.8 m/ x=0.9 m). **a)** The temperature at the middle of the heat exchanger has increased. Therefore, warm and lighter fluid moves upwards towards the core of the channel. **b)** At x=0.8 m, the size of the new vortices has increased. At the same time the temperature which is enclosed in the middle of the vortices is very high because is being dragged from the hot bottom surface of the channel. **c)** At this point the two recirculation zones in the middle of the heat exchanger are pushed towards the centre of the channel. The heat which is carried with the recirculation zones is being diffused in the cold core of the channel.

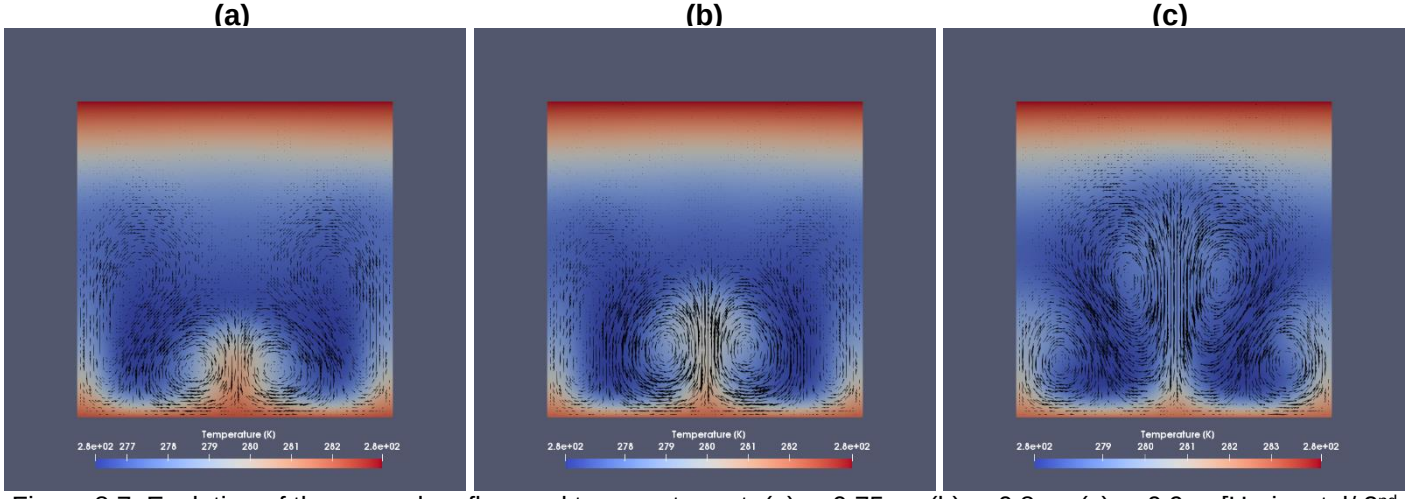

Figure 8.7: Evolution of the secondary flow and temperature at: (a) x=0.75 m, (b) x=0.8 m, (c) x=0.9 m [Horizontal/ 2nd Set of Simulations].

Figure 8.8 shows the same conclusions of the previous paragraph from a differenct perspective. At x=0.75 m and at x=1.15 m the new recirculation zones are being formed. From this position and for ~0.3 m, the magnitude of u_y is increasing and can directly affect the heat transfer inside the heat exchanger. By evaluating the temperature contours we can understand that heat is being dragged from the bottom hot surface of the channel and is being diffused in the colder core of the channel. Furthermore at x=1-1.15 m where the recirculation zone has been dissolved the magnitude of u_y is decreasing and it is negligible compared to the other two regions.

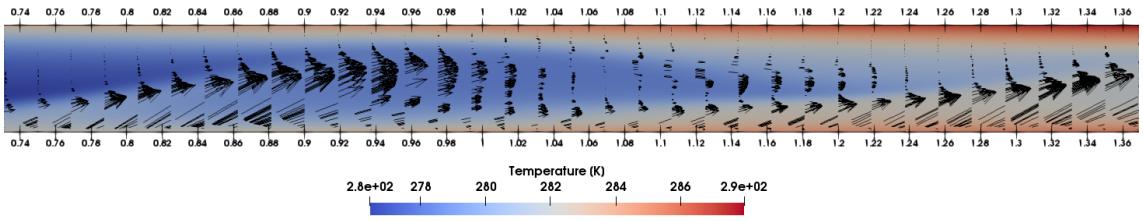

Figure 8.8: Vectors of u_y along with the temperature.

To further evaluate the heat transfer characteristics, parameters such as the convective heat transfer coefficient (h_c), wall heat flux (q_s), thermal boundary layer (δ_T) and the Nusselt number (Nu #) are being evaluated and will be discussed in this section.

For the h_c and the Nusselt number calculations the same formulas as in the Vertical section are used. Comparison of the heat transfer coefficient and the Nusselt number of the cold stream at the fully developed region of the heat exchanger for all three geometries and both set of simulations can be seen in Figure 8.9. In the three geometries of the first set of simulations specifically in the cold stream the same pattern is observed. The h_c and the wall heat flux at the top and bottom surface are maximum at the inlet of the heat exchanger because of the thin thermal boundary layer. They attain a constant value in the fully developed region where the thermal boundary layer's thickness remains constant ($\delta_T = D/2$). In all three heat exchanger geometries, the wall heat flux and consequently the h_c at the top surface are lower than the same parameters of the constant density simulations, suggesting impairment of heat transfer at this region. On the other hand, at the bottom surface the wall heat flux and h_c are larger than the constant density parameters and enhanced heat transfer is observed in this region. The average h_c (Both top and bottom surface) of the simulations where the Boussinesq approximation is implemented is larger than the constant density simulations yielding to the enhanced heat transfer observed in the heat exchanger. Results from the second set of simulations suggest that the h_c and the wall heat flux in the fully developed region for the 0.015 m and 0.03 m geometry, behave in the same way as the geometries in the first set of simulations. The Nusselt number is also calculated. For all the first case simulations (Both first set and second) where the density is constant, Nusselt number in the fully developed region attains a constant value of ~4.2. According to (Mills, 1999) in square ducts, when the heat flux is constant Nusselt number in the fully developed region should be ~3.6. The difference in these two values is expected because only the top and bottom surface of the channel are being heated (Left and right surface behave as adiabatic walls). As a result, conduction heat transfer is lower and the overall value of the Nusselt number increases. In the cases of the first set of simulations where the Boussinesq approximation is implemented, in the cold stream a decrease in the Nusselt number of the top surface and a huge increase in the Nusselt number of the bottom surface is observed. These results are in a very good agreement with the findings of (Wang, Tsuji, & Nagano, 1994). The increase of the average Nusselt number in all the cases (28% for the 0.015 m geometry, 30% for the 0.03 m geometry and 30% for the 0.06 m geometry) is a clear evidence of the increase in the convective heat transfer inside the heat exchanger. Results from the second set of simulation, for the smaller geometries, agree with the aforementioned. In the 0.015 m geometry a total increase of 1.64% is observed because of the weak buoyancy effects. In the 0.03m a huge increase of 60.5% in the Nusselt number is observed due to the strong buoyancy effects and the formation of the secondary flow. In the 0.06 m geometry both h_c and Nusselt number are affected by the formation of the new recirculation zones. Initially, in the first 0.4 m an increase in the h_c and Nusselt number is observed because the maximum streamwise velocity is shifted near the bottom surface. When the new vortices are created, they are pushing the maximum streamwise velocity towards the center of the channel. Therefore, both h_c and Nusselt number decrease. Once the vortices are dissolved the maximum streamwise velocity is shifted back at the bottom surface and once again increase of these parameters is observed. Overall, the Nusselt number increases 22% compared to the constant density case. At the same time both average h_c and Nusselt number values have increased verifying the fact that enhanced heat transfer is observed in the horizontal heat exchangers.

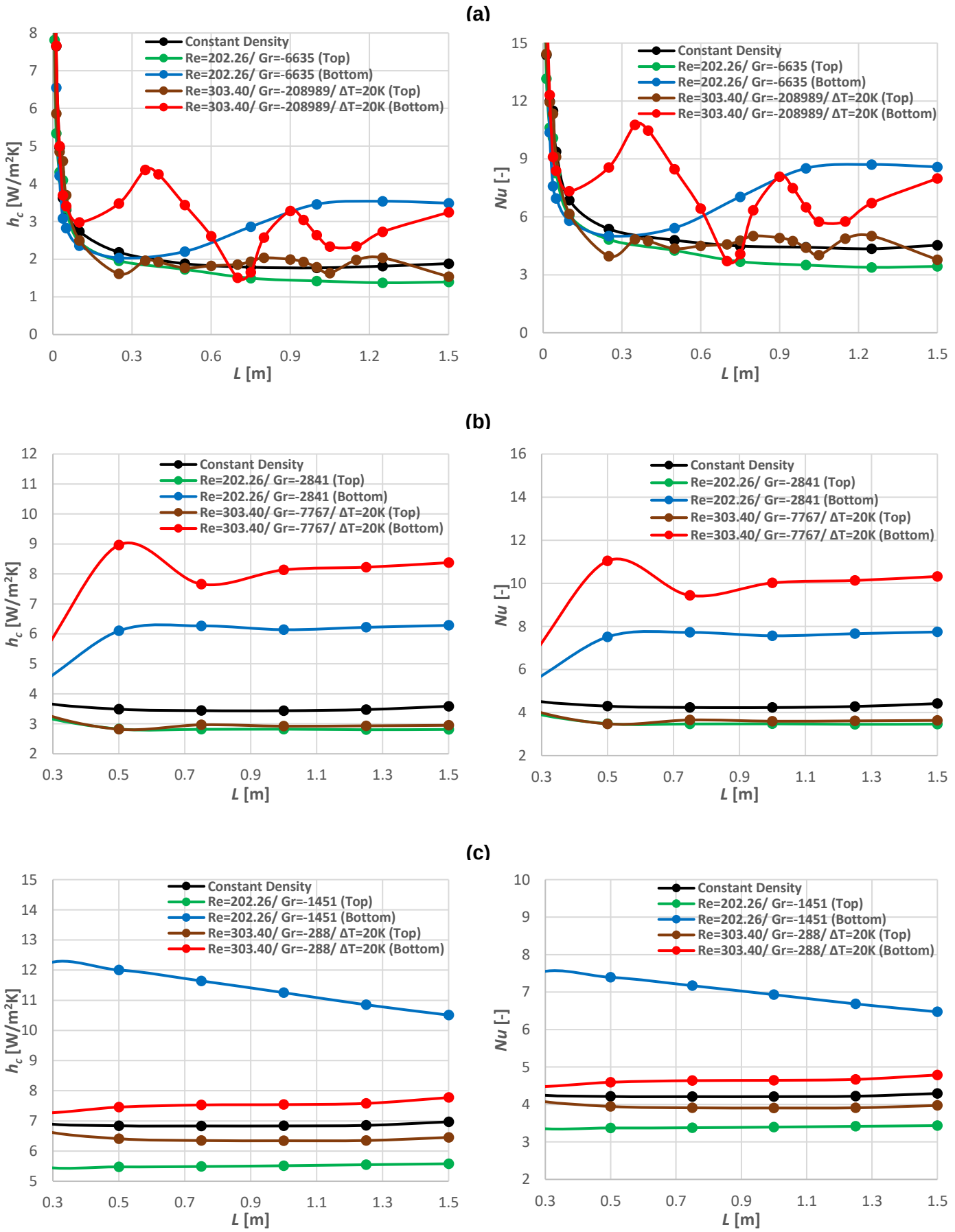

Figure 8.9: Left column: Heat Transfer Coefficient and Right column: Nusselt number for (a) 0.06 m, (b) 0.03 m and (c) 0.015 m in the fully developed region [Horizontal (Cold stream)/ 1st and 2nd Set of Simulations].

9 Performance of the Heat Exchangers

In this chapter the performance of the heat exchanger in each orientation will be assessed. Furthermore, the dependence of the Grashof number on the buoyancy effect will be investigated. Finally, some relations between the Grashof number, the overall heat transfer coefficient (*U*) and the effectiveness of the heat exchanger will be introduced.

9.1 Performance maps/ Grashof dependence [Vertical]

In the assisted buoyancy heat exchangers, in all simulations both first and second set enhanced heat transfer is observed and as a result the effectiveness of the heat exchanger increases. The effectiveness difference between the variable density cases and the constant density cases is always positive suggesting an improvement in the performance of the heat exchanger. In the vertical opposed buoyancy heat exchangers deteriorated heat transfer and decrease in the effectiveness of the heat exchanger is observed in all the simulations of the first and second set (Except for the instability case). In these simulations the effectiveness difference between the variable density cases and the constant density cases is always negative and consequently the performance of the heat exchanger is impaired. In the biggest geometry the induced instabilities produce enhanced heat transfer leading to an increase of the heat exchanger's effectiveness and improvement in its performance. The biggest increase of the effectiveness for all cases is always observed in the biggest diameters showing that buoyancy effects are directly proportional to the diameter of the heat exchanger.

In order to evaluate the dependence of Grashof number on the buoyancy effects all the vertical assisted and opposed buoyancy results (From both set of simulations) are divided in to three different categories based on the effectiveness difference of the heat exchanger. In the first group $\Delta\varepsilon$ is larger than 1.5% and buoyancy effects are causing enhancement of heat transfer. In the second group $\Delta\varepsilon$ is smaller than -1.5% and buoyancy effects produce impairment of heat transfer. In the third group $\Delta\varepsilon$ is between 1.5% and -1.5% assuming that buoyancy has negligible effect on heat transfer. A graph of *Gr* number Vs *Re* number is shown in Figure 9.1 (Assisted buoyancy results are on the left-hand side and opposed buoyancy results on the right-hand side).

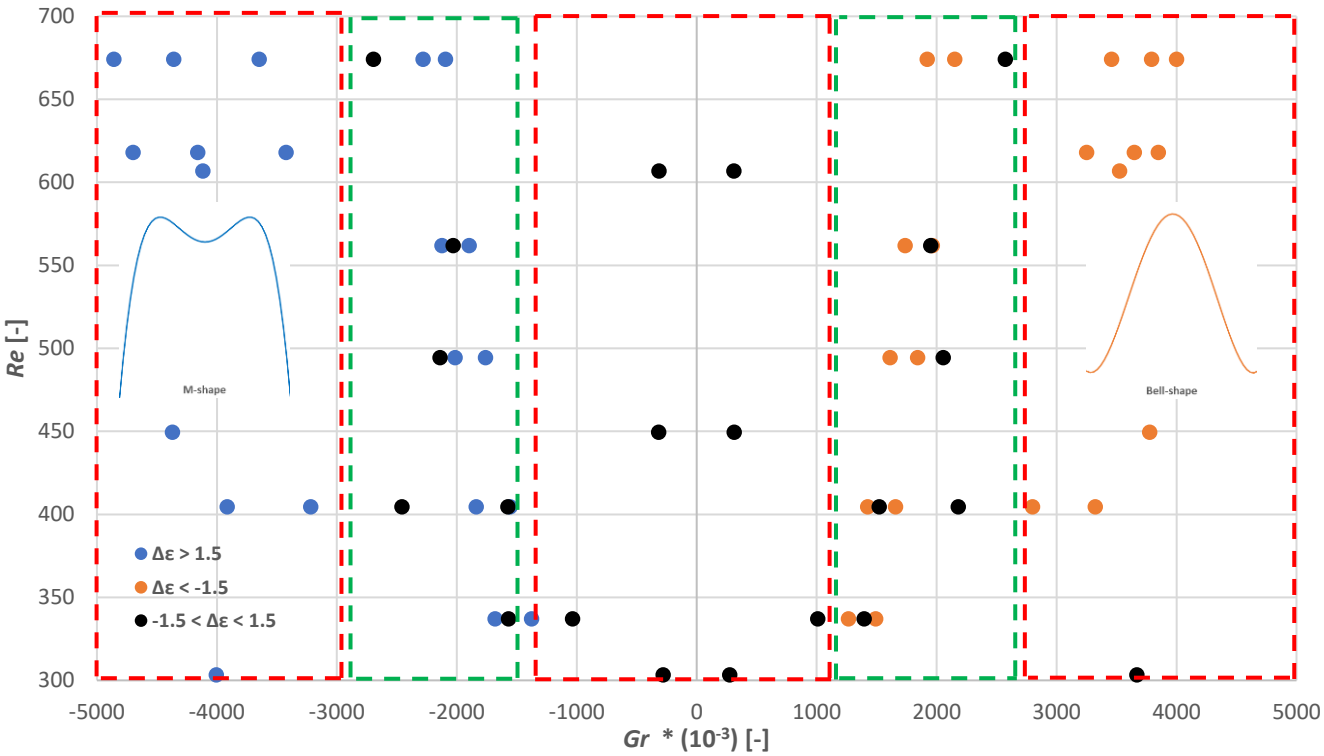

Figure 9.1: *Gr* number Vs *Re* number for all the vertical simulations.

By evaluating this figure five regions are observed. Three regions are created (red squares) where the effect of buoyancy is identified regardless of the Reynolds number. For the first region on the left-hand side, when the Grashof number is smaller than -3*10^6 enhanced heat transfer is observed (M-shape). In the second region on the right hand-side, when the Grashof number is bigger than 3*10^6 deteriorated heat transfer is observed (Bell-shape). For the third region in the middle of the graph, when the Grashof number is between -1*10^6 and (-1*10^6) the influence of buoyancy is very small. Between these three red regions two green regions are formed. In these two green regions both the Grashof and the Reynolds number are crucial in determining whether buoyancy effects will affect velocity and heat transfer inside the heat exchanger. The main conclusion of this graph is the fact that the Grashof number differentiates between buoyancy effects and is therefore also capable differentiating between enhanced or deteriorated performance.

One reason why we don't observe three clear cut regions and there are some crossovers at the limits of the regions is the huge temperature difference used in the first set of simulations to achieve Grashof number in the same order of magnitude. In order to minimize this effect and focus on the geometrical characteristics and the thermophysical properties of the flow a modified Grashof number is calculated. The formula of the modified Grashof is shown below and Figure 9.2 shows graph of Modified *Gr* number Vs *Re* number.

$$Gr_{mod} = \frac{Gr}{T_{c\,out} - T_{c\,in}} = \frac{g\beta\rho uACpd_h^4}{Lk\nu^2} = RePr\frac{g\beta Ad_h^3}{L\nu^2} \quad [36]$$

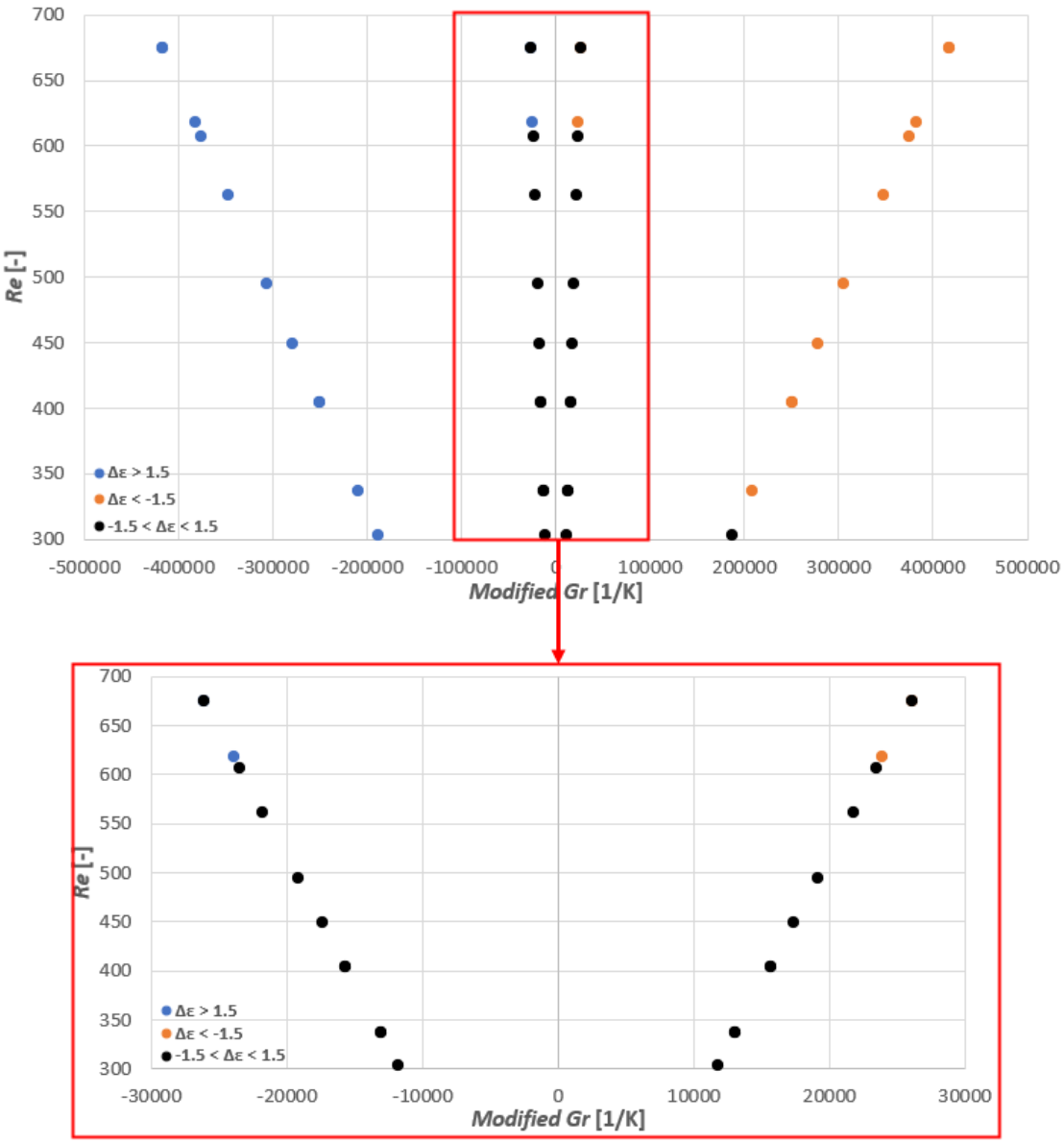

Figure 9.2: *Modified Gr* number Vs *Re* number for all the vertical simulations.

Using the modified Grashof number the three regions can be identified easier. Furthermore, the modified Grashof number can be very useful in determining the importance of the buoyancy effects. It depends on the geometrical characteristics of the heat exchanger, the thermophysical properties of the working fluid and can be calculated beforehand because it doesn't depend on the outlet temperature of the fluid.

9.2 Overall Heat Transfer Coefficient evaluation [Vertical]

The dependence of the Grashof number on the modification of the overall heat transfer coefficient of the heat exchanger is also evaluated. This investigation is conducted for identifying a function which will connect the Grashof number and the change of the overall heat transfer coefficient. Below the formula and the Figure 9.3 *Gr* number Vs ($U_{final}/U_{initial}$) for identifying this function can be seen. Where $U_{initial}$ is the overall heat transfer coefficient of the constant density's case and U_{final} is the overall heat transfer coefficient of the Boussinesq approximation's case.

$$U_{final} = U_{initial}\left(1 + f(Gr)\right) => f(Gr) + 1 = \frac{U_{final}}{U_{initial}} \quad [37]$$

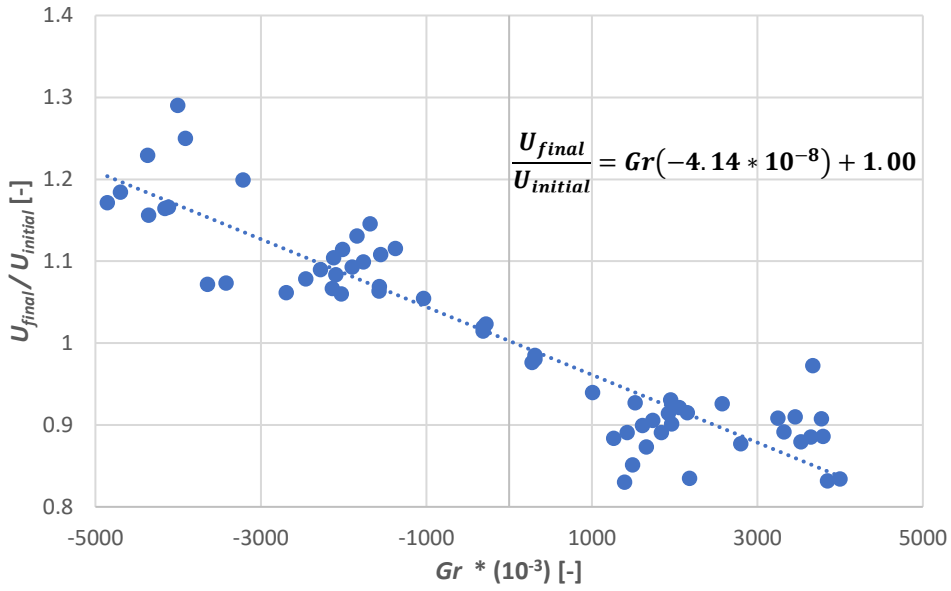

Figure 9.3: *Gr* number Vs (U_{final} / $U_{initial}$) for all the vertical simulations.

After gathering all the results from the vertical simulations, a relation between the Grashof number and the change of the overall heat transfer coefficient is estimated. This general relation can be very helpful in predicting the heat transfer in heat exchangers with buoyancy effects. For the vertical orientations this function is found to be ($-4.14*10^{-8}$).

In order to further quantify the importance of this relation the effectiveness and number of transfer units formula will be analyzed (ε-N_{tu}). For balanced heat exchangers the effectiveness formula simplifies to:

$$\varepsilon = \frac{N_{tu}}{1 + N_{tu}} \text{ where } N_{tu} = \frac{UPL}{C} \quad [38][39]$$

After further simplifying the above relation and solving for the total length of the heat exchanger:

$$L = \frac{\varepsilon C}{UP(1 - \varepsilon)} \quad [40]$$

In this final relation the total length of the heat exchanger is inversely proportional to the overall heat transfer coefficient. An increase or a decrease of the overall heat transfer coefficient due to the buoyancy effects can directly affect the length and consequently the costs of a heat exchanger.

An example is presented for understanding the impact of the buoyancy effects on the heat exchanger's length. Assuming that the effectiveness of the heat exchanger, the heated perimeter and the flow thermal capacity are constants. For a Grashof number significantly smaller than (-10^{-6}) or larger than (10^{6}), an 5% increase in the overall heat transfer coefficient of the assisted buoyancy cases and a 5% decrease in the opposed buoyancy cases is observed. This increase in the assisted buoyancy cases translates to a 4.76% reduction of the total heat exchanger's length and an 5.26% increase in the opposed buoyancy cases. For bigger change of the overall heat transfer coefficient (~15%) a 13.04% decrease of the total heat exchanger's length is observed in the assisted buoyancy cases and an 17.65% increase in the opposed buoyancy cases. These results suggest that buoyancy effects can have a significant impact in the design of the heat exchanger and can be more significant in the opposed buoyancy cases where deteriorated heat transfer is observed.

9.3 Performance maps/ Grashof dependence [Horizontal]

In the horizontal heat exchangers depending on the stream and the surface of the heat exchanger both enhanced or deteriorated heat transfer can be observed. Overall, by evaluating the total heat exchanger and not each surface individually, in all horizontal simulations enhanced heat transfer and improvement of the heat exchanger's performance and effectiveness is observed. Once again, the effectiveness difference and the buoyancy effects are directly proportional to the diameter of the heat exchanger confirming the conclusions of the previous sections. One observation which is worth noting is the fact that the effectiveness increase in the second set of simulations where the Reynolds number and the temperature difference were kept constant, for the 0.015 m geometries is less than 0.1%. These results suggest that buoyancy effects are not affecting at all the performance of the heat exchanger in this orientation for the smallest geometries.

All the horizontal results are also divided based on the same conditions as in the vertical case. The graph of *Gr* number Vs *Re* number for the horizontal cases can be seen in Figure 9.4.

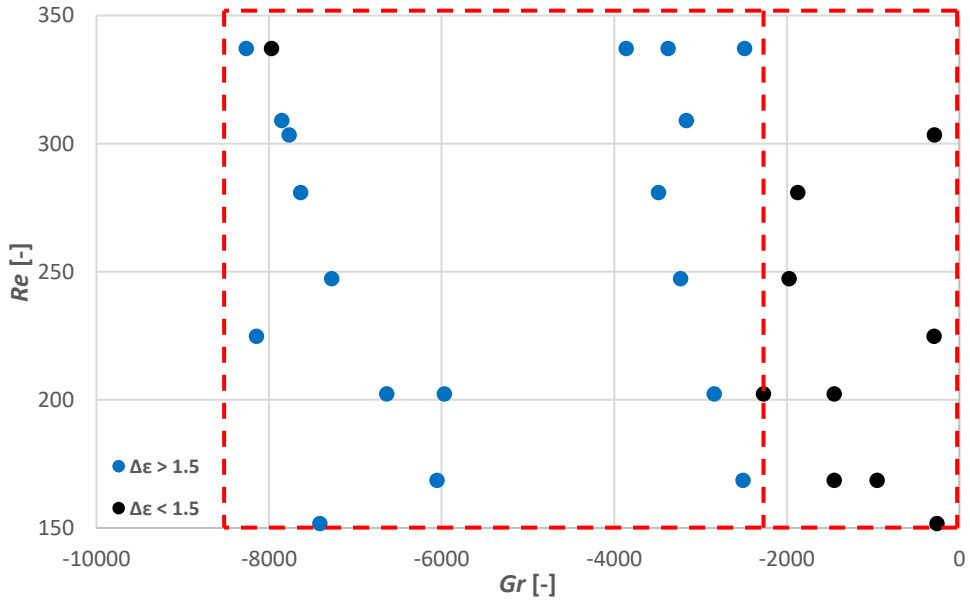

Figure 9.4: *Gr* number Vs *Re* number for all the horizontal simulation.

The Grashof number once again differentiates between the buoyancy effects and can be used to identify the enhanced performance of the heat exchanger. For the horizontal simulations two regions can be identified. The first one on the left-hand side, for Grashof number smaller than -2500 relates to enhanced heat transfer and production of secondary flow. In the second region on the right-hand side where the Grashof number is between -2500 and 0, buoyancy has very small influence on the flow transformation and heat transfer inside the heat exchanger.

9.4 Overall Heat Transfer Coefficient evaluation [Horizontal]

Similarly, as in the vertical cases the function which relates the Grashof number and the overall heat transfer coefficient of the heat exchanger is calculated. In the horizontal cases, this function is found to be -2.44*(10^{-5}). In comparison to the vertical cases buoyancy effects can only increase the overall heat transfer coefficient in horizontal geometries. As a result, both total length and cost of these heat exchangers will decrease. A graph of *Gr* number Vs $U_{final}/U_{initial}$ is shown below in Figure 9.5**.**

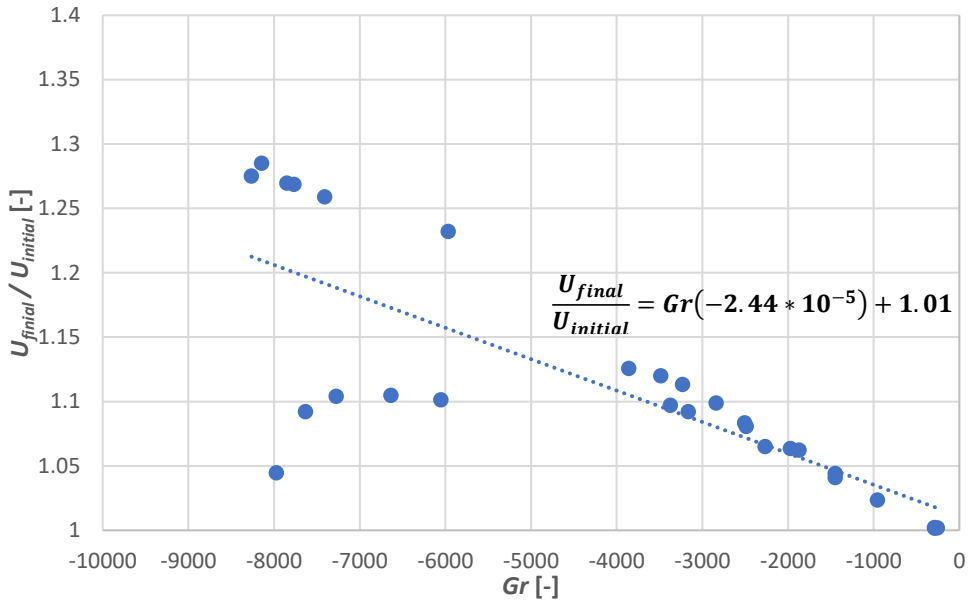

Figure 9.5: *Gr* number Vs (U_{final} / $U_{initial}$) for all the horizontal simulations.

10 Conclusions and Recommendations

In this final chapter the main outcomes of this study are summarized and recommendations for further research are provided. At the beginning of this report the main research questions were introduced:

How is the effectiveness of a Heat Exchanger affected by:

1. ***The varying density and the buoyancy effects***
2. ***Heat transfer enhancement and heat transfer deterioration***
3. ***The different geometry orientation***

To answer these questions, three objectives were formulated as described in section 1.2 which were investigated throughout this thesis. The next sections summarise the answer of each objective.

10.1 Develop a Printed Circuit Heat Exchanger model

In chapter 4 the Printed Heat Exchanger geometry is designed. Using the appropriate formulas from the literature the semi-circular channel is mapped into a square channel and the final geometry is derived. The heat exchanger's geometry is created in OpenFOAM using the correct boundary conditions and the numerical results of the heat exchanger's simulations are validated with the analytical solution from (Mills, 1999). In chapter 5 the right inlet conditions for observing buoyancy effects and flow reversal inside the heat exchanger geometry are identified.

10.2 Identify the Flow and Heat Transfer characteristics

Two sets of simulations are conducted in the three heat exchangers orientations (Assisted buoyancy, Opposed buoyancy and Horizontal). In the first set of simulations the Reynolds number and the flow thermal capacity is kept constant and the Grashof number is kept nearly constant in order to determine the dependence of Grashof number on the buoyancy effects. In the second set of simulations the Reynolds number, flow thermal capacity and temperature difference are kept constant to evaluate the performance of the heat exchanger under real working conditions.

In chapter 6 results of assisted buoyancy orientation are presented. The induced buoyancy effects inside the heat exchanger cause an acceleration of the flow adjacent to the walls and a deceleration of the flow at the centre of the channel. The maximum streamwise velocity is shifted from the middle of the channel close to the wall regions and an M-shape velocity profile is observed. In the second set of simulations and specifically in the 0.06 m geometry the intense buoyancy effects produce negative streamwise velocities in the middle of the channel and flow reversal. Due to the transformation of the velocity profile and the increase of the velocity near the walls the convection heat transfer (close to the walls) term increases. As a result, both the heat transfer coefficient and the Nusselt number increase in the assisted buoyancy orientation and enhancement of heat transfer is observed in all heat exchangers.

In chapter 7 results of opposed buoyancy orientation are presented. The induced buoyancy effects inside the heat exchanger cause an acceleration of the flow at the centre of the channel and a deceleration of the flow near the walls, leading to the formation of a Bell-shape velocity profile. The decrease of the velocity and the convection heat transfer near the walls translate into a decrease of the heat transfer coefficient and Nusselt number. Consequently, in the opposed buoyancy orientation deteriorated heat transfer is observed. In the second set of simulations, for the 0.03 and 0.06 m geometry the strong buoyancy effects produce instabilities of the flow and create recirculation zones inside the heat exchanger. These recirculation zones affect the heat flux along the length of the heat exchanger. An oscillating pattern is observed in the heat transfer coefficient and the Nusselt number. Despite expecting deteriorated heat transfer, the produced instabilities and recirculation zones result in enhancement of heat transfer in these geometries.

In chapter 8 results of horizontal orientation are presented. The induced buoyancy effects inside the heat exchanger produce a secondary flow (Two recirculation zones) which affects the streamwise velocity. Depending on the conditions, heating or cooling, the maximum streamwise velocity is shifted at the bottom surface (Heating conditions) and at the top surface (Cooling conditions). The increase of the streamwise velocity at the bottom surface produces enhanced heat transfer (Increase of the heat transfer coefficient and Nusselt number), while the decrease at the top surface produces deteriorated heat transfer (Decrease of the heat transfer coefficient and Nusselt number). The average heat transfer coefficient and Nusselt number in the horizontal heat exchangers increase, hence enhanced heat transfer is observed in this orientation. In the second set of simulations, in the 0.06 m geometry a peculiar transformation of the flow is observed. Instead of two recirculation zones, the intense buoyancy effects produce four recirculation zones inside the heat exchanger. In this geometry, under this flow characteristics increase of the heat transfer coefficient and Nusselt number is observed and therefore enhanced heat transfer.

10.3 Evaluate the Performance of the Printed Circuit Heat Exchanger

In chapter 9 the performance of the printed circuit heat exchanger in the three orientations is evaluated. In all the assisted buoyancy cases where the M-shape velocity profile and enhanced heat transfer are observed the performance and the effectiveness of the heat exchanger increase. In the opposed buoyancy cases where the Bell-shape velocity profile and deteriorated heat transfer are observed the performance and the effectiveness of the heat exchanger decrease. In the opposed buoyancy cases where the instabilities of the flow and recirculation zones are observed the effectiveness of the heat exchanger increase. Finally, in all the horizontal cases the induced buoyancy effects produce the secondary flow, recirculation zones and enhanced heat transfer. Consequently, the performance and the effectiveness of the heat exchangers in the horizontal orientation increase. One general conclusion which holds for all three orientations is the fact that the increase or the decrease in the effectiveness of the heat exchanger is directly proportional to the diameter of the heat exchanger. Thus, the diameter of the heat exchanger is one of the most crucial parameters when determining the effect of buoyancy inside the heat exchangers.

Another important parameter which is being assessed in chapter 9 is the Grashof number. In all three orientations the Grashof number differentiates between the different cases and can be used as an indicator of the importance of the buoyancy effects in the heat exchanger. For all the vertical cases, a modified Grashof number is derived. It depends on the geometrical characteristics of the heat exchanger and the thermophysical properties of the working fluid and can be used to identify the importance of buoyancy in the vertical orientation. Furthermore, it is shown that the overall heat transfer coefficient is also affected by the buoyancy effects. In both vertical and horizontal cases a function is derived which connects the change of the overall heat transfer coefficient with the Grashof number. This change has a direct impact on the design (Length) and the cost of the heat exchanger being more significant in the opposed buoyancy cases.

10.4 Recommendations

In this section, recommendations for possible improvements will be provided:

- The focus of this study is on the induced buoyancy effects, produced by the density variations inside the heat exchanger, while keeping the other thermophysical properties constant. Similar studies can be conducted to investigate the individual effect of each thermophysical property on the performance of the heat exchanger. This will help understand the real behavior of supercritical fluids where the thermophysical properties vary.
- Higher heat transfer rates are observed in turbulent flows, due to the vigorous mixing of the fluid (Mills, 1999). A similar study can be conducted in the turbulence regime in order to investigate the significance of buoyancy in higher Reynolds numbers.
- The channels of the printed circuit heat exchanger are semi-circular. A similar study can be conducted with semi-circular channels. Buoyancy effects will be observed regardless of the geometry but the effect on the flow, heat transfer and the overall performance of the heat exchanger will be different.

- Cyclic boundary conditions can be also applied at the minZ and maxZ boundaries to reproduce an actual heat exchanger geometry.
- The gradient of the wall normal velocity in the assisted buoyancy cases was found to be higher than in the constant density cases in the regions close to the wall. The same parameter was found to be lower in opposed buoyancy cases in the same regions. Investigation of this parameter might give further insights on the mechanism of the enhanced and deteriorated heat transfer.
- More simulations can be conducted in the ‘’green boxes’’ of Figure 9.1 in order to better divide the three regions (Enhanced buoyancy, negligible buoyancy, opposed buoyancy).

Bibliography

Ahn, Y., Bae, S., Kim, M., Cho, S., Baik, S., Lee, J., & Cha, J. (2015). Review of supercritical CO2 power cycle technology and current status of research and development. *Nuclear Engineering and Technology, 47*(6), 647-661.

Banuti, D. (2015). Crossing the Widom-line - Supercritical pseudo-boiling. *Journal of Supercritical Fluids, 98*, 12-16.

Bermejo, M., & Cocero, M. (2006). Supercritical water oxidation: A technical review. *AIChE Journal, 52*(11), 3933-3951.

Cao, X., Rao , Z., & Liao , S. (2011). Laminar convective heat transfer of supercritical CO2 in horizontal miniature circular and triangular tubes. *Applied Thermal Engineering, 31*(14-15), 2374-2384.

Causes of Climate Chnage. (n.d.). Retrieved from Europpean Comission: https://ec.europa.eu/clima/climate-change/causes-climate-change_en

Chen, M., Kim, I., Sun, X., Christensen, R., Bartel, N., Utgikar, V., & Sabharwall, P. (2013). Design of Printed Circuit Heat Exchangers for Very High Temperature Reactors. *Transactions of the American Nuclear Society*, 1090-1094.

Cheng, H., Zhao, J., & Rowinski, M. (2017). Study on two wall temperature peaks of supercritical fluid mixed convective heat transfer in circular tubes. *International Journal of Heat and Mass Transfer, 113*, 257-267.

CoolProp. (n.d.). Retrieved from http://www.coolprop.org/#what-is-coolprop.

Desrayaud, G., & Lauriat, G. (2009). Flow reversal of laminar mixed convection in the entry region of symmetrically heated, vertical plate channels. *International Journal of Thermal Sciences, 48*, 2036-2045.

Eckert, C., Knutson, B., & Debenedetti, P. (1996). Supercritical fluids as solvents for chemical and materials processing. *Nature, 383*, 313-318.

Energy Matters. (2018, October 25). Retrieved from http://euanmearns.com/every-big-bit-helps/

Guo, J., & Huai, X. (2017). Performance analysis of Printed Circuit Heat Exchanger for supercritical Carbon Dioxide. *Journal of Heat Transfer, 139*(6).

Gupta, S., Farah, A., King, K., Mokry, S., & Pioro, I. (2010). Developing New Heat-Transfer Correlation for SuperCritical-Water Flow in Vertical Bare Tubes. *Conference: 18th International Conference on Nuclear Engineering*.

Gupta, S., Saltanov, E., Mokry, S. J., Pioro, I., Trevani, L., & McGillivray, D. (2013). Developing empirical heat-transfer correlations for supercritical CO2 flowing in vertical bare tubes. *Nuclear Engineering and Design, 261*, 116-131.

Harnatty, T., Rosen, E., & Kabel, R. (1958). Effect of Heat Transfer on Flow Field at Low Reynolds Numbers in Vertical Tubes. *Industrial & Engineering Chemistry, 50*(5), 815-820.

He, S., Kim, W., & Jackson, J. (2008). A computational study of convective heat transfer to carbon dioxide at a pressure just above the critical value. *Applied Thermal Engineering, 28*(13), 1662-1675.

Jackson, J. (2013). Fluid flow and convective heat transfer to fluids at supercritical pressure. *Nuclear Engineering and Design, 264*, 24-40.

Jiang, P., Liu, B., Zhao, C., & Luo, F. (2013). Convection heat transfer of supercritical pressure carbon dioxide in a vertical micro tube from transition to turbulent flow regime. *International Journal of Heat and Mass Transfer, 56*(1-2), 741-749.

Khalesi, J., & Sarunac, N. (2019). Numerical analysis of flow and conjugate heat transfer for supercritical CO2 and liquid sodium in square. *International Journal of Heat and Mass Transfer, 132*, 1187-1199.

Kim, D., & Kim, M. (2011). Experimental investigation of heat transfer in vertical upward and downward supercritical CO2 flow in a circular tube. *International Journal of Heat and Fluid Flow, 32*(1), 176-191.

Kruizenga, A., Anderson, M., Fatima, R., Corradini, M., Towne, A., & Ranjan, D. (2011). Heat transfer of supercritical carbon dioxide in Printed Circuit Heat Exchanger geometries. *Journal of Thermal Science and Engineering Applications, 3*(3).

Kundu, P. K., Cohen, I. M., & Dowling, D. R. (2016). *Fluid Mechanics* (6th ed.).

Kuppan, T. (2000). *Heat Exchanger Design Handbook.* New York: Marcel Dekk.

Kurganov, V., Zeigarnik, Y., & Maslakova, I. (2012). Heat transfer and hydraulic resistance of supercritical pressure coolants. Part I: Specifics of thermophysical properties of supercritical pressure fluids and

turbulent heat transfer under heating conditions in round tubes (state of the art). *International Journal of Heat and Mass Transfer, 55*(11-12), 3061-3075.

Kurganov, V., Zeigarnik, Y., & Maslakova, I. (2013). Heat transfer and hydraulic resistance of supercritical-pressure coolants.Part II: Experimental data on hydraulic resistance and averaged turbulent flow structure of supercritical pressure fluids during heating in round tubes under normal & DHT conditions. *International Journal of Heat and Mass Transfer, 58*(1-2), 152-167.

Laaroussi, N., Lauriat, G., & Desrayaud, G. (2009). Effects of variable density for film evaporation on laminar mixed convection in a vertical channel. *International Journal of Heat and Mass Transfer, 52*, 151-164.

Lecompte, S., Ntavou, E., Tchanche, B., Kosmadakis, G., Pillai, A., Manolakos, D., & de Paepe, M. (2019). Review of experimental research on supercritical and transcritical thermodynamic cycles designed for heat recovery application. *Applied Sciences (Switzerland), 9*(12).

Li, M., Zhu, H., Guo , J., Wang, K., & Tao, W. (2017). The development technology and applications of supercritical CO2 power cycle in nuclear energy, solar energy and other energy industries. *Applied Thermal Engineering, 126*, 255-275.

Luo, L., Flamant, G., Qi, L., Xigang, Y., & Pierre, N. (2011). Compact heat exchangers: A review and future applications for a new generationof high temperature solar receivers. *Renewable and Sustainable Energy Reviews, 15*, 4855-4875.

Meshram, A., Jaiswal, A., Khivsara, S., Ortega, J., Ho, C., Bapat, R., & Dutta, P. (2016). Modeling and analysis of a Printed Circuit Heat Exchanger for supercritical CO2 power cycle applications. *Applied Thermal Engineering, 109*, 861-870.

Mills, A. (1999). *Basic Heat & Mass Transfer* (2nd ed.).

Nguyen, C., Maiga, S., Landry, M., Galanis, N., & Roy, G. (2004). Numerical investigation of flow reversal and instability in mixed laminar vertical tube flow. *International Journal of Thermal Sciences, 43*(8), 797-808.

Nikitin, K., Kato, Y., & Ngo, L. (2006). Printed circuit heat exchanger thermal-hydraulic performance in supercritical CO2 experimental loop. *International Journal of Refrigeration, 29*(5), 807-814.

Niu, X., Yamaguchi, H., Zhang, X., Iwamoto, Y., & Hashitani, N. (2011). Experimental study of heat transfer characteristics of supercritical CO2 fluid in collectors of solar Rankine cycle system. *Applied Thermal Engineering, 31*(6-7), 1279-1285.

OpenFOAMWiki. (2019, April 23). Retrieved from https://openfoamwiki.net/index.php/ChtMultiRegionFoam.

Pioro, I. (2020). *Supercritical-Fluids Thermophysical Properties and Heat Transfer in Power-Engineering Applications.* London,UK: IntechOpen.

Pioro, I., & Mokry, S. (2011). Thermophysical Properties at Critical and Supercritical Conditions. *Heat Transfer - Theoretical Analysis, Experimental Investigations and Industrial Systems*.

Pitla, S., Robinson, D., Groll, E., & Ramadhyani, S. (1998). Heat transfer from supercritical carbon dioxide in tube flow: A critical review. *HVAC and R Research, 4*(3), 281-310.

Pizzarelli, M. (2018). The status of the research on the heat transfer deterioration in supercritical fluids: A review. *International Communications in Heat and Mass Transfer, 95*, 132-138.

Ravindran, P., Sabharwall, P., & Anderson, N. A. (2010). Modeling a Printed Circuit Heat Exchanger with RELAP5-3D for the Next Generation Nuclear Plant. *Office of Scientific and Technical Information Technical Reports*.

Sabirzyanov, A., Il'in, A., Akhunov, A., & Gumerov, F. (2000). Solubility of Water in Supercritical Carbon Dioxide. *Kazan State University of Technology*.

Sarkar, J. (2015). Review and future trands of supercritical CO2 Rankine cycle for low-grade heat conversion. *Renewable and Sustainable Energy Reviews, 48*, 434-451.

Schltinder, E. (1983). *Heat Exchanger Design Handbook.* Hemisphere Publishing Corporation.

Schulenberg, T., Starflinger, J., Marsault, P., Bittermann, D., Maraczy, C., Laurien, E., . . . Toivonen, A. (2011). European supercritical water cooled reactor. *Nuclear Engineering and Design*, 3505-3513.

U.S. Energy Information Administration (EIA). (2019, September 24). Retrieved from Eia.gov: https://www.eia.gov/todayinenergy/detail.php?id=41433

U.S. Global Change Research Programm. (n.d.). Retrieved from GlobalChange.gov: https://www.globalchange.gov/browse/indicators/atmospheric-carbon-dioxide

Wang, J., Guan, Z., Gurgenci, H., Hooman, K., Veeraragavan, A., & Kang, X. (2018). Computational investigations of heat transfer to supercritical CO2 in large horizontal tube. *Energy Conversion and Management, 157*, 536-548.

Wang, J., Guan, Z., Gurgenci, H., Veeraragavan, A., Kang, X., Sun, Y., & Hooman, K. (2018). Numerical study on cooling heat transfer of turbulent supercritical CO2 in large horizontal tubes. *International Journal of Heat and Mass Transfer, 126*, 1002-1019.

Wang, M., Tsuji, T., & Nagano, Y. (1994). Mixed convection with flow reversal in the thermal entrance region of horizontal and vertical pipes. *International Journal of Heat and Mass Transfer, 37*(15), 2305-2319.

Yang, C., Xu, J., Wang, X., & Zhang, W. (2013). Mixed convective flow and heat transfer of supercritical CO2 in circular tubes at various inclination angles. *International Journal of Heat and Mass Transfer, 64*, 212-223.

Yoo, J. (2013). The turbulent flows of supercritical fluids with heat transfer. *Annual Review of Fluid Mechanics, 45*, 495-525.

Yoon, H., Ahn, Y., Lee, J., & Addad, Y. (2012). Potential advantages of coupling supercritical CO2 Brayton cycle to water cooled small and medium size reactor. *Nuclear Engineering and Design, 245*, 223-232.

Yoon, S.-J., Sabharwall, P., & Kim, E.-S. (n.d.). Analytical Study on Thermal and Mechanical Design of Printed Circuit Heat Exchanger. *Idaho National Laboratory*.

Yu, S., Li, H., Lei, X., Feng, Y., Feng, Y., Zhang, Y., . . . Wang, T. (2013). Influence of buoyancy on heat transfer to water flowing in horizontal tubes under supercritical pressure. *Applied Thermal Engineering, 59*(1-2), 380-388.

Zhang, S., Xu, X., Liu, C., & Dang, C. (2020). A review on application and heat transfer enhancement of supercritical CO2 in low-grade heat conversion. *Applied Energy, 269*.